SOVIET ATOMIC ENERGY

АТОМНАЯ ЭНЕРГИЯ
(ATOMNAYA ÉNERGIYA)

TRANSLATED FROM RUSSIAN

SOVIET ATOMIC ENERGY

Soviet Atomic Energy is a translation of Atomnaya Energiya, a publication of the Academy of Sciences of the USSR.

An agreement with the Copyright Agency of the USSR (VAAP) makes available both advance copies of the Russian journal and original glossy photographs and artwork. This serves to decrease the necessary time lag between publication of the original and publication of the translation and helps to improve the quality of the latter. The translation began with the first issue of the Russian journal.

Soviet Atomic Energy is abstracted or indexed in Chemical Abstracts, Chemical Titles, Pollution Abstracts, Science Research Abstracts, Parts A and B, Safety Science Abstracts Journal, Current Contents, Energy Research Abstracts, and Engineering Index.

Consultants Bureau journals appear about six months after the publication of the original Russian issue. For bibliographic accuracy, the English issue published by Consultants Bureau carries the same number and date as the original Russian from which it was translated. For example, a Russian issue published in December will appear in a Consultants Bureau English translation about the following June, but the translation issue will carry the December date. When ordering any volume or particular issue of a Consultants Bureau journal, please specify the date and, where applicable, the volume and issue numbers of the original Russian. The material you will receive will be a translation of that Russian volume or issue.

CONSULTANTS BUREAU, NEW YORK AND LONDON

233 Spring Street
New York, New York 10013

Published monthly. Second-class postage paid at Jamaica, New York 11431.

Mailed in the USA by Publications Expediting, Inc., 200 Meacham Avenue, Elmont, NY 11003.

POSTMASTER: Send address changes to Soviet Atomic Energy, Plenum Publishing Corporation, 233 Spring Street, New York, NY 10013.

SOVIET ATOMIC ENERGY

CONTENTS

Engl./Russ.

CONTENTS

(continued)

Engl./Russ.

ARTICLES

EFFECTIVE SINGLE-GROUP COEFFICIENT OF NEUTRON
DIFFUSION IN REACTOR GRIDS

N. I. Laletin and V. F. Boyarinov   UDC 621.039.5

INTRODUCTION

In the surface-harmonic method (SHM) — a generalization of homogenization theory; see [1, 2], for example — the effective coefficient of neutron diffusion in the reactor grids is introduced, among other quantities. The corresponding definition is a natural generalization (also suitable for nonuniform grids) of the definition of the effective diffusion coefficient adopted in [3, 4], where sufficiently extended uniform grids were considered.

In the single-group approach, the effective diffusion coefficient is defined as follows

$$D = \frac{a}{2\Psi_{as}\left(\frac{a}{2}\right)}, \tag{1}$$

where

$$\Psi_{as}\left(\frac{a}{2}\right) = \frac{3}{l} \int_{4\pi} d\Omega \Omega_x^2 \int_{\Gamma_1} dr_s \Psi(r_s, \Omega) \tag{2}$$

is the value of the combination of zero and second angular moments — $(\Omega_x = \frac{1}{3}[1 + 2P_2(\Omega_x)])$ — of the antisymmetric trial function at the cell boundary Γ_1; l is the length of boundary Γ_1; a is the lattice step. In Eqs. (1) and (2), the coordinate x is measured from the center of the cell, and in the problem of determining the antisymmetric trial function the x axis is in the opposite direction to the current flux.

It is assumed that the secondary angular moments in Eq. (2) almost always make a small contribution, and Eq. (1) may be approximated as follows:

$$D \cong \frac{a}{2\Psi^0{}_{as}\left(\frac{a}{2}\right)}, \tag{3}$$

where $\Psi^0_{as}\left(\frac{a}{2}\right) = \frac{1}{l} \int_{4\pi} d\Omega \int_{\Gamma_1} dr_s \Psi(r_s \Omega)$ is the neutron flux at the cell boundary. This approximation was used in the El'shin program, in which the diffusion coefficient is calculated for square and hexahedral cells in the P_2 and P_4 approximations of the spherical-harmonic method. For a cylindrical cell, the expression analogous to Eq. (3) takes the form

$$D \cong \frac{R}{\Psi^0_{as}(R)}, \tag{4}$$

where R is the radius of the cylindrical cell.

This approximation was used in the first version of the ORAR-Ts program [5]. In calculations by this program, the following features were noted: a strong dependence of the diffusion coefficient in Eq. (4) on the angular distribution of the neutrons entering the cell — tens and even hundreds of percent (ORAR-Ts) and large deviation of its value beyond the limits of the interval $[1/3\bar{\Sigma}, \bar{\lambda}/3]$.*

---

*It is known — see [6], for example — that for a cell with weak absorption $(1/3)\bar{\Sigma}$ and $\bar{\lambda}/3$ are the limiting values of the diffusion coefficient. It is natural to expect that, for cells with weak absorption, the diffusion coefficient will not pass far beyond the limits of this interval.

These results lend themselves to more careful analysis and it is also of interest to verify the approximations on which Eqs. (3) and (4) are based.

Diffusion Coefficient in a One-Dimensional Plane Cell

In one-dimensional plane geometry, the neutron-transfer equation in the transport approximation takes the following form in the single-group case

$$\mu \frac{\partial}{\partial x} \Psi(x, \mu) + \Sigma_{tr}(x) \Psi(x, \mu) = \frac{1}{2} \Sigma_{s, tr} \Phi_0(x) + \frac{\nu \Sigma_f}{k_{ef}} \Phi_0(x) \tag{5}$$

(the notation is conventional).

The solution of Eq. (5) according to SHM is

$$\Psi(x, \mu) = \Psi_{sym}(x, \mu) \delta J + \Psi_{as}(x, \mu) J, \tag{6}$$

where Ψ_{sym} and Ψ_{as} are the symmetric and antisymmetric trial functions [1], i.e., $\Psi_{sym}(x, \mu) = \Psi_{sym}(-x, -\mu)$, $\Psi_{as}(x, \mu) = \Psi_{as}(-x, -\mu)$; $\delta J = \frac{1}{2}(j_1 - j_2)$ is the neutron current reaching the cell (or leaving it); $J = \frac{1}{2} \cdot (j_1 + j_2)$ is the neutron current passing through the cell; j_1 and j_2 are the neutron currents at the cell boundaries.

This representation is a generalization of that adopted in [3, 4] and is related as follows to the division of the solution $\Psi^B(x, \mu B) e^{iBx}$ into components in [4] for a uniform and sufficiently extended ($Ba \ll 1$) grid:

$$\Psi^B(x, \mu, B) e^{iBx} \cong \left[\Psi^B(x, \mu, 0) + \right.$$
$$+ \frac{\partial}{\partial x} \Psi^B(x, \mu, B)|_{B=0} iB \left. \right] (1 + iBx) \cong \Psi^B(x, \mu, 0) +$$
$$+ iB \left[x \Psi^B(x, \mu, 0) + \frac{\partial}{\partial x} \Psi^B(x, \mu, B)|_{B=0} \right]; \tag{7}$$

$$\begin{cases} \Psi_{sym}(x, \mu) = const_1 \Psi^B(x, \mu, 0); \\ \Psi_{as}(x, \mu) = const_2 \left[x \Psi^B(x, \mu, 0) + \right. \\ \left. + \frac{\partial}{\partial x} \Psi^B(x, \mu, B)|_{B=0} \right]. \end{cases} \tag{8}$$

Consider the equation of the spherical-harmonic method

$$(n+1) \frac{d\Phi_{n+1}(x)}{dx} + n \frac{d\Phi_{n-1}(x)}{dx} + (2n+1) \Sigma_{tr}(x) \Phi_n(x) = 0, \tag{9}$$

where $\Phi_n(x) = \int_{4\pi} d\Omega P_n(\mu) \Psi(x, \mu)$; $P_n(\mu)$ are Legendre polynomials. When $n = 1$, it follows from Eq. (9) that

$$\Phi_1(x) = J(x) = -D(x) \frac{d}{dx} [\Phi_0(x) + 2\Phi_2(x)].$$

If $d\Phi_2(x)/dx$ may be neglected, the usual Fin law is obtained:

$$J(x) = -D(x) \frac{d\Phi_0(x)}{dx}. \tag{11}$$

In Eqs. (10) and (11), $D = 1/(3\Sigma_{tr})$, but in Eq. (10) D is the proportionality factor between the current and the derivative of the combination of the flux with the second moment. This combination is called the neutron level. The introduction of this term is justified in that the neutron current is proportional to the gradient of this quantity, i.e., the neutrons flow from a region with a high neutron level to one with a low level (see Appendix). Note that Eq. (10) is absolutely accurate if the precise functions $\Phi_0(x)$ and $\Phi_2(x)$ are available. The finite-difference analog of Eq. (10) may be written in the form

$$D = \frac{J \Delta x}{\Delta [\Phi_0 + 2\Phi_2]}, \tag{12}$$

where Δx is the plate thickness; $\Delta[\Phi_0 + 2\Phi_2]$ is the jump in neutron level; J is the neutron current passing through the plate; $J = \frac{1}{2}[J(x_1) + J(x_2)]$. Substituting Eq. (8) into Eq. (12) gives

632

$$D = \frac{\Delta x}{\Delta \left| \Psi_{as}^{0} + 2 \Psi_{as}^{2} \right|} , \tag{13}$$

where

$$\Psi_{as}^{n} = \int_{-1}^{1} \Psi_{as}(\mu) P_n(\mu) \, d\mu.$$

Suppose that $a/2$ is half the plate thickness, and the neutron current through the cell is directed along the x axis; then

$$D = \frac{a}{2 \left[\Psi_{as}^{0} \left(-\frac{a}{2} \right) + 2 \Psi_{as}^{2} \left(-\frac{a}{2} \right) \right]}. \tag{14}$$

Equation (14) completely coincides with Eq. (1), which is the definition of the diffusion coefficient in the SHM equations. Another expression may be obtained for the diffusion coefficient: if Eq. (7) is multiplied by $\Omega_x = (\Omega i_x) = \mu$ and integrated over Ω and over the volume of the cell, some elementary transformations lead to the result

$$\frac{a}{2 \left[\Psi_{as}^{0} \left(-\frac{a}{2} \right) + 2 \Psi_{as}^{2} \left(-\frac{a}{2} \right) \right]} = \frac{1}{3 \overline{\Sigma}_{tr} k_j} , \tag{15}$$

where

$$\overline{\Sigma}_{tr} = \frac{\dfrac{1}{a} \displaystyle\int_{-a/2}^{a/2} dx \Sigma_{tr}(x) \Psi_{as}^{1}(x)}{\dfrac{1}{a} \displaystyle\int_{-a/2}^{a/2} dx \, \Psi_{as}^{1}(x)} ;$$

$$k_j = \frac{\overline{\Psi}_{as}^{1}}{\Psi_{as}^{1} \left(-\frac{a}{2} \right)} ; \quad \Psi_{as}^{1} \left(-\frac{a}{2} \right) = 1. \tag{16}$$

It follows from a comparison of Eqs. (14) and (15) that

$$D = 1/(3 \overline{\Sigma}_{tr} k_j). \tag{17}$$

Thus, two alternative expressions — Eqs. (14) and (17) — are obtained for the diffusion coefficient in a one-dimensional plane cell, allowing the computational scheme to be constructed in different ways. Consider Eq. (17). Note that $\overline{\Sigma}_{tr}$ is the mean (with current weighting) transport cross section of the plane cell; k_j is the current nonuniformity coefficient in the plane cell. Suppose that in the plane cell i is the number of the zone with maximum transport cross section and j is the number of the zone with minimum transport cross section; then

$$\frac{1}{3 \Sigma_{tr}^{i}} \leqslant \frac{1}{3 \overline{\Sigma}_{tr}} \leqslant \frac{1}{3 \Sigma_{tr}^{j}} .$$

In view of its definition — see Eq. (16) — the coefficient k_j is usually not greatly different from unity, and in a nonbreeder cell is always less than unity. Thus, Eq. (17) is expedient in that it has a clear physical meaning and allows the limits of variation of the diffusion coefficient in the cell to be approximately estimated.

Diffusion Coefficient in Square Cell

In two-dimensional Cartesian geometry, the neutron-transfer equation in the transport approximation takes the form*

$$\mu \frac{\partial \Psi(w)}{\partial x} + \sqrt{1 - \mu^2} \cos \chi \, \frac{\partial \Psi(w)}{\partial y} + \Sigma_{tr}(x, y) \Psi(w) = \frac{\Sigma_{s, tr}(x, y)}{4\pi} \Psi^{00}(x, y), \tag{18}$$

_____

*Since, as is evident from the formulas of the preceding section, the diffusion coefficient depends only on the antisymmetric component of the solution, which is influenced fairly weakly by the breeding, as a rule, a cell without breeding is considered here and below, for the sake of simplicity.

633

where $w = \{x, y, \Omega\}$; $\mu = \Omega i_X$; χ is the angle between the planes (X, Y) and (Ω, i_X). The solution of Eq. (18) in a square centrally symmetric cell may be written, in accordance with SHM [1], in the form of a linear combination of trial functions

$$\Psi(w) = \Psi_{sym}(w)\,\delta J + \Psi_{as}^x(w)\,J_x + \Psi_{as}^y(w)\,J_y. \tag{19}$$

Here J_X and J_y are the neutron currents passing through the cell in the direction of the x and y axes, respectively.

Expansion of $\Psi(w)$ with respect to spherical functions is used, in the form

$$\Psi(w) = \sum_{n,h} \frac{2n+1}{2\pi(1+\delta_{h0})} Y_n^h(\Omega)\Psi^{nh}(x, y), \tag{20}$$

where

$$Y_n^h(\Omega) = \sqrt{\frac{(n-k)!}{(n+k)!}}\, P_n^h(\mu)\cos k\chi. \tag{21}$$

Multiplying the Eq. (18) by $\Omega_X = \mu$, integrating the results over Ω and the cell volume, and making a series of transformations, taking account of Eqs. (19) and (20), it is found that

$$\frac{a}{2\left[\Psi_{as}^{00}\left(-\frac{a}{2}\right) + 2\Psi_{as}^{10}\left(-\frac{a}{2}\right)\right]} = \frac{1}{3\overline{\Sigma}_{tr}k_j}, \tag{22}$$

where

$$\overline{\Sigma}_{tr} = \frac{\dfrac{1}{a^2}\displaystyle\int_{-a/2}^{a/2} dx \int_{-a/2}^{a/2} dy\,\Sigma_{tr}(x, y)\,\Psi_{as}^{10}(x, y)}{\dfrac{1}{a^2}\displaystyle\int_{-a/2}^{a/2} dx \int_{-a/2}^{a/2} dy\,\Psi_{as}^{10}(x, y)}; \tag{23}$$

$$k_j = \frac{\overline{\Psi}_{as}^{10}}{\Psi_{as}^{10}\left(-\frac{a}{2}\right)}; \quad \Psi_{as}^{10}\left(-\frac{a}{2}\right) = 1;$$

$$\Psi_{as}^{nh}\left(-\frac{a}{2}\right) = \frac{1}{a}\int_{-a/2}^{a/2} dy\,\Psi_{as}^{nh}\left(-\frac{a}{2}, y\right).$$

Here a is the side of the square cell.

Thus, for the diffusion coefficient in a square cell

$$D = \frac{a}{2\left[\Psi_{as}^{00}\left(-\frac{a}{2}\right) + 2\Psi_{as}^{20}\left(-\frac{a}{2}\right)\right]} \tag{24}$$

and

$$\tag{25}$$

$$D = \frac{1}{3\overline{\Sigma}_{tr}k_j}.$$

Diffusion Coefficient in a Hexahedral Cell

As in the preceding section, a two-dimensional Cartesian coordinate system is used, with its origin at the center of the cell; the x axis is directed through the middle of one of the sides. Let Γ_L denote the cell boundary to the left of the y axis and Γ_R the boundary to the right. The representation of $\Psi(w)$ in terms of trial functions and spherical harmonics will be as in Eqs. (19) and (20), respectively. Multiplying Eq. (18) by $\Omega_X = \mu$, integrating the result over Ω and the cell volume, and making a series of transformations, taking account of Eqs. (19) and (20), it is found that

$$\frac{a}{2\left[\overline{\Psi}_{as,\,\Gamma_L}^{x00} + 2\overline{\Psi}_{as,\,\Gamma_L}^{x20}\right]} = \frac{1}{3\overline{\Sigma}_{tr}k_j}, \tag{26}$$

where

634

$$\overline{\Sigma}_{tr} = \frac{\frac{1}{V} \int\limits_V dr \Sigma_{tr}(x,\,y) \Psi_{as}^{x10}(x,\,y)}{\frac{1}{V} \int\limits_V dr \Psi_{as}^{x10}(x,\,y)} \; ;$$

$$k_j = \frac{\overline{\Psi}_{as}^{x10}}{\overline{\Psi}_{as,\,r_L}^{x10}} \; ; \quad \overline{\Psi}_{as,\,r_L}^{x10} = 1; \tag{27}$$

$$\overline{\Psi}_{as,\,r_L}^{xnh} = \frac{1}{l_{r_L}} \int\limits_{r_L} dr_s \Psi_{as}^{xnh}(x,\,y).$$

Thus, for the diffusion coefficient in a hexhedral cell

$$D = \frac{a}{2\,[\overline{\Psi}_{as,\,r_L}^{x00} + 2\overline{\Psi}_{as,\,r_L}^{x20}]}; \tag{28}$$

$$D = \frac{1}{3\overline{\Sigma}_{tr}k_j}. \tag{29}$$

Diffusion Coefficient in Cylindrical Cell

The neutron-transfer equation in the transport approximation may be written in the following form in a cylindrical coordinate system

$$\mu \frac{\partial \Psi(w)}{\partial \rho} + \frac{(1-\mu^2)\cos^2 \chi}{\rho} \frac{\partial \Psi(w)}{\partial \mu} + \frac{\mu \sin 2\chi}{2\rho} \frac{\partial \Psi(w)}{\partial \chi} +$$
$$+ \frac{\sqrt{1-\mu^2}\cos \chi}{\rho} \frac{\partial \Psi(w)}{\partial \alpha} + \Sigma_{tr}(\rho)\,\Psi(w) = \frac{\Sigma_{s,\,tr}(\rho)}{4\pi}\,\Psi^{00}(\rho,\,\alpha), \tag{30}$$

where $w = \{\rho,\,\alpha,\,\Omega\}$; $\mu = (\Omega\rho)/\rho$; χ is the angle between the planes (Ω,ρ) and $(x,\,y)$.

The solution in the cylindrical cell is written in the form of a set of trail functions

$$\Psi(w) = \Psi_{sym}(w)\,\delta J + \Psi_{as}(w)\,J, \tag{31}$$

where δJ is the neutron current reaching the cell; J is the neutron current passing through the cell in the direction of the x axis.

Suppose that the coordinate origin is at the center of a cell of radius R. The solution is expanded in terms of spherical functions

$$\Psi(w) = \sum_{n,h} \frac{2n+1}{2\pi(1+\delta_{h0})}\,Y_n^h(\Omega)\,f_h(\alpha)\,\Psi^{nh}(\rho), \tag{32}$$

where

$$f_h(\alpha) = \begin{cases} \cos \alpha, & \text{if } k \text{ is even.} \\ \sin \alpha, & \text{if } k \text{ is odd.} \end{cases}$$

This representation in terms of α derives from the symmetry of the problem [5].

In a cylindrical coordinate system Ω_x takes the form

$$\Omega_x = \mu \cos \alpha - \sqrt{1-\mu^2}\cos \chi \sin \alpha. \tag{33}$$

Multiplying Eq. (30) by Ω_x, the result is integrated with respect to Ω and the cell volume using Eqs. (31) and (32). From the integral over the cell volume, it is convenient at this point to isolate simply the integral over α. Integration with respect to ρ is performed later. Then it is found that

$$\frac{1}{3\rho} \frac{d}{d\rho} \{\rho\,[\Psi_{as}^{00}(\rho) + 2\Psi_{as}^{20}(\rho) + \sqrt{6}\Psi_{as}^{21}(\rho)]\} + \Sigma_{tr}(\rho)\,[\Psi_{as}^{10}(\rho) + \sqrt{2}\Psi_{as}^{11}(\rho)] = 0. \tag{34}$$

It follows from Eq. (34) that the quantity called the neutron level above is determined by the following expression in cylindrical coordinates

$$\Psi_{as}^{00}(\rho) + 2\Psi_{as}^{20}(\rho) + \sqrt{6}\Psi_{as}^{21}(\rho).$$

635

Now integration of Eq. (34) with respect to ρ from 0 to R gives

$$\frac{R}{\Psi_{as}^{00}(R) + 2\Psi_{as}^{20}(R) + \sqrt{6}\Psi_{as}^{21}(R)} = \frac{1}{3\bar{\Sigma}_{tr}k_j}, \tag{35}$$

where

$$\begin{cases} \bar{\Sigma}_{tr} = \dfrac{\int_0^R d\rho\rho\Sigma_{tr}(\rho)[\Psi_{as}^{10}(\rho) + \sqrt{2}\Psi_{as}^{11}(\rho)]}{\int_0^R d\rho\rho[\Psi_{as}^{10}(\rho) + \sqrt{2}\Psi_{as}^{11}(\rho)]} ; \\[4mm] k_j = \dfrac{\overline{\Psi_{as}^{10}} + \sqrt{2}\,\overline{\Psi_{as}^{11}}}{\Psi_{as}^{10}(R) + \sqrt{2}\Psi_{as}^{11}(R)} ; \\[4mm] \Psi_{as}^{10}(R) + \sqrt{2}\Psi_{as}^{11}(R) = 1. \end{cases} \tag{36}$$

The right-hand side of Eq. (35) coincides — in external form and in the physical meaning of the quantities which it includes — with the expression for the diffusion coefficient in plane, square, and hexahedral cells. Therefore, Eq. (35) is taken as the definition of the diffusion coefficient for a cell with a cylindrical boundary. The result obtained is

$$D = \frac{R}{\Psi_{as}^{00}(R) + 2\Psi_{as}^{20}(R) + \sqrt{6}\Psi_{as}^{21}(R)} \tag{37}$$

and

$$D = \frac{1}{3\bar{\Sigma}_{tr}k_j}. \tag{38}$$

Analyzing a formula of the form in Eq. (38) for all the geometries here considered, the following generalization may be obtained:

$$\begin{cases} \bar{\Sigma}_{tr} = \dfrac{\dfrac{1}{V}\int_V d\mathbf{r}\Sigma_{tr}(\mathbf{r})j_x(\mathbf{r})}{\dfrac{1}{V}\int_V d\mathbf{r}j_x(\mathbf{r})} ; \\[4mm] j_x(\mathbf{r}) = \int_{4\pi} d\Omega\Omega_x\Psi_{as}(w); \\[4mm] k_j = \dfrac{\bar{j}_x}{j_x^{bo}} ; \quad j_x^{bo} = 1; \\[4mm] \bar{j}_x = \dfrac{1}{V}\int_V d\mathbf{r}j_x(\mathbf{r}). \end{cases} \tag{39}$$

Thus, calculating the diffusion coefficient for a cell of arbitrary form involves averaging $\Sigma_{tr}(\mathbf{r})$ over the cell volume with weighting by the neutron flux along the x axis, multiplying by three and by the current-non-uniformity coefficient, and taking the inverse of the result.

Influence of Taking Account of the Second Angular Moments of the Distribution Function at the Cylindrical-Cell Boundary on the Diffusion Coefficient

Calculations are performed for the three cells I, II, III with the characteristics shown in Table 1. Cell I is a microcell (UO_2-H_2O) isolated from the internal region of the RBMK-reactor channel, with constants characteristic of the thermal group. The constants of cell II are characteristic of a narrow fast group. Cell III is a two-zone macrocell of an RBMK reactor. In the first zone of this cell all the materials in the composition of the RBMK channel are homogeneously distributed; the second zone consists of graphite. The constants are characteristic of the thermal group. The constants for cells I and III are taken from [8].

In the calculations, the ORAR-Ts and BENT programs are used. In the ORAR-Ts program, the calculations are performed in the G_3 approximation of the surface-pseudosource method; the diffusion coefficient is

636

determined both with — Eq. (37) — and without — Eq. (4) — taking account of the second moments. In the BENT program, the calculations are performed in the P_4 approximation (the last cell is calculated in the P_2 approximation) for a square grid of elements, disregarding the second moments. The results of calculating the diffusion coefficients are shown in Table 2, together with the values of $1/(3\Sigma_{tr,1})$, $1/(3\Sigma_{tr,2})$. Table 3 gives the maximum (in terms of α) values of the flux and the second moments of the distribution function at the external cell boundary calculated by the ORAR-Ts program for all three cells.

It follows from Tables 2 and 3 that, for small cells (the thickness of the external moderator is approximately equal to the free path length), the effect of taking account of the second moments on the value of the diffusion coefficient is fairly significant. In cell I, Eq. (4) underestimates the diffusion coefficient by 4.8%, and the BENT program by 12%. The influence of the second moments on the diffusion coefficicient is especially large for cell II, which is characterized by very strong relative absorption in the moderator. The overestimation of the diffusion coefficient is 139% by Eq. (4) and 94% by the BENT program. For cell III with thick external moderator (moderator thickness much greater than the free path length), the influence of the second moments on the diffusion coefficient is practically nonexistent.

Note that in the ORAR-Ts program the angular distribution of the neutrons reaching the cell may be changed. This is accomplished by means of a volume source/sink $Q\rho \cos\alpha$, which extends from $\rho = R$ to $\rho = \infty$. Change in P_1 changes the angular distribution of the neutrons reaching the cell; for more details, see [5]. The values of the diffusion coefficient in Table 2 are calculated with $R_1 = \infty$. The influence of the angular distribution of incoming neutrons on the diffusion coefficient has been investigated. For all three cells, P_1 varies from R to ∞. In calculations by Eq. (4), the diffusion coefficient changes smoothly for cell I from 0.29319 to 0.29398, i.e., approximately by 0.3% and for cell II from 2.48590 to 5.79958, i.e., almost twofold; for cell III, it remains practically constant (up to five significant figures). In calculations by Eq. (37), the diffusion coefficient for cells I and II is practically unchanged (up to five significant figures); for cell II, it changes smoothly from 2.45281 to 2.42897, i.e., by less than 1%. Thus, neglecting second moments leads to marked error in the value of the diffusion coefficient in various methods of modeling the real surroundings of the cell. It is particularly important to note, however, that the accurate diffusion coefficient is practically independent of the cell surroundings.

CONCLUSIONS

Specific formulas are obtained for the single-group effective diffusion coefficient used in the SHM equations, for plane, square, hexahedral, and cylindrical cells in terms of the angular moments of the antisymmetric neutron distribution function at the cell boundary. The limits of validity of neglecting the second angular moments are tested. It is shown that, for dense grids, this leads to larger errors, which explains the previously incomprehensible results.

TABLE 1. Cell Parameters

Cell type	Zone No.	External radius, cm	Σ_{tr}, cm^{-1}	Σ_a, cm^{-1}
I	1	0,68	0,6114	0,2455
	2	0,864	2,1318	0,0075
II	1	0,38	0,15604	0,01962
	2	1,27	0,13655	0,109716
III	1	4,4	0,11	1,117
	2	14,105	0,00001	0,38091

TABLE 2. Diffusion Coefficient in Cells

Cell type	$1/(3\Sigma_{tr,1})$	$1/(3\Sigma_{tr,2})$	D		
			ORAR-Ts		BENT P_4, P_2
			Eq. (4)	Eq. (37)	
I	0,54520	0,15636	0,29398	0,30887	0,27185
II	2,13620	2,44111	5,79958	2,42897	4,70182
III	0,29842	0,87510	0,85275	0,85269	0,85470

TABLE 3. Moments of Distribution Function at Cell Boundaries

Cell type	$\psi^{00}_{as}(R)$	$\psi^{20}_{as}(R)$	$\psi^{21}_{as}(R)$
I	2,93893	0,07912	0,00679
II	0,21898	0,09524	0,04629
III	16,54063	0,00343	-0,00230

637

In addition, for any cell geometry, a single formula for the effective single-group diffusion coefficient is obtained:

$$D = \frac{1}{3\Sigma_{tr}k_j}.$$

APPENDIX

It is known that the neutron current is only approximately proportional to the flux gradient. Thus, even in one of the first books on nuclear-reactor theory [9], an expression was given for the generalized Fick's law, from which the value of the second angular moments of the neutron distribution function is evident for the given particular case in determining the neutron current. In addition, in works devoted to the refined boundary conditions in the spherical-harmonic method [10] and in the surface-pseudosource method (see [11], for example), and also in obtaining equations in generalized homogenization theory (see [1, 2], for example), some combination of flux with the second angular moment appears again and again as the basic factor. This entails more careful consideration of this combination and the introduction of a special term for it.

Consider the transfer equation for monoenergetic neutrons in a medium with an isotropic source

$$\Omega\nabla\Psi(w) + \Sigma(r)\Psi(w) = \int \Sigma_s(\Omega'\Omega, r)\Psi(\Omega')\,d\Omega' + S(r), \tag{A.1}$$

Multiplying Eq. (A.1) by Ω_i — the projection of the vector Ω onto axis i of the Cartesian coordinate system — and integrating with respect to Ω, it is found after simple transformations that

$$j_i = -\frac{1}{3\Sigma_{tr}}\nabla_j l_{ij}, \tag{A.2}$$

where j_i is the i-th component of the neutron current and

$$\Sigma_{tr} = \Sigma - \Sigma_s^1; \quad \Sigma_s^1 = \int (\Omega\Omega')\Sigma_s(\Omega\Omega')\,d\Omega;$$

$$l_{ij} = 3 \int \Omega_i\Omega_j\Psi_i(\Omega)\,d\Omega.$$

Summation is implied by the repeating subscripts in Eq. (A.2).

Consider l_{ii}. It is simple to show that $l_{ii} = \Phi_0 + 2\Phi_2$, i.e., the same combination of the flux Φ_0 and the second angular moment $\Phi_2 = \int P_2(\Omega)\Psi_i(\Omega)\,d\Omega$, as mentioned above. Since, as follows from Eq. (A.2), the magnitude and direction of the neutron current are related to the derivatives of the tensor components l_{ij}, it is natural to propose the term neutron-level tensor for the latter, and to call the diagonal elements of this tensor, which are encountered most often, neutron levels.

LITERATURE CITED

1. N. I. Laletin and A. V. El'shin, "Refining the method of homogenizing a heterogeneous reactor," At. Energ., 43, No. 3, 247-251 (1977); N. I. Laletin, "Equations of a heterogeneous reactor," Vopr. At. Nauk. Tekh., Ser. Fiz. Tekh. Yad. Reakt., No. 5(18), 31-46 (1981); N. I. Laletin, "Basic principles for developing equation for heterogeneous reactor — a modification of the homogenization method," Nucl. Sci. Eng., 85, 133 (1983).
2. A. V. El'shin, "Basis and refinement of the method of homogenizing a heterogeneous reactor," Author's Abstract of Candidate's Dissertation, Moscow (1979).
3. N. I. Laletin, in: Proceedings of the Second International Conference on the Peaceful Use of Atomic Energy. Contributions by Soviet Participants [in Russian], Vol. 2, Atomizdat, Moscow (1959), pp. 634-650; G. Ya. Rumyantsev, "Neutron diffusion in a periodic lattice," At. Energ., 13, No. 6, 556-559 (1962).
4. P. Benoist, "Streaming effects and collision probabilities in lattices," Nucl. Sci. Eng., 34, 285 (1968); E. Gelbard, "Anisotropic neutron diffusion in lattices of the zero-power plutonium reactor experiments," Nucl. Sci. Eng., 54, 327 (1974); R. Bonalumy, "A united theory of cell diffusion coefficients," Energ. Nucl., 18, No. 7/8, 718 (1971).
5. V. F. Boyarinov and I. A. Zhokina, Program for the Single-Group Calculation of Antisymmetric Neutron Distributions in a Cylindrical Cell of a Reactor (ORAR-Ts) [in Russian], Preprint IAÉ-3873/5, Institute of Atomic Energy, Moscow (1984).

6. I. S. Grigor'ev and V. M. Novikov, Neutron Diffusion in Heterogeneous Media [in Russian], Atomizdat, Moscow (1966).
7. G. I. Bell and S. Glasstone, Nuclear Reactor Theory, Van Nos Reinhold (1970).
8. Yu. P. Elagin, A. S. Il'yashenko, V. A. Lyul'ka, et al., "Comparison of some methods of calculating neutron fluxes in the technological channel of a reactor," At. Energ., 48, No. 2, 148–153 (1980).
9. S. Glasstone and M. Edlund, Principles of the Theory of Nuclear Reactors [Russian translation], IL, Moscow (1954).
10. V. S. Vladimirov, "Mathematical problems of the single-velocity theory of particle transfer," in: Proceedings of the V. A. Steklov Mathematical Institute, Academy of Sciences of the USSR [in Russian], Izd. Akad. Nauk SSSR, Moscow (1961). G. Ya. Rumyantsev, "Boundary conditions in the spherical-harmonic method," At. Energ., 10, No. 1, 26–29 (1961).
11. N. I. Laletin and N. V. Sultanov, "Development of the surface-pseudosource method for calculating neutron field in cells with a bundle of fuel-element rods," At. Energ., 46, No. 3, 148–152 (1979).

GENERALIZED SUBGROUP APPROACH TO CALCULATING THE RESONANT ABSORPTION OF NEUTRONS

V. V. Tebin and M. S. Yudkevich   UDC 621.039.5

The concept of a subgroup was first introduced in [1]. Further development and use of the subgroup approach [2-5] was aimed at taking account of the resonant self-screening of the cross sections in fast-reactor calculations. In fast reactors, resonant effects appear basically in the high-energy region (the region of unresolved resonances of heavy-element nuclides). Therefore, in obtaining subgroup parameters, a hypothesis valid in this region is used: that energy dispersal in neutron scattering significantly exceeds the width of the resonances and the distance between them (narrow-resonance approximation).

This assumption is adopted in the BNAB system of constants [3], which is widely used for fast-reactor calculations. At the same time, the narrow-resonance model is incorrect in the region of low-lying broad resonances, where the basic resonant capture occurs in thermal reactors.

Special calculations of thermal heterogeneous systems show that, in the region of unresolved resonances, the subgroup approximation introduces an error comparable with the indeterminacy in the microconstants. In this energy range, the BNAB constants [3] may also be used for thermal reactors. Their use in the region of resolved resonances, however, leads to an error of $\sim 10\%$ in the resonant absorption [6]. The error in individual groups reaches 30%.

In the present work, a subgroup equation of neutron transfer valid for resonances of arbitrary width is formulated. The problem of obtaining subgroup parameters in the approximation of a constant (in units of lethargy) collision density for neutrons of a single subgroup is considered.

Subgroup Kinetic Equation

The resonant energy region is divided into intervals (groups). The boundaries of the groups are determined as in the ordinary group method, i.e., so that, for the whole class of problems considered, absorption and leakage of neutrons does not lead to significant difference in the fluxes of decelerating neutrons at the group boundaries. Note, first of all, that for typical thermal reactor grids this condition is always satisfied if the group interval of lethargy $\Delta u \sim 1$.

The basic idea of the subgroup approach is that, within the limits of the group, all the neutrons at energies such that the total cross sections are enclosed in the interval $\Delta\sigma_t^i = \{\sigma^{i-1}, \sigma^i\}$, $\sigma^0 = \min\limits_{u \in \Delta u} \sigma_t(u)$ are assigned to the same spatial–angular distribution. In the absorbing units of the thermal heterogeneous reactor, the spatial distribution of neutrons is basically determined by singly colliding neutrons, and the scattering anisotropy at resonant heavy-element nuclides in the intermediate energy range is small. Therefore, in the group, all the neutrons with energies at which the total cross sections of resonant nuclides are equal have approximately the

639

same spatial—angular distribution. This allows the idea of the subgroup approach to be used in calculations of resonant absorption in thermal heterogeneous reactors.

The integral equation of neutron transfer will now be written in the subgroup formulation. First, the following definitions are introduced.

1. The subgroup of neutrons i of nuclide k — denoted by either (i, k) or i below — is called the set of all neutrons in the group with energies at which the total cross section of this nuclide belongs to the specified interval $\Delta \sigma_t^i k$.

2. The subgroup neutron flux at point $\mathbf{r}$ in the direction Ω is called the integral — over the subgroup (i, k) — flux $\Phi^{i,k}(\mathbf{r}, \Omega)$ normalized to unit lethargy.

3. The neutron subgroup is characterized by the complete subgroup cross section $\sigma_t^{(i,k)}$ and the fractions of the subgroup in group $a^{(i,k)}$. The value of $\sigma_t^{(i,k)}$ inside $\Delta \sigma_t^{(i,k)}$ is determined by averaging the total cross section and the limit as $\sigma^{i-1} \to \sigma^i$ is σ^i. The fraction of the subgroup is the relative part of the group integral of the lethargy in which all the neutrons belong to this subgroup, i.e., $\sum_{i=1}^{I} a^{(i,k)} = 1$, where I is the total number of subgroups in the group. Partial subgroup cross sections are determined from the condition of conservation of the number of processes for each reaction x in each subgroup

$$\sigma_x^{(i,k)} = A_x^{(i,k)}(\mathbf{r}, \Omega)/\Phi^{(i,k)}(\mathbf{r}, \Omega). \tag{1}$$

4. The relative fraction of the neutrons in subgroup (j, l) also belonging to subgroup (i, k) is called the correlation coefficient of subgroup j of nuclide l relative to subgroup i of nuclide k (denoted by $\alpha[(j, l), (i,k)]$ or $\alpha[j, i]$). From the definitions it follows that $\sum_{j=1}^{J} \alpha[(j,l),(i,k)] = 1$, and $\alpha[(j,k),(i,k)] = 0$.

5. The subgroup scattering function is the probability that the neutrons of subgroup (j, l) of group m after scattering on nuclide l will belong to subgroup (i, k) of group n (denoted by $\omega[(j, l),(i,k)]$ or $\omega[j,i]$). In addition, the quantity $\eta_{m,n}^{[l,(i,k)]}$ is introduced; this is the probability that the neutron, after scattering in group m on nuclide l, will belong to subgroup i of nuclide k in group n, that is

$$\eta_{m,n}^{[l,(i,k)]} = \sum_{j=1}^{J} \omega_{m,n}^{[(j,l),(i,k)]}.$$

The balance equation for neutrons of subgroup (i, k) in group n at point $\mathbf{r}$ traveling in the direction Ω is now written. It is assumed that the sources from the other groups $Q_{m,n}^{(i,k)}(\mathbf{r}, \Omega)$ and at the surface of the given volume $T_n^{(i,k)}(\mathbf{r}_S, \Omega)$ are known. Proceeding as in the derivation of the ordinary transfer equation, it is found that

$$\Phi^i(\mathbf{r}, \Omega)\Sigma_t^i + \Phi^i(\mathbf{r}, \Omega)\sum_{l \neq k}^{L}\sum_{j}^{J}{}_i^j\alpha^{[j,i]}(\mathbf{r}, \Omega) = \int_V d\mathbf{r}' P^i(\mathbf{r}', \mathbf{r})\left\{\int d\Omega'\sum_l^L\sum_j^J\Phi^j(\mathbf{r}, \Omega)\Sigma_s^j \times\right.$$

$$\left. \times \omega^{[j,i]}(\Omega', \Omega, \mathbf{r}') + Q^i(\mathbf{r}, \Omega)\right\} + \int_S P^i(\mathbf{r}_S, \mathbf{r})T^i(\mathbf{r}_S, \Omega)d\mathbf{r}_S. \tag{2}$$

Here the index of the group and the nuclide is omitted; $\Sigma_t^i = \sigma_t^i \rho^k$; ρ^k is the concentration of nuclide k; Σ_s^j is the macroscopic scattering cross section in subgroup j of one of the nuclides l, including k; $P^i(\mathbf{r}', \mathbf{r})$ is the probability that a neutron of subgroup (i, k) produced at point $\mathbf{r}'$ will undergo its first collision at point $\mathbf{r}$.

Exhausting all the possible values $1 \leq k \leq L$ and $1 \leq i \leq I$ gives a closed system of equations.

Different groups are related through the sources

$$Q_n^i(\mathbf{r}', \Omega) = \int d\Omega'\sum_m^M\sum_l^L\sum_j^J\Phi_m^j(\mathbf{r}', \Omega')\Sigma_{s,m}^j(\mathbf{r}')\,\omega_{m,n}^{[j,i]}(\Omega', \Omega, \mathbf{r}'). \tag{3}$$

640

Determining the group functionals from the values of the subgroup fluxes means calculating sums of the type

$$A_x(\mathbf{r}, \Omega) \quad \Delta u \sum_i^{I} \sum_j^{J} \sigma_{x\phi}^{j}{}^{I}(\mathbf{r}) \Phi^{j}(\mathbf{r}, \Omega) a^{j}. \tag{4}$$

To solve Eq. (2), it is necessary to know the subgroup parameters, which, in turn, depend on the neutron spectrum. In this sense, the subgroup approach is no different from other means of solving the kinetic equation by determined methods, for example, the group or multigroup approaches. Thus, taking account of the general laws, the weighted spectrum must be found for obtaining "universal" (in the given class of problems) subgroup parameters σ_t^i, a^i, σ_x^i, $\alpha^{[j,i]}\omega^{[j,i]}$. The problem of calculating the resonant absorption in cells of thermal heterogeneous reactors is considered.

Determining the Subgroup Parameters

To elucidate the most general laws of the resonant-neutron distribution in cells of thermal reactors, a large series of calculations has been performed by the Monte Carlo method [6-8]. The results confirm that, in a broad range of variation of the cell parameters, the spatial distribution of the collision density of neutrons of a single group is basically determined by the value of the total cross section. This provides a basis for assuming, in obtaining the subgroup parameters, that the energy dependence of the collision density is a function only of σ_t. The dependence of the collision density is approximated by a piecewise-constant function. Analysis is performed with fixed boundaries for 26 groups, with the aim of matching with the existing libraries of BNAB constants [3].

The assumption of constant collision density in the subgroup is sufficient to determine the boundaries of the subgroups and find all the subgroup parameters. It may be used for a mixture of resonant nuclides because of the extremely rare coincidence of resonances of the latter. Violations of the hypothesis of constant collision density within the limits of the subgroup restricts the region of application of the parameters obtained. Two similar examples are considered below.

The derivation of the criteria for selecting the subgroup boundaries and the method of obtaining subgroup parameters was outlined in detail in [9]. Only the conditions which determine the subgroup division in the group are considered here.

Systematic transition from the Peierls integral equation to the subgroup equation of neutron transfer is now undertaken. Consider the simplest composition of a heterogeneous medium: an absorbing unit or resonant nuclide surrounded by weakly absorbing moderator. Attention is confined to the energy range where there are no sources of fission neutrons and inelastically scattered neutrons. Elastic scattering is assumed to be spherically symmetric in the laboratory coordinate system. Then the neutron collision density in the unit $\Psi(u, \mathbf{r})$ conforms to the equation

$$\Psi(u, \mathbf{r}) = \int_{V_{un}} d\mathbf{r}' P(u, \mathbf{r}', \mathbf{r}) \int_{u-\delta u}^{u} \frac{\sigma_s(u')}{\sigma_t(u')} \Psi(u', \mathbf{r}') W(u' \to u) du' + \int_{V_{mod}} d\mathbf{r}' P(u, \mathbf{r}', \mathbf{r}) Q_s(u, \mathbf{r}'), \tag{5}$$

where $W(u' \to u)$ is the elastic-scattering function; δu is the maximum energy threshold in elastic scattering; $Q_s(u, \mathbf{r}')$ is the source of neutrons with lethargy u in the moderator; V_{un}, V_{mod} are the volume of the unit and the moderator.

A probabilistic method of specifying the cross sections may be used to achieve transition to the subgroup form [1]. In this case, the differentials du and $d\sigma_t$ may be related

$$du/\Delta u = a(\sigma_t) d\sigma_t, \tag{6}$$

where $a(\sigma_t)$ is the distribution density of the probability of having a cross section σ_t inside the group; Δu is the width of the group.

Assuming that the collision density depends on $\mathbf{r}$ in the same way for different values of σ_t, and transforming from the independent variable u to $\sigma_t(u)$ in Eq. (5), it is found that

$$\Psi(\sigma_t, \mathbf{r}) = \int_{V_{un}} d\mathbf{r}' P(\sigma_t, \mathbf{r}', \mathbf{r}) \int_{\sigma_{min}}^{\sigma_{max}} \frac{\sigma_s(\sigma_t')}{\sigma_t'} \Psi(\sigma_t', \mathbf{r}') \times$$

$$\times W(\sigma_t' \to \sigma_t, \delta u) a(\sigma_t') d\sigma_t' + \int_{V_{mod}} d\mathbf{r}' P(\sigma_t, \mathbf{r}', \mathbf{r}) Q_s(\sigma_t, \mathbf{r}'). \tag{7}$$

641

TABLE 1. Comparison of the Results of Calculating the Resonant Absorption by the Monte Carlo Method (A_{MC}) with Those Obtained on the Basis of the Generalized Subgroup Approach (A_{SA})

Variant No.	Unit composition, (nucleus/cm³)· 10^{-24}	diameter, cm	Moderator composition, (nucleus/cm³)· 10^{-24}	step, cm	A_{MC}*	A_{SA}	$\frac{A_{MC} - A_{SA}}{A_{MC}} \cdot 100$
1	²³⁸U	0,2	H₂O	0,4	0,1666 (8)	0,1654	—1,0
2		1,0		1,2	0,375 (2)	0,378	+0,8
3		1,0		2,0	0,1045 (5)	0,1052	+0,6
4	0,0473	4,0	0,0333	10	0,0331 (2)	0,340	+3,0
5	²³⁵U	0,5	H₂O	2,0	0,220 (3)	0,222	+1,0
6		1,0		4,0	0,151 (1)	0,151	0,0
7	0,0473	2,0	0,0333	7,0	0,1197 (6)	0,1198	+0,1
8	²³²Th	1,0	H₂O	4,0	0,0105 (1)	0,0104	—1,0
9		1,6		7,0	0,0071 (1)	0,0069	—2,8
10	0,0293	4,0	0,0333	12	0,0106 (1)	0,0106	0,0
11	²³⁸U	0,376	C	3,27	0,134 (1)	0,131	—2,2
12		1,0		4,0	0,345 (4)	0,341	—1,2
13	0,0473	1,0	0,1	8,0	0,101 (1)	0,099	—2,0
14		0,76		1,27	0,1264 (6)	0,1234 (0,1265)	—2,4 (+0,03)
15	²³⁸UO₂	2,0	H₂O	7,0	0,0166 (1)	0,0158 (0,0164)	—4,8 (—1,2)
16	0,0228	6,0	0,0333	10	0,0627 (3)	0,0597 (0,0626)	—11,1 (—0,2)

* The notation 0.1666(8) means 0.1666 + 0.0008, where 0.0008 is the mean square deviation in calculations by the Monte Carlo method.

where $W(\sigma'_t \to \sigma_t, \delta u)$ is the generalized scattering function (the probability that the neutron, after scattering in the energy range where the total cross section is σ'_t, passes to the region where the total cross section is σ_t).

The region of variation of the total cross section is divided into I intervals within which neutrons are combined into a single subgroup, assuming that $\Psi(\sigma_t, r) \equiv \Psi^i(r)$ for this subgroup. Integrating Eq. (7) with weights $a(\sigma_t)$ within the limits of each interval $\Delta\sigma^i_t$, a system of equations relating the subgroup collision densities in the unit is obtained

$$\Psi^i(r) = \int_{V_{un}} dr \sum_j^J \Psi^j(r) < P(\sigma_t, r', r) \left\langle \frac{\sigma_s(\sigma'_t)}{\sigma'_t} \widetilde{W}(\sigma'_t \to \sigma_t \delta u) \right\rangle_j \rangle_i a^j +$$

$$+ \int_{V_{mod}} dr' \langle P(\sigma_t, r', r) Q_s(\sigma_t, r') \rangle_i, \qquad (8)$$
$$i = 1, 2, \ldots, I;$$

where

$$a^j = \int_{\sigma^{j-1}}^{\sigma^j} a(\sigma_t) d\sigma_t;$$

$$\langle \psi(\sigma_t) \rangle_j \equiv \psi^j = \frac{1}{a^j} \int_{\sigma^{j-1}}^{\sigma^j} \psi(\sigma_t) a(\sigma_t) d\sigma_t,$$

and $\varphi(\sigma_t)$ is any function of σ_t defined within the group interval.

Analogously, an expression is obtained for the number of processes x in the group

$$A_x(r) = \sum_i^I \Psi^i(r) \left\langle \frac{\sigma_x(\sigma_t)}{\sigma_t} \right\rangle_i a^i. \qquad (9)$$

The following conditions must be satisfied in order to reduce Eqs. (8) and (9) to subgroup form, as in Eq. (2):

642

$$\left\langle \frac{\sigma_x}{\sigma_t} \right\rangle_i = \frac{\langle \sigma_x \rangle_i}{\langle \sigma_t \rangle_i} ; \tag{10a}$$

$$\left\langle P \left\langle \frac{\sigma_s}{\sigma_t} \tilde{W} \right\rangle_j \right\rangle_i = \langle P \rangle_i \frac{\langle \sigma_s \rangle_i}{\langle \sigma_t \rangle_i} \langle\langle \tilde{W} \rangle_j \rangle_i; \tag{10b}$$

$$\langle P Q_s \rangle_i = \langle P \rangle_i \langle Q_s \rangle_i. \tag{10c}$$

This is also the criterion for the selection of the boundaries of the subgroups σ^i. The error of Eq. (10a) is completely determined by the number of subgroups and the position of the boundaries σ^i.

Taking account of Eq. (10a), Eq. (10b) is well satisfied for elastic scattering in the interresonance region, thanks to the smoothness of the function $P(\sigma_t)$. In the region of sharp variation in total cross section, the error in Eq. (10b) will be minimal if the width of each energy interval within which the total cross section is continuous and belongs to a single subgroup is less than the maximum energy loss on scattering. This may be achieved by choosing the boundaries σ^i.

The condition in Eq. (10c) holds since the collision density in the moderator depends only weakly on the lethargy. When the moderator in the thermal reactor is hydrogen, Eq. (10c) holds practically precisely.

In [9], the selection of the subgroup boundaries and the determination of the values of σ_t^i, σ_x^i, a^i are based on reducing the error of Eqs. (10a)–(10c) to a permissible level. Furthermore, the additional condition

$$P(\langle \sigma_t \rangle_i, \; r', \; r) \approx \langle P(\sigma_t, \; r', \; r) \rangle_i \tag{10d}$$

is imposed, allowing the value σ_i^t to be used in calculating the probabilities of the first collisions and also allowing the whole apparatus of the method of first–collision probabilities developed for single–velocity problems to be applied.

In [9], the relation was found between the required accuracy of calculating the resonant absorption and the necessary number of subgroups in the group. For example, it is sufficient to have 6–8 subgroups in the group in order to calculate the resonant absorption at ^{238}U in the region of resolved resonances with an error of no more than 3%.

The calculation of the subgroup parameters $\alpha^{[j, i]}$ and $\omega^{[j, i]} = \langle\langle \tilde{W} \rangle_j \rangle_i a^j$, under the assumption of constant collision density in the subgroup with known boundaries σ^i, is sufficiently obvious, and follows from their definitions. It is only necessary to note that the subgroup scattering function in transitions between subgroups of different nuclides may be found from the values of the correlation coefficients and the subgroup scattering function transitions between subgroups of the same nuclide

$$\omega^{[(i, h), (j, l)]} = \sum_{(j, h)}^{J^h} \alpha^{[(j, h), (j, l)]} \omega^{[(i, h), (j, h)]}. \tag{11}$$

The parameters of the generalized subgroup approach σ_t^i, σ^i, a^i, $\sigma_x^i (x = c, e, f)$, $\alpha^{[(j, l), (i, k)]}$, $\omega^{[(j, k), (i, k)]}$ for the basic nuclides determining the resonant-neutron spectrum in thermal reactors are obtained from the SERP program [9].

The number of subgroups is chosen from the condition of calculating the resonant absorption with an error of no more than 3% using a 26–group division [3]. This ensures the introduction of newly obtained parameters as a supplement to the BNAB–78 library [3]. However, note that, as shown in [9], the constant–collision–density approximation is also valid for broader groups in the case of thermal reactors.

Results of Numerical Testing

Table 1 gives the comparison of the results of calculating resonant absorption in regular grids by the Monte Carlo method (MONR1 program [10]) and in the subgroup approximation. The initial information on detailed resonant cross sections in both cases is identical (CROS program [11]).

The resonant absorption is calculated in the energy ranges 465–4.65 eV for ^{238}U, 100–1 eV for ^{235}U, 2150–10 eV for ^{232}Th. The diameter of the central unit, its composition, the triangular grid step, and the moderator material are varied. It is evident that the calculation error in the subgroup approximation for most variants is not more than the 3% established in obtaining the subgroup parameters. In addition, it may be noted that, except for variants 4, 14–16, the selection criterion for the number of subgroups in the SERP program gives an upper bound of the estimate. The calculation error for these variants is due to violation of the condition of constant neutron collision density for a single subgroup. For variant 4, the violation occurs in internal layers of the

643

thick unit: because of strong attenuation of the neutron flux from the moderator, the collision density at an energy less than the resonant energy is markedly different from that at an above-resonant energy. With further increase in diameter of a metallic-uranium unit, the error does not rise, since the fraction of neutrons absorbed in the internal layers decreases.

The pronounced error arises for UO_2 units. This is a result of the nonasymptotic oscillations of the collision density in the region of broad scattering resonances [12]. This is of practical interest for thermal reactors when the resonant nuclides of heavy elements are diluted by nonresonant nuclides of light elements [8]. Under the assumption of constant collision density, the subgroup function for transitions after scattering on a nonresonant nuclide to the subgroup of a resonant nuclide is equal to the fraction of the subgroup of the resonant nuclide.

Nonasymptotic oscillation leads to a redistribution of probability between the subgroups. In [8, 9], an effective method of taking account of the nonasymptotic oscillations of the collision density was proposed. On the basis of solving the precise equations of moderation in the model problem (homogeneous mixture of resonant nuclides with a light moderator at a source equal to the absorption at each energy point) corrections to the subgroup fractions are obtained. They are used in forming the subgroup scattering function in transitions from the nonresonant nuclide to the subgroup of the resonant nuclide

$$\omega_{m,n}^{[l,(i,k)]} = a_n^{(i,k)} f_n^{[l,(i,k)]} \eta_{m,n}^{[l,l]}, \tag{12}$$

where $f^{[l,(i,k)]}$ is the correction to the nonasymptotic oscillations; $\eta_{m,n}^{[l,l]}$ is the probability that the neutron enters group n after scattering on the nonresonant nuclide l in group m.

Table 1 gives the results of calculation using the corrections $f^{[l,(i,k)]}$ in parentheses for variants 14-16; these results show the possibility of using the effective method in cases that are of practical interest.

The generalized subgroup approach outlined here is convenient for computer realization on account of the single method of solution in the regions of unresolved and resolved resonances and the presence of a sufficiently complete library of constants. At the same time, this approach is also sufficiently economical. For example, the computation time for a single variant from among those shown in Table 1 is 10-15 sec on the BÉSM-6 computer.

LITERATURE CITED

1. M. N. Nikolaev and V. V. Filippov, "Variation in resonant-structure parameters of the cross sections of some elements at high neutron energies 0.3-2.7 MeV," At, Energ., 15, No. 6, 493-498 (1963).
2. M. N. Nikolaev, A. A. Ignatov, N. V. Isaev, and V. F. Khokhlov, "Subgroup method for taking account of the resonant structure of cross sections in neutron calculations. I, II," At. Energ., 29, No. 1, 11-16 (1970); 30, No. 5, 426-430 (1971).
3. L. P. Abagyan, N. O. Bazazyants, M. N. Nikolaev, and A. M. Tsibulya, Group Constants for Calculating Reactors and Protection [in Russian], Énergoizdat, Moscow (1981), p. 231.
4. V. V. Sinitsa and M. N. Nikolaev, "Analytical method of obtaining subgroup parameters," At. Energ., 35, No. 5, 429-430 (1973).
5. V. V. Korobeinikov and M. N. Nikolaev, "Calculating effects of resonant heterogeneity by the Monte Carlo method," Vopr. At. Nauk. Tekh., Ser. Yad. Konst., No. 22, 103-118 (1976).
6. V. V. Korobeinikov, A. G. Sboev, and V. V. Tebin, "Modeling experiments on the variation in the resonant integral of ^{238}U by the Monte Carlo method," Vopr. At. Nauk. Tekh., Ser. Yad. Konst., No. 4(35), 52-61 (1979).
7. V. V. Tebin, "Results of calculating the resonant absorption of neutrons by the Monte Carlo method in some reactor cells with water moderator," Vopr. At. Nauk. Tekh., Ser. Fiz. Tekh. Yad. Reakt., No. 9(22), 19-59 (1981).
8. V. V. Tebin and M. S. Yudkevich, "Taking account of the energy dependence of the collision dependence due to resonant scattering in calculating group cross sections," Vopr. At. Nauk. Tekh., Ser. Yad. Konst., No. 1(36), 81-88 (1980).
9. V. V. Tebin and M. S. Yudkevich, Subgroup Parameters in the Region of Resolved Resonances [in Russian], Preprint IAÉ-3395/5, Institute of Atomic Energy, Moscow (1981), p. 32.
10. A. G. Sboev, "Program for calculating the resonant absorption of neutrons in reactor cells by the Monte Carlo method: MONR-1," Vopr. At. Nauk. Tekh., Ser. Fiz. Tekh. Yad. Reakt., No. 5(18), 91-96 (1981).
11. V. V. Tebin and M. S. Yudkevich, "Calculating neutron cross sections from estimated resonant parameters," Vopr. At. Nauk. Tekh., Ser. Yad. Konst., No. 2(29), 2-7 (1978).

12. A. A. Luk'yanov, Moderation and Absorption of Resonant Neutrons [in Russian], Atomizdat, Moscow (1974), p. 360.

INFLUENCE OF STATISTICAL CORRECTION ON THE RESULT
OF SOLVING THE RADIANT-TRANSFER EQUATION

Yu. I. Balashov, V. V. Bolyatko,
A. I. Ilyushkin, V. P. Mashkovich,
V. I. Savitskii, and A. A. Stroganov

In [1], a method was proposed for taking account of the influence of the statistical character of the indeterminacies in the initial data on the result of solving the radiant-transfer equation. The result is understood here to mean the linear functional of the radiation flux density (dose, heat liberation, activation, radiation damage of the material, etc.), and initial data to mean the interaction cross section (group constants), functions specifying the radiation source and the detector response, etc.

When the initial parameters ("transport" group parameters) include statistical indeterminacies, the result of the calculation depending on these parameters must also be regarded as a statistical quantity with some mean value and dispersion. In [1], it was noted that the mean value of the result of the calculation may differ from the result obtained with mean values of the initial group constants. The following quantity is taken as the characteristic of this difference

$$\omega_R = \frac{\overline{R(x_1, x_2, \ldots, x_N)}}{R\,\overline{x_1},(\,\overline{x_2}, \ldots, \overline{x_N})},$$ (1)

and is called the statistical correction, where $\overline{R(x_1, x_2, \ldots, x_N)}$ is the mean value of the result of the calculation; $R(\overline{x_1}, \overline{x_2}, \ldots, \overline{x_N})$ is the result obtained with mean values of the "transport" group constants.

It is important that $\omega_R > 1$ for the radiant-transfer problem in the shielding. If $\overline{R(x_1, x_2, \ldots, x_N)}$ is regarded as the result of experimental determination of the functional and $R(\overline{x_1}, \overline{x_2}, \ldots, \overline{x_N})$ as a result of calculation, the amount by which the theoretical result is less than the experimental (true) value may be estimated. In [1], a method for estimating ω_R was proposed, on the basis of the mathematical apparatus of sensitivity analy-

TABLE 1. Comparison and Correction of the Results of Calculations and Experiments on the TSF Apparatus

Composition No.	Layer thickness, cm			Data of [6]			Present work		
	stainless steel	sodium	carbon steel	$\frac{C}{E}$	$\frac{C_1}{E}$	σ_D	σ_R	ω_R	$\omega_R \frac{C}{E}$
1	47	0	0	1,00	1,07	—	—	—	—
2	47	155	0	0,90	1,05	10	10	1,01	0,90
3	47	309	0	0,78	0,84	29	30	1,04	0,81
4	47	309	15	1,04	0,94	38	39	1,07	1,12
5	47	309	31	1,13	1,29	44	46	1,10	1,24
6	47	309	41	0,87	1,52	47	50	1,12	0,97
7	47	309	62	0,75	1,37	47	50	1,12	0,84
8	47	460	0	0,84	0,73	54	58	1,16	0,97
9	47	460	15	1,54	0,95	64	71	1,23	1,89
10	47	460	31	1,82	1,38	63	70	1,21	2,22
11	47	460	41	0,46	0,80	74	85	1,31	0,60
12	47	460	51	0,30	0,74	76	88	1,33	0,40
13	47	460	62	0,30	0,75	75	90	1,35	0,40
14	31	460	0	0,88	0,80	50	53	1,13	1,00
15	31	460	15	1,51	1,07	57	62	1,18	1,78
16	31	460	31	1,38	1,42	57	62	1,18	1,62
17	31	460	41	0,82	1,24	51	68	1,21	0,99
18	31	460	51	0,77	1,26	64	71	1,23	0,95
19	31	460	62	0,76	1,26	65	73	1,24	0,94
20	31	460	72	0,77	1,30	65	73	1,24	0,95
21	31	460	82	0,73	1,25	66	74	1,24	0,91
22	31	460	90	0,70	1,20	67	75	1,25	0,88

TABLE 2. Statistical Correction ω_R for a Composition with a Sodium Layer (4.6 m) and an Iron Layer (0.9 m)

Neutron spectrum	Function of radiation field			
	φ_f (E ≥ 1.4 MeV)	P_{equ}	P	1/v detector
$f+1/E$ INC	7,5 4,9	1,5 2,0	1,5 2,0	1,5 2,0

TABLE 3. Constant Component of Error in the Activation of Sodium for the Model of the Lateral Shielding of a Fast Reactor, %

Process	Sodium	Iron	Carbon
Capture	10,5	1,13	—
Elastic scattering	15,9	9,34	7,45
Inelastic scattering	1,92	3,72	—
Sum over the process	19,2	10,1	7,45

sis [2, 3], the PARF method [1], and the assumption of a normal distribution law of the initial parameters. The expression obtained for the statistical correction is

$$\omega_R = \exp\left(\frac{1}{2}\,\sigma_{R_{LPT}}^2\right), \tag{2}$$

where

$$\sigma_{R_{LPT}}^2 = \sum_n \sum_{n'} p_n p_{n'} \sigma_n \sigma_{n'} \rho_{nn'}; \tag{3}$$

$\sigma_{R_{LPT}}^2$ is the relative error of calculation of the functional in the approximation of linear perturbation theory (LPT); p_n, $p_{n'}$ are the relative sensitivities of R to the parameters x_n and $x_{n'}$; σ_n, σ_n', are the relative errors of x_n and $x_{n'}$; $\rho_{nn'}$ is the correlation coefficient of x_n and $x_{n'}$.

The introduction of statistical correction with the aim of correcting the results of calculations and improving the agreement with experiment for problems of deep penetration by radiation is illustrated below. Estimates of the values of ω_R in one-, two-, and three-layer compositions and for test multilayer models of the lateral shielding of fast reactors of integral compositions are given [4-6].

As an example, the results of miscalculation of the data of the basic experiments at the Oak Ridge National Laboratory on the TSF apparatus are corrected [6]. The composition consists of alternating layers of stainless steel, sodium, and carbon steel. The measurements are made by Bonner derectors. The results of the correction are shown in Table 1, which gives the ratio of data calculated by the DOT III program in the 51-group energy approximation (C) to experimental data (E); the ratio of data calculated by the DOT III program and corrected with respect to the ratio of the theoretical data according to the ANISN program in the 171- and 51-group approximations (C_1) to the experimental data (E); the standard deviation of the result of the calculation due to errors in the differential data only σ_D (corresponding to $\sigma_{R_{LPT}}$ in [6]); the standard deviation determined by the PARF method σ_R [1]; the statistical correction ω_R found from Eq. (2); the ratio of calculation to experiment corrected taking account of the statistical correction ω_R.

On the basis of Table 1, it may be concluded that it is important to take account of the statistical correction ω_R in problems of deep penetration by radiation; the method proposed here improves the agreement of the theoretical and experimental data for compositions with a thick last layer in which asymptotic conditions are established; this is a necessary condition for the possibility of using Eq. (2). Introducing the correction ω_R for compositions 6-8, 14, 17-22 markedly improves the agreement between theoretical and experimental data.

In contrast to the method used in [6], where the correction of the cross sections at least improves agreement between the theoretical and experimental data, but may lead to physically unreal values of the group cross sections, the introduction of the statistical correction in the result of the calculation takes account of the physical laws of error formation. It was noted in [6] that, although there was improvement in agreement between the theoretical and experimental data, the corrections to the cross sections here were found to be twice as large as expected. This was attributed to the presence of shifts of systematic errors in the constants. In fact, this may be partially explained by the constant ω_R. Therefore, it is proposed here that ω_R be introduced to take account of some of the statistical component of the error in calculating the functional (unrelated to the fitting error of the group cross sections). The importance of this is confirmed by the data of Table 1.

In some cases, the statistical shift in the result of the calculation may be small against the background of the error introduced in fitting the macroscopic constants (for example, that associated with taking account of the resonant structure of the cross sections). This is especially evident in the transition regions (compositions 9, 10, 15, 16).

646

Estimates of ω_R are made for one- and two-layer spheres of sodium and iron with a point isotropic source at the center with the energy spectrum of an intermediate-neutron converter (INC) [7] and a fission spectrum at neutron energies $E \geq 2.5$ MeV as well as a spectrum of the form $1/E$ at $E \leq 2.5$ MeV $(f+1/E)$. Table 2 gives estimates of ω_R for a spherical composition with a sodium layer (4.6 m) and an iron layer (0.9 m) in calculating the flux density of fast neutrons φ_f ($E \geq 1.4$ MeV), the absorbed skin dose rate P, the equivalent dose P_{equ}, and the detector readings $1/v$, where v is the neutron velocity. The relative errors in the calculation results due to the errors in the interaction cross sections $\sigma_{R_{LPT}}$ are taken from [7].

Note that ω_R depends not only on the error of the interaction cross sections but also indirectly, through the sensitivity coefficients, on the energy distribution of the source and the response function of the detector. If this is taken into account, the results in Table 2 may be understood. For example, for a fast-neutron flux there is a significant difference in the values of p_n for the $(f+1/E)$ and INC spectra, determining the difference in the values of ω_R.

It follows from the data of Table 2 that failure to take account of the statistical indeterminacies in the interaction cross section leads to approximately 7.5-fold underestimation of the fast-neutron flux. For the remaining functionals, the theoretical data may be too low by half.

On the basis of the data on the error in calculating the activation of sodium in a test model of the lateral shielding of a reactor proposed in [5], the statistical correction for calculations with ENDF-B/IV and ENDF-B/V data are estimated: in the first case, the relative error $\sigma_D = 69\%$, $\omega_R = 1.3$; in the second, $\sigma_D = 65\%$; $\omega_R = 1.2$.

Calculations of the test model of the lateral shielding of a reactor of integral composition [4] have been carried out. Information on the sensitivity of the calculation results is obtained from the ZAKAT program [7]; analysis of the errors in accordance with Eq. (3) is based on the CORE program [8], using LUND-12 files of the errors and correlations of the interaction cross sections [8, 9]. Table 3 gives a partial (with respect to the type of neutron interaction with matter and with respect to the various elements appearing in the composition of the protection) component of the error in calculating the activation of second-loop sodium. The total constant component of the error is 23%; the statistical correction $\omega_R = 1.04$.

In conclusion, it remains to thank G. N. Manturov and I. N. Kachanov for useful discussions.

LITERATURE CITED

1. Yu. I. Balashov, V. V. Bolyatko, A. M. Zhezlov, et al., "Statistical correction of the result of calculating radiation-transfer problems," At. Energ., 55, No. 2, 99-102 (1983).
2. L. N. Usachev, "Perturbation theory for the reproduction coefficient and other number ratios of various processes in the reactor," At. Energ., 15, No. 6, 472-481 (1963).
3. E. Oblow, General Sensitivity Theory for Radiation Transport, ORNL-TM-4110 (1973).
4. V. I. Savitskii, One-Dimensional Test Models of the Shielding of Fast Power Reactors [in Russian], Preprint FÉI-1290, Physics and Power Institute, Obninsk (1982).
5. M. Salvatores and C. Palniotti, "International LMFBR shielding benchmark intercomparison and analysis," in: Proceedings of the Sixth International Conference on Radiation Shielding, Tokyo (May 16-20, 1983); JAERI, 1, 34 (1983).
6. E. Oblow and C. Weisbin, "Fast reactor sensitivity studies for steel−sodium−iron systems," in: Proceedings of the Fifth International Conference on Reactor Shielding, Science Press, Princeton (1977), p. 140.
7. V. V. Bolyatko, M. Yu. Vyrskii, A. I. Ilyushkin, et al., Error of Calculations of Radiation Shielding [in Russian], Énergoatomizdat, Moscow (1983).
8. G. N. Manturov, Software for Problems of Analyzing the Sensitivity of Reactor Characteristics to Nuclear Constants [in Russian], Preprint FÉI-1034, Physics and Power Institute, Obninsk (1980).
9. L. P. Abagyan, N. O. Bazazyants, M. N. Nikolaev, et al., Group Constants for Calculating Reactors and Shielding [in Russian], Énergoatomizdat, Moscow (1981).

SURFACE-PSEUDOSOURCE METHOD FOR CALCULATING THE ANTISYMMETRIC SINGLE-GROUP NEUTRON DISTRIBUTION IN A CYLINDRICAL REACTOR CELL

V. F. Boyarinov

If such cell characteristics as the effective transport cross section (Σ_{tr}) or the neutron diffusion coefficient (D) are to be correctly obtained, it is necessary to know how to calculate the antisymmetric neutron distributions in the cells. In the present work, a method of calculating such distributions in the single-group approximation is proposed.

Formulation of the Problem

A multizone cylindrical cell is considered. The neutron distribution in zone h of the cell is described by the single-group neutron-transfer equation in the transport approximation

$$\Omega \nabla \Psi_h(w) + \Sigma_{tr}^h \Psi_h(w) = \frac{\Sigma_{s,tr}^h}{4\pi} \Psi_h^0(r) + S(r), \tag{1}$$

where $w = (r, \Omega)$; $\Psi_h^0(r) = \int_{4\pi} d\Omega\, \Psi_h(r, \Omega)$; $r = \rho = (\rho, \alpha)$; S (r) is an external source.

At the external boundary of the cell, the value of the neutron current flowing in the direction of the x axis is specified

$$\int_{4\pi} d\Omega\, (\Omega i_x)\, \Psi_H(R, \alpha, \Omega) = T;$$

$$\int_{4\pi} d\Omega\, (\Omega i_y)\, \Psi_H(R, \alpha, \Omega) = 0, \tag{2}$$

where R is the external radius of the cell; H is the number of final (external) zones of the cell; i_x and i_y are unit vectors in the direction of the x and y axes, respectively. It follows from Eq. (2) that the function $\Psi(w)$ must be symmetric relative to the x axis. In addition, only the part of $\Psi(w)$ that is antisymmetric with respect to x is of interest. Hence, the function $\Psi(w)$ must satisfy the following two conditions

$$\Psi(\rho, \alpha, \Theta, \chi) = \Psi(\rho_+, -\alpha, \Theta, \pi - \chi);$$
$$\Psi(\rho, \alpha, \Theta, \chi) = -\Psi(\rho, \pi - \alpha, \Theta, \pi - \chi), \tag{3}$$

where $\Theta = \arccos(\Omega \rho / \rho)$; χ is the angle between the planes (Ω, ρ) and (x, y). This coordinate system was used in [1]. Conditions of the form in Eq. (3) must also be satisfied by the source S(r). Equations (1)–(3) determine the antisymmetric single-group distribution of the neutrons in a multizone cylindrical reactor cell.

Using the Surface-Pseudosource Method to Calculate Single-Group Antisymmetric Neutron Distributions in a Cylindrical Cell

According to the surface-pseudosource method (SPM) [2], the solution of Eq. (1) in zone h of a multizone cylindrical cell takes the form

$$\Psi_h(w) = \Psi_h^s(w) + \Psi_h^q(w) + \Psi_Q(w)\, \delta_{h,H}, \tag{4}$$

where $\Psi_h^S(w)$ is the neutron distribution in an infinite homogeneous medium of the material of zone h from source $S_h(\mathbf{r})$; $\Psi_h^g(w)$ is the neutron distribution in an infinite homogeneous medium of the material of zone h from the surface pseudosources of this zone; $\Psi_Q(w)$ is the neutron distribution in an infinite homogeneous medium of the material of zone H from some volume neutron source/sink $Q(w)$ placed in the region from $\rho = R_1 \geq R$ to $\rho = \infty$; source/sink $Q(w)$ is necessary to satisfy Eq. (2) at the external cell boundary.

An expression is now written for the moments of the function $\Psi_h(w)$, which will be used below

$$M_h^{nk}(\rho) = \begin{cases} 1/\pi \int_0^{2\pi} d\alpha \cos\alpha \int_{4\pi} d\Omega\, Y_n^h(\Omega)\, \Psi_h(w), \\[2pt] n = 0, 1, \ldots;\ k = 0, 2, \ldots, 2\,[n/2]; \\[6pt] 1/\pi \int_0^{2\pi} d\alpha \sin\alpha \int_{4\pi} d\Omega\, Y_n^h(\Omega)\, \Psi_h(w), \\[2pt] n = 1, 2, \ldots;\ k = 1, 3, \ldots, 2\,[n/2] + 1, \end{cases} \tag{5}$$

where [x] is the integer part of the number x; and

$$Y_h^n(\Omega) = \sqrt{\frac{(n-k)!}{(n+k)!}}\, P_n^h(\mu)\cos k\chi;$$

$\mu = \cos\Theta$. Each of the three terms in Eq. (5) is now considered in more detail.

Function $\Psi_h^S(w)$. Writing the source $S_h(\mathbf{r})$ in the form of a series in trigonometric functions of the axial angle $\overline{\alpha}$ and requiring that it satisfy the condition in Eq. (3), it is found that

$$S_h(\mathbf{r}) = \sum_{n=1,3\ldots} S_{h,n}(\rho)\cos n\alpha.$$

Retaining only the first term in this expansion, and specifying the spatial dependence $S_{h,1}(\rho)$ in the form $S_{h,1}(\rho) = S^h \rho_b\ (\rho_b = \rho \Sigma_{tr}^h)$, it follows that

$$S_h(\mathbf{r}) = S^h \rho_b \cos\alpha. \tag{6}$$

The particular solution of Eq. (1) from the source in Eq. (6) satisfying Eq. (3) is obtained in the Appendix, and takes the form

$$\Psi_h^s(w) = \frac{S^h}{4\pi\Sigma_a^h}\{\cos\alpha\,[\rho_G Y_0^0(\Omega) - Y_1^0(\Omega)] - \sin\alpha \sqrt{2}\, Y_1^{-1}(\Omega)\}. \tag{7}$$

The expression for the moments of the function $\Psi_h^S(w)$ is

$$M_{h,s}^{nk}(\rho) = \frac{S^h}{\Sigma_a^h}\left[\rho_b \delta_{n0}\delta_{k0} - \frac{1}{3}\delta_{n1}\delta_{k0} - \frac{1}{3\sqrt{2}}\delta_{n1}\delta_{k1}\right]. \tag{8}$$

Function $\Psi_h^g(w)$. The following expression may be written for $\Psi_h^g(w)$

$$\Psi_h^g(w) = \sum_j (G^h(w/w_j'),\ g_j[\alpha', \Omega]), \tag{9}$$

where $w_j' = \{\rho_j', \alpha', \Omega'\}$; j is the number of sides of the boundary

$$j = \begin{cases} 1, & h = 1; \\ 2h-2,\ 2h-1, & h \neq 1, H; \\ 2H-2, & h = H; \end{cases}$$

$$\rho_{2h-1}' = \rho_{2h}' = \rho_h,\quad h = 1, 2, \ldots, H-1;$$

$$(G^h(w/w_j'),\ g_j[\alpha', \Omega']) = \int_0^{2\pi} d\alpha' \int_{4\pi} d\Omega'\, G^h(w/w_j')\, g_j(\alpha', \Omega');$$

$G^h(w/w_j')$ is the Green's function of Eq. (1) [3, 4]; $g_j(\alpha, \Omega)$ are surface pseudosources.

Writing $g_j(\alpha, \Omega)$ in the form

$$g_j(\alpha, \Omega) = \sum_{p=0,1\ldots}\ \sum_{n=1,3\ldots}\ \sum_{k=0,1\ldots} Y_n^k(\Omega)\ [\cos p\alpha g_{j,\,pc}^{nk} + \sin p\alpha g_{j,\,ps}^{nk}],$$

649

retaining two terms in the expansion with respect to α ($p = 0$, 1), and requiring that the pseudosource $g_j(\alpha, \Omega)$ satisfy conditions of the form in Eq. (3), it is found that

$$g_j(\alpha, \Omega) = \sum_{n=1, 3\ldots} \sum_{h=0, 1\ldots} Y_n^h(\Omega) g_j^{nh} f_h(\alpha),$$

(10)

where

$$g_j^{nh} = \begin{cases} g_{j,\,1c}^{nh}, & \text{if } k \text{ is even} \\ g_{j,\,1s}^{nh}, & \text{if } k \text{ is odd;} \end{cases}$$

$$f_h(\alpha) = \begin{cases} \cos\alpha, & \text{if } k \text{ is even} \\ \sin\alpha, & \text{if } k \text{ is odd.} \end{cases}$$

Substituting Eq. (10) and the expression for $G^h(w/w_j')$ from [3] into Eq. (9), and taking account of Eq. (3), it is found that

$$\Psi_h^g(w) = \sum_{n,\,h} \frac{2n+1}{2\pi(1+\delta_{h0})} Y_n^h(\Omega) f_h(\alpha) \sum_{j,\,n',\,h'} G_{n'h'}^{nh}(\rho/\rho_j') g_j^{n'h'},$$

(11)

where $G_{n'h'}^{nk}(\rho/\rho_j')$ are the moments of the Green's function, expressions for which were given in [4].

The expression for the moments of $\Psi_h^g(w)$ is

(12)

$$M_{n,\,g}^{nh}(\rho) = \sum_{j,\,n',\,k'} G_{n'h'}^{nh}(\rho/\rho_j') g_j^{n'h'}.$$

Function $\Psi_Q(w)$. The source/sink $Q(w)$ is introduced at some distance from the cell center $\rho = R_1 \geq R$ so that Eq. (2) is satisfied at the external boundary of the cell. Taking into account that $Q(w)$ must satisfy conditions of the form in Eq. (3), it is chosen in the form

$$Q(R_1, \alpha, \Omega) = Q_c(R_1) Y_1^0(\Omega) \cos\alpha + Q_s(R_1) Y_1^1(\Omega) \sin\alpha.$$

(13)

Choosing $Q(w)$ in the form in Eq. (13) allows the conditions at the external boundary to be accurately satisfied. The choice of R_1 allows the real surroundings of the cell to be modeled in different ways, which influences the angular distribution of the neutrons reaching the cell. This source/sink is used in the first version of the ORAR-Ts program.

It is found that a source/sink of the form in Eq. (13) does not permit transition to the limit as $R_1 \to \infty$, since in this case the two constants Q_c and Q_s degenerate to one. Using one constant, however, it is impossible to satisfy Eq. (2) precisely. Therefore, when R_1 is equal to a few free path lengths in the external zone of the cell, there is loss of accuracy. Therefore precise satisfaction of Eq. (2) is not attained. It is expedient to introduce the volume source/sink $Q(w)$ in the region from $\rho = R_1 \geq R$ to $\rho = \infty$, in the form

$$Q(w) = Q\rho_b\cos\alpha, \quad \rho \in [R_1, \infty], \quad R_1 \geq R.$$

(14)

The source/sink of the form in Eq. (14) satisfies Eq. (3) and allows the conditions at the external cell boundary in Eq. (2) to be approximately satisfied; precise satisfaction of Eq. (2) is impossible with one constant Q. The solution $\Psi_Q(w)$ from a source/sink of the form in Eq. (14) takes the form

$$\Psi_Q(w) = Q \sum_{n,\,k} \frac{2n+1}{2\pi(1+\delta_{k0})} Y_n^k(\Omega) f_h(\alpha) G_Q^{nk}(\rho),$$

(15)

$$\rho < R_1,$$

where

$$G_Q^{nk}(\rho) = \int_{R_1}^{\infty} d\rho' \, \rho'\rho_b' G_{00}^{nk}(\rho/\rho') = -R_1 \int_v dv \frac{1}{N(v)} K_2\left(\frac{R_{b,\,1}}{v}\right) \begin{cases} \Phi_{h0}^{n1}\left(\frac{\rho_b}{v}\right), & \text{if } k \text{ is even} \\ -\Phi_{h0}^{n1}\left(\frac{\rho_b}{v}\right), & \text{if } k \text{ is odd} \end{cases}$$

(16)

and the notation of [3, 4] is used.

650

The expression for the moments of $\Psi_Q(w)$ takes the form

$$M_Q^{nk}(\rho) = Q G_Q^{nk}(\rho). \tag{17}$$

Passing to the conditions at the external cell boundary, Eq. (2) takes the following form in cylindrical coordinates

$$\int_{4\pi} d\Omega\,(\Omega n)\,\Psi_H(R,\,\alpha,\,\Omega) = T\cos\alpha; \tag{18}$$

$$\int_{4\pi} d\Omega\,(\Omega\tau)\,\Psi_H(R,\,\alpha,\,\Omega) = -T\sin\alpha,$$

where n is the external normal to the cylindrical surface at the point $(R,\,\alpha)$; τ is the unit vector at the point $(R,\,\alpha)$ directed counterclockwise along the tangent to the cylindrical surface.

As already noted, the condition in Eq. (2) or Eq. (18) cannot be precisely satisfied using a source/sink of the form in Eq. (14). Therefore, Eq. (18) is satisfied approximately, dealing only with the normal (and most important) component of the neutron flux. Thus, the condition at the external cell boundary which is realized by a source/sink of the form in Eq. (14) takes the form

$$\int_{4\pi} d\Omega\,(\Omega n)\,\Psi_H(R,\,\alpha,\,\Omega) = T\cos\alpha. \tag{19}$$

Taking into account that $(\Omega n) = Y_1^0(\Omega)$, Eq. (19) is rewritten in the form

$$\tag{20}$$

$$\int_{4\pi} d\Omega\,Y_1^0(\Omega)\,\Psi_H(R,\,\alpha,\,\Omega) = T\cos\alpha.$$

Substituting $\Psi_H(w)$ into Eq. (20), the following expression is obtained for the unknown constant Q

$$Q = \frac{1}{G_Q^{10}(R)}\left[T + \frac{1}{3\Sigma_a^H}S^H - \sum_{n',\,k'} G_{n'k'}^{10}(R/\rho'_{2H-2})\,g_{2H-2}^{n'k'}\right]. \tag{21}$$

Substituting Eq. (21) into Eq. (15) gives

$$\Psi_Q(w) = \frac{1}{G_Q^{10}(R)}\left(T + \frac{1}{3\Sigma_a^H}S^H\right)\sum_{n,\,k}\frac{2n+1}{2\pi(1+\delta_{n0})}Y_n^k(\Omega)f_k(\alpha)G_Q^{nk}(\rho) -$$

$$\tag{22}$$

$$- \frac{1}{G_Q^{10}(R)}\sum_{n,\,k}\frac{2n+1}{2\pi(1+\delta_{n0})}Y_n^k(\Omega)f_k(\alpha)G_Q^{nk}(\rho)\sum_{n',\,k'}G_{n'k'}^{10}(R/\rho'_{2H-2})\,g_{2H-2}^{n'k'}.$$

Finally, for $\Psi_h(w)$, the following expression is obtained

$$\Psi_h(w) = \sum_{n,\,k}\frac{2n+1}{2\pi(1+\delta_{k0})}Y_n^k(\Omega)f_k(\alpha)\sum_{j,\,n',\,k'}F_{n'k'}^{nk}(\rho/\rho'_j)\,g_j^{n'k'} +$$

$$\tag{23}$$

$$+ S^h D_1^{nk}(\rho) + \delta_{h,\,H}T D_T^{nk}(\rho)\Big],$$

where the notation introduced is

$$F_{n'k'}^{nk}(\rho/\rho'_j) = G_{n'k'}^{nk}(\rho/\rho'_j) - \frac{G_Q^{nk}(\rho)\,G_{n'k'}^{10}(R/\rho'_{2H-2})}{G_Q^{10}(R)}\delta_{h,\,H};$$

$$D_1^{nk}(\rho) = \frac{1}{\Sigma_a^h}\left[\rho_0\delta_{n0}\delta_{k0} - \frac{1}{3}\delta_{n1}\delta_{k0} - \frac{1}{3\sqrt{2}}\delta_{n1}\delta_{k1}\right] + \frac{G_Q^{nk}(\rho)\,\delta_{hH}}{3\Sigma_a^H G_Q^{10}(R)};$$

$$\tag{24}$$

$$D_T^{nk}(\rho) = \frac{G_Q^{nk}(\rho)}{G_Q^{10}(R)}.$$

The expression for the moments of $\Psi_h(w)$ takes the form

$$M_h^{nk}(\rho) = \sum_{j',\,n',\,k'}F_{n'k'}^{nk}(\rho/\rho'_j)\,g_j^{n'k'} + S^h D_1^{nk}(\rho) + \delta_{h,\,H}T D_T^{nk}(\rho). \tag{25}$$

Equating the moments of the distribution function at the boundaries between the zones, an infinite system of boundary conditions is obtained

$$M_h^{nk}(\rho_h) = M_{h+1}^{nk}(\rho_h), \quad h = 1, 2, \ldots, H-1. \tag{26}$$

Breaking off the infinite system in Eq. (26) at n (n ≤ N), the G_N approximation of SPM is obtained. In Eq. (26), identical numbers of moments with respect to cos α and sin α are equated: in the G_1 approximation (n, k) = (0, 0), (1, 0), (1, 1), (2, 1); in the G_3 approximation (n, k) = (0, 0), (1, 0), (2, 0), (2, 2), (3, 0), (3, 2), (1, 1), (2, 1), (3, 1), (3, 3), (4, 1), (4, 3).

Solving Eq. (26) in the G_N approximation, the moments of the surface pseudosources are determined. Knowing the values of the surface-pseudosource moments, the moments of the distribution function at any point of the cell may be calculated.

Using the Matrix-Factorization Method

One of the advantages of SPM is that it is short-range, that is, the neutron distribution in each specific zone is determined by the neutron sources in that zone and the pseudosources at the boundaries of the zone, and does not depend on the sources in other zones nor on the pseudosources at the boundaries of other (including adjacent) zones. As a result, the pseudosources of only two adjacent zones (three boundaries) are related in each equation of the system in Eq. (26). Consequently, Eq. (26) lends itself to the application of the method of matrix factorization (fitting) [5]. In [6, 7], the matrix-factorization method was used in solving SPM problems to calculate symmetric distributions. The modification described in [7] is found to be most convenient and most natural. It may be used to solve Eq. (26). First, Eq. (26) is written in a form convenient for factorization

$$-\hat{A}_h g_{h+1} + \hat{B}_h g_h - \hat{C}_h g_{h-1} = D_h, \tag{27}$$
$$k = 1, 2, \ldots, H-1,$$

where the matrix elements $\hat{A}_k$, $\hat{B}_k$, $\hat{C}_k$ are combinations of the moments of the Green's function; $\hat{C}_1 = \hat{0}$ and $\hat{A}_{H-1} = 0$; D_k is a vector whose elements are combinations of $S^h D_1^{nk}(\rho_h)$ and $T D_T^{nk}(\varphi_h)$; the vector g_k includes all the moments of the surface pseudosources on the two sides of one boundary (boundary k). The form in Eq. (27) is expedient in that the matrix elements $\hat{B}_k$ must be close in value, since they consist of moments of the Green's function for a single boundary, and this leads to stable calculation. In accordance with the matrix-factorization method [5]

$$g_h = \hat{E}_h g_{h+1} + F_h, \quad k = 1, 2, \ldots, H-1, \tag{28}$$

where

$$\hat{E}_1 = \hat{B}_1^{-1} \hat{A}_1;$$
$$\hat{F}_1 = \hat{B}_1^{-1} D_1; \tag{29}$$
$$\hat{E}_{H-1} = \hat{0}$$

and

$$\hat{E}_h = [\hat{B}_h - \hat{C}_h \hat{E}_{h-1}]^{-1} \hat{A}_h;$$
$$F_h = [\hat{B}_h - \hat{C}_h \hat{E}_{h-1}]^{-1} [D_h + \hat{C}_h F_{h-1}]. \tag{30}$$

Equations (28)–(30) determine the vector g. Using the matrix-factorization method to solve Eq. (26) allows the time for computer calculation to be reduced.

ORAR-Ts Program

The above algorithm has been realized in the ORAR-Ts program. The program calculates the single-group antisymmetric neutron distributions in a cylindrical reactor cell with a specified current at the external cell boundary in the G_1 and G_3 approximations of the SPM. To operate the program, the VORAR-Ts executive program is written; the VORAR-Ts program introduces the initial data and calls the ORAR-Ts program. In addition, from the results of ORAR-Ts calculation, the effective cell diffusion coefficient is calculated in VORAR-Ts. ORAR-Ts is written in Algol-GDR.

652

TABLE 1. Diffusion Coefficients of Cells

Cell No.	Zone No.	Σ_a, cm^{-1}	Σ_{tr}, cm^{-1}	ORAR-Ts		P_4	
				$R_1 = R$	$R_1 = \infty$	square grid	triangular grid
1	1	0,5	0,8	0,24824	0,24824	0,22982	0,23361
	2	0,02	2,02				
2	1	1,0	1,3	0,21212	0,21207	0,20344	0,20584
	2	0,02	2,02				
3	1	2,0	2,3	0,17399	0,17392	0,17192	0,17266
	2	0,02	2,02				
4	1	4,0	4,3	0,14800	0,14790	0,14506	0,14440
	2	0,02	2,02				
5	1	0,02	2,02	0,16590	0,16589	0,16766	0,16769
	2	0,02	2,02				

Calculation Results

Comparative calculations of the effective diffusion coefficient have been carried out for five two-zone cells with external zone radii $r_1 = 0.3$ cm and $r_2 = 0.42003$ cm. Calculations are performed by the ORAR-Ts program in the G_3 approximation of SPM with the two limiting angular distributions of the neutrons reaching the cell which may be realized in this program ($R_1 = R$ and $R_1 = \infty$). The diffusion coefficient in the VORAR-Ts program is determined from the formula

$$D = \frac{R}{\Psi^{00}(R) + 2\Psi^{20}(R) + \sqrt{6}\,\Psi^{21}(R)}, \qquad (31)$$

where $\Psi^{nk}(R) = M_H^{nk}(R)$. Equation (31) is accurate with known values of $\Psi^{nk}(R)$. Calculations are also performed in the P_4 approximation of the spherical-harmonic method for square and triangular lattices. The diffusion coefficient is calculated without taking account of the second moments of the antisymmetric distribution function at the cell boundaries. The material parameters of the cell and the results of the calculations are shown in Table 1.

The basic reason for the difference between the diffusion coefficients calculated by the ORAR-Ts program and in the P_4 approximation is that, in the latter case, the diffusion coefficient is calculated from an approximate formula in which the influence of the second angular moments of the antisymmetric distribution function is neglected. It follows from Table 1 that the effective diffusion coefficient of the cell calculated from Eq. (31) — the ORAR-Ts program — is almost independent of the angular distribution of the incoming neutrons.

APPENDIX

Particular Solution of the Single-Group Neutron-Transfer

Equation from the Source $\rho \cos \alpha$

The single-group neutron-transfer equation in a cylindrical coordinate system used in [1] with a source $\rho \cos \alpha$ takes the form

$$\mu \frac{\partial}{\partial \rho}\Psi(w) + \frac{(1-\mu^2)\cos^2\chi}{\rho}\frac{\partial\Psi(w)}{\partial\mu} + \frac{\mu\sin 2\chi}{2\rho}\frac{\partial\Psi(w)}{\partial\chi} + \frac{\sqrt{1-\mu^2}\cos\chi}{\rho}\frac{\partial\Psi(w)}{\partial\alpha} + \Psi(w) = \frac{c}{4\pi}\Psi_0(\rho,\alpha) + \frac{1}{4\pi}\rho\cos\alpha, \quad (A.1)$$

where $w = \{\rho, \alpha, \mu, \chi\}$; the coordinate ρ is measured in units of free path length; $c = \Sigma_s / \Sigma_t$. Only the antisymmetric part of the solution of Eq. (A.1) is considered, i.e., the function $\Psi_s(w)$ must satisfy Eq. (3). Now $\Psi_s(w)$ is found in the form

$$\Psi_s(w) = \cos\alpha\,[a_c(\mu,\chi) + b_c(\mu,\chi)\rho] + \sin\alpha\,[a_s(\mu,\chi) + b_s(\mu,\chi)\rho]. \qquad (A.2)$$

Substituting Eq. (A.2) into Eq. (A.1) and equating terms with identical powers of ρ (ρ^{-1}, ρ^0, ρ^1), the following system is obtained

$$(1-\mu^2)\cos^2\chi\left[\cos\alpha\frac{\partial a_c(\mu,\chi)}{\partial\mu} + \sin\alpha\frac{\partial a_s(\mu,\chi)}{\partial\mu}\right] + \frac{\mu\sin 2\chi}{2}\left[\cos\alpha\frac{\partial a_c(\mu,\chi)}{\partial\chi} + \sin\alpha\frac{\partial a_s(\mu,\chi)}{\partial\chi}\right] +$$

$$+ \sqrt{1-\mu^2}\cos\chi\,[-\sin\alpha\,a_c(\mu,\chi) + \cos\alpha\,a_s(\mu,\chi)] = 0;$$

653

$$\mu \cos \alpha b_c (\mu, \chi) + \mu \sin \alpha b_s (\mu, \chi) + (1 - \mu^2) \cos^2 \chi \left[\cos \alpha \frac{\partial b_c (\mu, \chi)}{\partial \mu} + \sin \alpha \frac{\partial b_s (\mu, \chi)}{\partial \mu} \right] + \frac{\mu \sin 2\chi}{2} \left[\cos \alpha \frac{\partial b_c (\mu, \chi)}{\partial \chi} + \sin \alpha \frac{\partial b_s (\mu, \chi)}{\partial \chi} \right] +$$

$$+ \sqrt{1 - \mu^2} \cos \chi \left[- \sin \alpha b_c (\mu, \chi) + \cos \alpha b_s (\mu, \chi) \right] + \cos \alpha a_c (\mu, \chi) + \sin \alpha a_s (\mu, \chi) = \frac{c}{4\pi} [\cos \alpha a_c^{00} + \sin \alpha a_s^{00}];$$

$$\cos \alpha b_c (\mu, \chi) + \sin \alpha b_s (\mu, \chi) = \frac{c}{4\pi} [\cos \alpha b_c^{00} + \sin \alpha b_s^{00}] + \frac{\cos \alpha}{\pi}. \qquad \text{(A.3)}$$

From the last relation in Eq. (A.3), in view of the orthogonality of the trigonometric functions with respect to α, it follows that

$$\begin{cases} b_c (\mu, \chi) = \frac{1}{4\pi} (1 + c b_c^{00}); \\ b_s (\mu, \chi) = \frac{c}{4\pi} b_s^{00}. \end{cases} \qquad \text{(A.4)}$$

Integrating Eq. (A.4) with respect to (μ, χ) and assuming that $c \neq 1$, it is found that

$$\begin{cases} b_c^{00} = \frac{1}{1-c}; \\ b_s^{00} \quad 0, \end{cases}$$

and hence

$$\begin{cases} b_c (\mu, \chi) = \frac{1}{4\pi (1-c)}; \\ b_s (\mu, \chi) = 0. \end{cases} \qquad \text{(A.5)}$$

Substituting Eq. (A.5) into the second relation in Eq. (A.3), it is found that

$$\frac{\mu \cos \alpha}{4\pi (1-c)} - \sin \alpha \frac{\sqrt{1 - \mu^2} \cos \chi}{4\pi (1-c)} + \cos \alpha a_c (\mu, \chi) + \sin \alpha a_s (\mu, \chi) = \frac{c}{4\pi} [\cos \alpha a_c^{00} + \sin \alpha a_s^{00}],$$

and hence, in view of the orthogonality of the trigonometric functions, it is found that

$$a_c (\mu, \chi) = \frac{1}{4\pi} \left[c a_s^{00} - \frac{\mu}{1-c} \right] \qquad \text{(A.6)}$$

$$a_s (\mu, \chi) = \frac{1}{4\pi} \left[c a_s^{00} + \frac{\sqrt{1 - \mu^2} \cos \chi}{1-c} \right].$$

Integrating Eqs. (A.6) with respect to (μ, χ) for $c \neq 0$ yields $a_C^{00} = a_S^{00} = 0$, whence

$$a_c (\mu, \chi) = - \frac{\mu}{4\pi (1-c)} = - \frac{Y_1^0 (\mu, \chi)}{4\pi (1-c)};$$

$$a_s (\mu, \chi) = \frac{\sqrt{1 - \mu^2} \cos \chi}{4\pi (1-c)} = - \frac{\sqrt{2} Y_1^1 (\mu, \chi)}{4\pi (1-c)}. \qquad \text{(A.7)}$$

Substituting Eqs. (A.5) and (A.7) into the first relation in Eq. (A.3) yields an identity.

Thus, the particular solution of Eq. (A.1) takes the form

$$\Psi_s (w) = \frac{1}{4\pi (1-c)} [\cos \alpha (\rho - \mu) + \sin \alpha \sqrt{1 - \mu^2} \cos \chi] \qquad \text{(A.8)}$$

or

$$\Psi_s (w) = \frac{1}{4\pi (1-c)} \{\cos \alpha [\rho Y_0^0 (\Omega) - Y_1^0 (\Omega)] - \sin \alpha \sqrt{2} Y_1^1 (\Omega)\}. \qquad \text{(A.9)}$$

LITERATURE CITED

1. N. I. Laletin, "Green's function of the neutron-transfer equation for problems with cylindrical symmetry," At. Energ., 26, No. 4, 370 (1969); N. I. Laletin, "Elementary solutions of the single-velocity neutron transfer equation," in: Methods of Calculating the Thermal-Neutron Fields in Reactor Grids [in Russian], Atomizdat, Moscow (1974), p. 155.

654

2. N. I. Laletin, Surface-Pseudosource Method for Solving Neutron-Transfer Equations [in Russian], Preprint IAÉ-374, Institute of Atomic Energy, Moscow (1967); N. I. Laletin, "Surface-pseudosource method for solving neutron-transfer equations," in: Methods of Calculating the Thermal-Neutron Fields in Reactor Grids [in Russian], Atomizdat, Moscow (1974), p. 187.

3. N. I. Laletin and N. V. Sultanov, Green's Function of the Neutron-Transfer Equation for Cylindrical Geometry with Azimuthal Asymmetry [in Russian], Preprint IAÉ-2265, Institute of Atomic Energy, Moscow (1973).

4. N. V. Sultanov, Development of Surface-Pseudosource Method for Calculating Neutron Fields in RBMK-Reactor Cells [in Russian], Preprint IAÉ-3005, Institute of Atomic Energy, Moscow (1978).

5. G. I. Marchuk and V. I. Lebedev, Numerical Methods in the Theory of Neutron Transfer [in Russian], Atomizdat, Moscow (1981).

6. V. F. Boyarinov, Program for Neutron Group Calculation of a Plane Periodic Cell of a Reactor by a Difference Analog of the Surface-Pseudosource Method (NEGR-PR) [in Russian], Preprint IAÉ-3582/5, Institute of Atomic Energy, Moscow (1982).

7. N. V. Sultanov, Single-Velocity Calculation of Cylindrical Cells with a Strongly Absorbing Annular Zone [in Russian], Preprint IAÉ-3988/4, Institute of Atomic Energy, Moscow (1984).

EFFECTS OF THE CONTAINMENT CHAMBER
OF A HIGH-TEMPERATURE GAS-COOLED REACTOR
ON THE CORE

A. M. Bogomolov, A. V. Zhirnov,   UDC 621.039.51
V. A. Zavorokhin, A. S. Kaminskii,
V. V. Paramonov, and V. M. Talyzin

The presence of an erection clearance between the upper end of the reflector and the core of a high-temperature gas-cooled reactor with spherical fuel elements has a considerable influence on the neutron and physical characteristics of the reactor. In order to investigate this effect and test design methods and programs, we have carried out a series of experiments on cores using a test rig type GROG [1].

In order to arrive at a "clean" assembly, i.e., a core without additional structural members, and in order to be able to dismantle it rapidly, we erected models of the reactor with their central axes horizontal. Figure 1 shows the core with a clearance height of 50 cm (the distance between the upper end of the reflector and the core). In order to form a chamber in cube-shaped graphite cladding with a 450 cm edge, a series of columns were extracted and replaced with shaped blocks. As a result, a chamber of diameter 320 cm was formed inside the cladding. Four series of columns of total thickness 100 cm at the front of the chamber simulated the upper end of the reflector. A core of the same diameter was formed at the rear of the chamber, together with a zone containing the absorber elements and the lower face of the reflector. The assemblies simulated the start-up charge of the reacor with a cylindrical core that was quasihomogeneous for nonresonant neutrons (less than 10% blocking), 62.5 cm along the axes, burning $^{235}U \sim 6\%$, with a ratio of nuclear concentration of graphite and ^{235}U equal to 9000. The fuel-element system with modules of the universal physical simulator of HT gas-cooled reactor fuel elements

TABLE 1. Spectral Neutron Characteristics

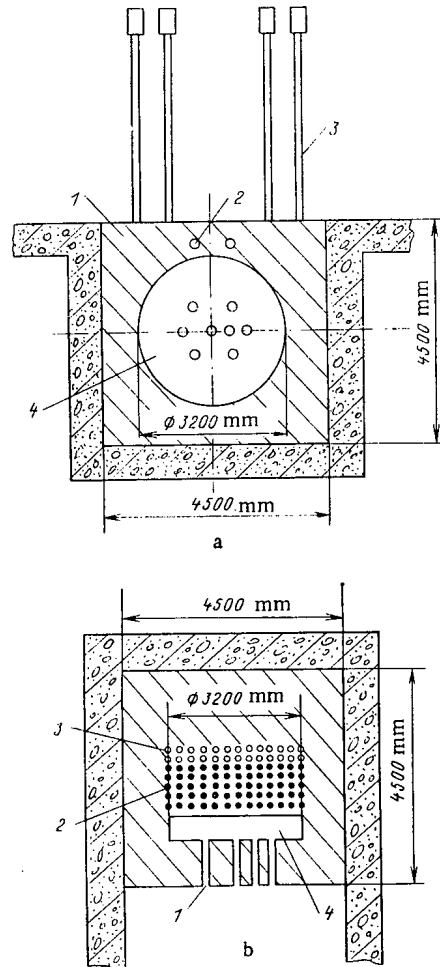| Zone	Neutron gas temp., °K	Rigidity of spectrum	Cadmium ratio
Upper end reflector	340±11	0,016±0,003	50
Chamber (H = 50 cm)	370±12	0,055±0,003	14
Core	480±14	0,086±0,004	8

Figure 1. Diagram of core with 50-cm erection
clearance: a) cross section of chamber along clear-
ance: 1) graphite cladding; 2) channels for horizontal
rods; 3) fault protection rods; 4) clearance; b) cross
section along central axis: 1) channels for horizontal
rods; 2) channels for fuel elements; 3) channels for
absorber rods; 4) clearance.

[2] and modules of the absorber (a homogeneous mixture of boron and aluminum) are installed in vertical channels
of the cladding. The control rods are also mounted in the vertical channels, while the control rods being
studied run in horizontal channels parallel to the central axis.

The investigation was carried out on six assemblies, differing in their clearance heights (0.25 and 50 cm)
and compositions (degrees of blackness) and their absorber zones (two versions). The critical parameters and
the reactivity effect, together with the spectral indices, plutonium coefficient, the mean energy ratio of micro-
scopic ^{238}U capture section and ^{235}U fusion, and the neutron gas temperature were determined during the experi-
ments. The distribution of reaction rate was investigated with the aid of activation detectors [^{63}Cu (n, γ) ^{64}Cu,
^{164}Dy (n, γ) $\times$ ^{165}Dy, ^{176}Lu (n, γ) ^{177}Lu, ^{235}U (n, f)] and by the use of scanning equipment, ensuring the simultaneous
displacement of groups of miniature fission chambers in the assembly and the recording of their signals. When
measuring large reactivity margins, we used the homogeneous contamination method [3], with 10 mm diameter
absorbers containing boron, that enter the cladding with a step of 25 cm. The disturbance in reactivity caused
by a single absorber did not exceed $0.15\beta_{eff}$, which virtually excluded any interference.

The cores and their clearances were designed within the framework of a diffusion approximation, using
two approaches: 1) the clearance is described by means of the effective diffusion constant; 2) the corresponding
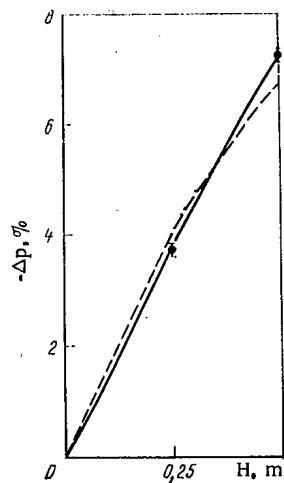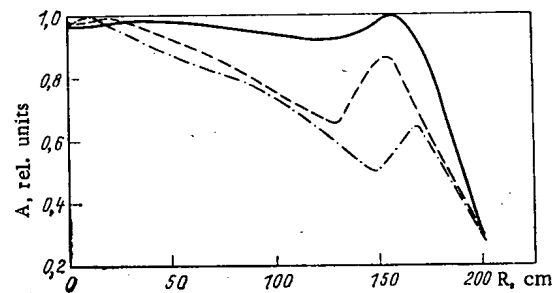conditions at the boundary of the clearance are employed.

656

Fig. 2

Fig. 3

Fig. 2. Relationship of reactivity introduced by the chamber to its height: ●) by experiment; —) by calculation, calculated for anisotropic and isotropic diffusion coefficients in the chamber; ----) by calculation, using the transfer matrix at the boundary with the chamber.

Fig. 3. The effect that the height of the clearance has on the radial distribution of the rate of ^{235}U fission (A) in the upper part of the core when the clearance is: ——) 50 cm; ----) 25 cm; —·—) absent.
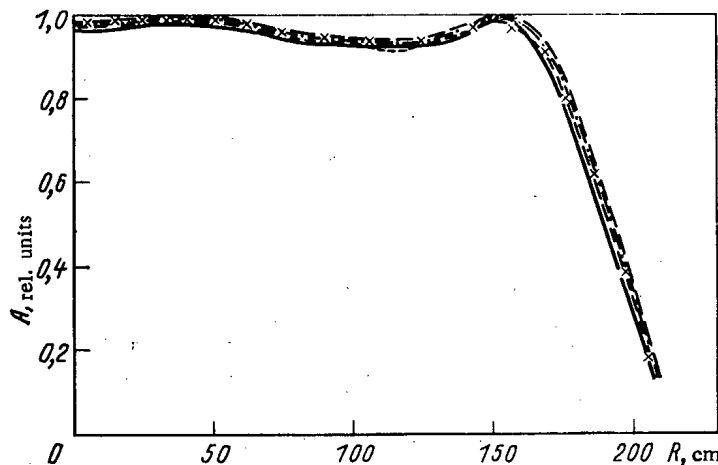

Fig. 4. Radial distribution of rate of ^{235}U fission (A) at the boundary of a core with 50 cm clearance: ——) by experiment; —·—) by calculation using anisotropic diffusion coefficients for the chamber; ----) by calculation using isotropic diffusion coefficients for the chamber; — × —) by calculation employing the transfer matrix at the boundary with the chamber.

The homogenization constants were found by means of a WIMS program [4], with the constant then being corrected in accordance with data obtained from programs PIT [5] and MONR-1 [6], in which the thermalization and resonance effects are taken into consideration with greater accuracy. Calculations by the WIMS program involved equivalent conversion of the geometrical cell [7].

When employing effective diffusion constants, the neutron interaction section in the chamber is assumed to be zero and anisotropic [8] or isotropic diffusion coefficients are introduced instead. We take one third of the mean chord of the chamber as our isotropic diffusion coefficient, i.e., $D = \bar{l}/3 = (1/3)(4V/S)$, where V and S are the volume and surface area of the chamber respectively. The diffusion coefficients in a chamber with absorbing rods are taken as being the same as in a chamber without such rods, since investigations have shown that they have little effect on the neutron and physical characteristics, and the effective chamber constants scarcely change at all when the rods are inserted. When a core having a containment chamber is being designed,

657

we employ the usual methods of representing the control rods in the diffusion calculations (including empty space). The effective neutron multiplication factor k_{eff} and the spatial energy distribution of neutrons in the presence and absence of control rods are determined by the three-dimensional QUM-3-HER program [9]. When the core is being designed without control rods, we can also use the two-dimensional PENAP program [10].

The second approach combines the theory of transfer in the chamber and the theory of diffusion in the main part of the core, employing the corresponding boundary conditions. A neutron transfer matrix M is assumed at the boundary of the chamber to describe the relationship between the one-way flows of neutrons for the diffusion solution: $I_{out} = \hat{M} I_{in}$. Where the chamber is cylindrical in shape and without rods, the neutron transfer matrices for isotropic and linear-isotropic distributions of neutron flux were determined analytically. The elements of the neutron transfer matrix for the chamber can be calculated by the Monte Carlo method for any positioning of the control rods. In this case, the time needed for the calculation is considerably less than would be the case if the whole core were to be calculated by the Monte Carlo method. This approach has been realized in a two-dimensional DOP program [11].

Figure 2 shows the relationship between the reactivity of the assembly and the height of the chamber, while the shape and composition of the remaining zones remain the same. In this case, the relationship is linear. We observed a close similarity between the experimental results and calculated values obtained both when the chamber was described by means of effective constants (the values with anisotropic and isotropic diffusion coefficients being virtually the same) and when the neutron transfer matrix at the boundary of the chamber is used. We should note that the relationship between the reactivity and chamber height becomes less pronounced when a reflector of structural material is fitted at the upper end.

Calculations of k_{eff} for a core in the critical state ($k_{eff} = 1.000 \pm 0.001$), for different combinations of loading in the zone of the horizintal absorber rods that are being studied, show that there is a difference between calculated and experimental values of k_{eff} of 0.1-0.5%. Measuring the spectral characteristics shows a significantly "rigid" neutron spectrum (see Table 1). The presence of the chamber and its size have a slight effect on the neutron spectrum in the core. The calculated values of spectral characteristics lie within 6% of the experimental results.

LITERATURE CITED

1. A. M. Bogomolov, A. S. Kaminskii, A. D. Molodtsov, et al., "Basic characteristics of type GROG critical test rig and problems of studying the physics of the high-temperature gas-cooled reactor," Vopr. At. Nauki Tekh., Ser. At. Vodorodnaya Energ. Tekhnol., No. 3(10), 17-21 (1981).
2. A. M. Bogomolov, A. S. Kaminskii, A. D. Molodtsov, et al., "Fuel element for the core of a reactor," Inventor's Certificate No. 915628, Byull. Izobret., No. 30, 300 (1982).
3. V. A. Pavshuk and V. M. Talyzin, "Measuring the margin in reactivity of a gas-cooled reactor," Vopr. At. Nauki Tekh., Ser. Fiz. Tekh. Yad. Reaktorov, No. 5(18), 105-107 (1981).
4. J. Askew et al., "A general description of the lattice code WIMS," J. Brit. Nucl. Energy Soc., 5, No. 4, 564 (1966).
5. A. S. Kaminskii and L. V. Maiorov, "The PIT program for calculating slow neutrons by the Monte Carlo method, taking thermalization into account," Vopr. At. Nauki Tekh., Ser. Fiz. Tekh. Yad. Reaktorov, No. 8(21), 76-77 (1981).
6. A. G. Sboev, "A program for calculating resonant absorption of neutrons in reactor cells by the Monte Carlo method MONR-1," Vopr. At. Nauki Tekh., Ser. Fiz. Tekh. Yad. Reaktorov, No. 5(18), 91-96 (1981).
7. A. S. Kaminskii, A. G. Morozov, A. G. Sboev, and A. V. Cherepanov, "Some model methods of calculating resonant capture in complex cells," Vopr. At. Nauki Tekh., Ser. Fiz. Tekh. Yad. Reaktorov, No. 6(43), 22-24 (1984).
8. H. Gerwin and W. Sckerer, "Ein diffussions-theoretisches Simulationsverfahren zur Behandlung des oberen Hohlraumes in Kugelhaufen-HTR," 1599 (1979).
9. S. S. Gorodkov, M. I. Gurevich, and N. L. Pozdnyakov, Instructions for Using Program Calculation of Three-Dimensional or Two-Dimensional Heterogeneous Reactor QUM-3-HER, Preprint IAE-2794, Moscow (1977).
10. P. N. Alekseev, S. M. Zaritskii, L. N. Usachev, and L. K. Shishkov, "Program complex TVK-2D," Vopr. At. Nauki Tekh., Ser. Fiz. Tekh. Yad. Reaktorov, No. 4(33), 32-35 (1983).
11. V. F. Tsibul'skii and V. S. Malkov, "Multigroup diffusion program DOP for calculating neutron fields in two-dimensional reactors with containment chambers," Vopr. At. Nauki Tekh., Ser. At.-Vodorodnaya Energ. Tekhnol., No. 3(16), 29-31 (1983).

ANALYZING THE MAXIMUM DESIGN FAULT IN THE CORE
OF A FAST REACTOR

Yu. K. Buksha, Yu. E. Bagdasarov,
L. M. Zabud'ko, and I. A. Kuznetsov

One of the two worst-case design faults for nuclear power stations with fast reactors is the fault involving clogging of the cross section of an individual fuel element, caused by swelling of the element itself, by precipitation of foreign substances from the coolant or by penetration by foreign objects. This leads to a reduction in the flow of coolant through the element and damage, destruction or melting of the fuel element with consequential damage to its immediate surroundings [1]. To satisfy the requirements of Standard OPB-82 on preventing the spread of damage due to a breakdown of normal operation of a fuel element, the whole of the core has to be studied at the different stages in the development of a fault, in order to determine the time characteristics of the process and the danger that the fault situation represents for the reactor as a whole. This allows us to formulate the demands that must be imposed on the monitoring and protection systems of the reactor.

The present article examines some aspects of such a worst-case fault for reactor type BN-600.

The nature of the fault process is determined by the size and position of the blockage. Partial clogging of the passage through the fuel element outside the bounds of the fuel area itself is not particularly dangerous, even when the blockage is of considerable extent. Even a blockage of half the area of the passage through this part of the element only results in a fall of 10% in the flow of sodium. Therefore, the danger of blockage applies to the fuel part of the subassembly.

In recent times, the accumulation of calculated and experimental data, both in the Soviet Union and abroad [2], has made it clear that the blockage of a few cells leads only to an increase in temperature at the point of blockage, without causing the sodium to boil. With blockages encompassing a significant proportion of the cells, a stagnant zone is formed beyond the obstruction, whose length comprises just two diameters of the blockage zone. The average temperature of the sodium in the stagnant zone is below the boiling point, whereas directly beyond the blockage, the temperature of the sodium can reach boiling point. Calculations carried out by the authors into the process of boiling of sodium with overheating of up to 85°C at blockages of 50% of the through section of the fuel part of the element show that the lifetime of the vapor bubble comprises about 0.1 sec, and complete drying out of the surface of the fuel element does not take place.

There is no doubt that the temperature of the can rises above rated and that the sealing of the can may fail with a loss of gas to the interelement environment, depending upon the nature of the process and the number of pulsations of the bubble. These calculations of the boiling process have been confirmed by experiment [3]. Experiments carried out on the DFR reactor involving significant blockage of the through section resulted in boiling of the sodium [4]. These experiments show that the fuel subassembly can operate for several hours under such conditions without catastrophic consequences. We therefore see that even large local blockages do not spread to the fuel subassembly as a whole.

When burnup is complete and the pressure of the gas-forming products of fission is fairly high in the fuel element, while the mechanical properties of the can material have deteriorated due to the high fluence levels, there is a possibility that the sealing of the fuel element will fail. However, the resultant escape of gas will vary depending upon the area of the cracks formed in the can. With microcracks, the escape of the gas-forming fission products will be slow, with small bubbles forming and breaking. Such a situation is not particularly dangerous from the point of view of reducing the flow of sodium and of causing overheating in the fuel element.

Calculation of the thermohydraulic processes taking place in the fuel elements when large breaks have occurred in the fuel can (with areas of 1-2 cm^2) show that almost complete expulsion of gas takes place from the can in the initial stages of the process, during the first few milliseconds. The pressure in the space between

       659

the fuel elements increases considerably above its nominal level. The introduction of gas into this space leads to a short-term rise in the flow rate of sodium at the output and a maintenance of the flow rate in the inlet parts of the subassembly. When the outflow is complete, the flow rate of sodium returns to normal. The bubble now moves towards the outlet, practically at the speed of the sodium itself, with small periodic variations in pressure and in the sizes of the bubbles. As a result, the fuel elements are left without cooling or with inadequate cooling for several hundredths of a second, which is a considerably shorter period than the maximum permissible time for loss of cooling (measured in hundredths of a second). When the sodium circulates by convection, it takes a long time to expell the bubbles (about 2 sec). However, the temperature of the fuel element does not rise very much in this time. Consequently, large breaks in the fuel can or expulsion of bubbles do not in themselves endanger the fuel element, whether at maximum sodium rates or at rates corresponding to convectional circulation.

Reference [5] surveys experimental results on the loss of gas from fuel elements. Various types of loss were investigated, slow and rapid, with various degrees of can failure.

The expulsion of thin fast jets and the rapid expulsion of a large quantity of gas represent some degree of danger. Jets can lead to the formation of "dry" spots on the surface of the adjacent fuel element facing the defective element. Experiments have shown that droplets of liquid are present in the jets which moderate the process, so that the can temperature of the neighboring element does not exceed the permissible level. Furthermore, even when there is a break in the can of the neighboring fuel element at the point where the jet strikes, the fault will not spread further, since any emission from the new break would be directed back towards an already faulted element. We can assume that this type of emission does not lead to the fault propagating and is self-limiting in this respect.

Reference [6] gives the results of experiments with large instantaneous breaks of fuel-element cans holding an initial gas volume of 16.8 cm^3 at a pressure of 15.0 MPa. The following conclusions are drawn: bubbles pass through a region of isolated heat transmission for several tens of milliseconds. Extrapolated to the conditions existing in a fast sodium-cooled reactor, the results show that the maximum temperature rise under worst-case conditions is no more than some tens of degrees, while the increase in pressure at the wall of the fuel system is not more than 2.0 MPa, with a duration of a few milliseconds. Special experiments for studying these processes have not been carried out in the USSR. However, the calculation model has been shown by experimental and theoretical investigations to be very close to the phenomena arising in the space between the fuel elements as a result of interaction between the sodium and the water of the hydrogen bubble when it is ejected into the compensation space. The results are practically identical from the point of view of hydrodynamics [7]. These calculations show a close accord between calculated and experimental data.

Analysis shows that local blockage of the coolant paths inside the fuel subassembly and failure of the fuel cans do not lead to an avalanche spreading of the damage. The situation could continue for some time without any significant extension of the fault zone. An effective way of recording such a situation is to monitor the sealing of the can by reference to the gas activity and delayed neutrons. It is also possible to register this stage of a fault from the neutrons and the acoustic noise of the boiling sodium.

It is possible for the sodium to boil throughout the fuel subassembly when the flow rate falls by not more than half. This could arise through the blockage of a considerable part of the coolant path section and also through an increase in the hydraulic resistance, combined with a sealing failure in a large number of fuel elements. The spread of damage in this case can be determined from the nature of the boiling (stable or otherwise). Unstable boiling, accompanied by a rapid reduction in the flow rate of the coolant through the fuel subassembly, or pressure pulsing, accelerates the breakup of the fuel element. The hydraulic characteristics of the fuel subassembly determine the nature of the boiling. The location of the operating point on the drooping part of the hydraulic characteristic of the core is a sufficient condition for unstable boiling. In a normal fuel subassembly, the operating point lies at the minimum of the hydraulic characteristic and boiling at this point would be unstable. This is a property of all BN reactors. The hydraulic characteristic of a faulty fuel subassembly can be represented as the sum of the hydraulic characteristic of a normal fuel subassembly and some additional resistance, which can be either local or distributed throughout the length of the subassembly. Any additional resistance to the liquid part of the flow of sodium increases the stability of any possible boiling. Resistance to the two-phase part increases the instability of the process. Despite the low probability of sodium boiling in the subassembly, it is logical to suppose that it would start due to the appearance of additional resistance at the inlet to the subassembly, since the flow section of the core is reduced at this point, due to the buildup of oxides or the depositing of any foreign material from the coolant. This would occur predominantly at the inlet part in the vicinity of the gas chamber of the fuel element, since this is the "coldest" place in the primary
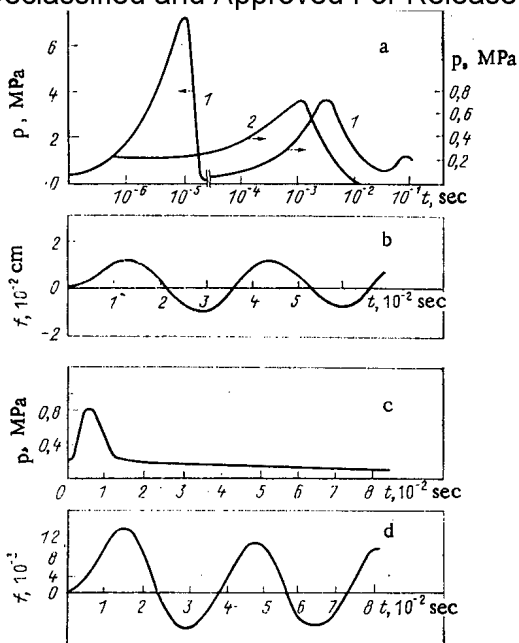
660

Fig. 1

Fig. 2

Fig. 1. Melting of one fuel element: 1) instantaneous contact of fuel and liquid sodium; 2) the same, but with boiling sodium; a, b) when there is no interaction of initial vapor and gas; c, d) with dispersion (fragmentation) time of fuel and its mixing with liquid sodium of 0.005 sec.
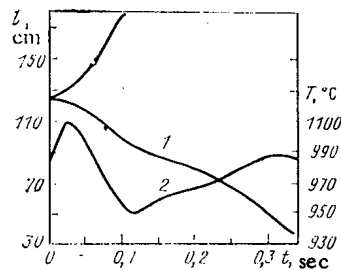
Fig. 2. Boiling of sodium in fuel subassembly: 1) position of boundary of bubble; 2) temperature of sodium in bubble; l) axial coordinate of fuel subassembly.

circuit. Calculations show that the operating point in this case can be found on the rising part of the hydraulic characteristic. However, the margin in flow stability is small and comprises a few percent of rated flow.

When considering a fault involving melting of the fuel in a subassembly of a fast reactor, we find it necessary to investigate all its stages. One of the phenomena important when assessing the consequences of such a fault is the thermal interaction between the fuel and the sodium. Investigation of this process is of interest from the point of view of whether or not the fault can spread from one subassembly to the next, due to the mechanical loads on the walls of the damaged subassembly. Models, methods, and a series of calculated results have already been obtained [8, 9]. We shall consider the process of interaction of the molten fuel with the sodium and the reaction of the walls of the can to the pressure pulses that arise. The calculated value of the pressure pulses depends upon many parameters characterizing the conditions governing the behavior of the process, the scale of the fault (the quantity of molten fuel), the time dispersion of the fuel and its mixture with the sodium, the presence of the vapor phase of sodium or gas in the zone of interaction and so on. Since the coefficient of conversion of thermal energy into mechanical energy is determined by the rate of heat transmission, we can consider melting of the fuel throughout the height of the subassembly to be negligible, since the fact that the process differs in the various sections throughout the height of the subassembly will reduce the maximum pressure in the subassembly (the duration of the effective interaction process does not exceed about 0.1 sec). Figure 1a, b gives the results of calculations of the pressure within the zone of interaction and displacement of the wall of the fuel subassembly when one fuel element melts over a length of 1 cm for various initial vapor contents in the zone of interaction. Curve 1 corresponds to the limiting case of instantaneous contact of the fuel with the liquid coolant under the worst conditions: when there is no initial vapor and gas in the zone of interaction. Under these circumstances, the maximum pressure is 7.5 MPa. However, the duration of the pulse does not exceed $0.5 \cdot 10^{-4}$ sec. When vapor is present, the maximum pressure is lower (curve 2). The calculated deflection of the subassembly wall shows that a short pulse at a pressure of 7.5 MPa causes considerably less deflection of the wall than would be the case with steady-state loading. Figure 1c, d gives the results of calculations for the most realistic assumptions, taking into consideration the dispersion and mixing times, but without a vapor phase, whose presence would lead to even-lower values, both of pressure and of wall deflection. We need to have regard for the nonsimultaneous nature of the dropping of the molten fuel into the sodium (the delay even over a section of 1 cm comprises several tens of milliseconds). Taking the presence of initial vapor and gas in the zone of interaction into account, together with condensation of the

661

vapor, we arrive at an even greater reduction in pressure and consequently to a smaller deflection of the subassembly wall.

An analysis shows that in all the cases we have been considering, no damage to the walls of the fuel subassembly takes place and therefore this factor cannot be the cause of a spreading of the damage to neighboring subassemblies. Such damage can be spread by a drying of the surfaces of fuel cells in the zone of interaction (the bubble) or a fall in the flow rate of sodium throughout the whole subassembly, due to an increase in the internal pressure. However, the damage is unable to spread in these cases due to the short-term nature of the process.

Calculations show that when the nonsimultaneity of melting of the fuel is correctly taken into account, together with the instant of its falling into the sodium, we are able to maintain the integrity of the wall, even when fuel elements melt over half the sectional area of the subassembly. However, a high level of indeterminacy is introduced into these calculations by the temperature of the wall and the properties of its material.

Calculating the effects of the interaction of the fuel with the sodium when the fuel elements melt over the whole section of the fuel subassembly gives us pulses of pressure enough to cause disruption of the walls of the subassembly, with all that this entails. However, a rapid melting of the fuel elements over the whole section can only be considered possible by postulating a fault with instantaneous blockage of the sodium flow throughout the whole subassembly.

The system for supplying coolant to the subassembly is arranged so that total blockage, and particularly instantaneous blockage, becomes impossible. Consequently, faults involving instantaneous blocking of the whole cross section can only be considered improbable. We only consider this case to determine the limiting time characteristic of the processes involved.

Figure 2 shows the results of calculations of the boiling process (boundaries of bubbles and temperature in bubble) with instantaneous reduction of sodium flow rate throughout the subassembly. Boiling of sodium starts after about 0.55 sec at the exit from the core. It then spreads into the depth of the subassembly and on to its inlet. The upper zone of destruction is achieved after about 0.08 sec, while full destruction takes place after 0.35 sec. Heat transfer from the surface of the fuel element at its "hot" points starts after 0.3–0.4 sec following boiling. When the film of sodium has dried over a sufficient length of the fuel part, the amount of heat entering the bubble will fall off, and a reverse flow of sodium will take place in the subassembly.

However, full heating of the subassembly does not in fact take place. The characteristic time of development of the damage up to this stage is about 1 sec. After heat transfer from the surface of the fuel element ceases, the temperature of the fuel element starts to rise and it eventually melts. Complete melting of the fuel in the endangered section takes 5–6 sec. The time needed for the melting to spread throughout the height of the core is 0.7–1.0 sec. After the fuel has melted, it falls onto the wall of the subassembly. The walls of the damaged and neighboring subassemblies behave in an ambiguous way. An assessment of the temperature of the subassembly walls for various assumptions shows that the walls of neighboring subassemblies may or may not melt. We are unable to give one single answer to the question as to how long the coolant section can avoid being destroyed in such a situation. However, the mechanical loading of the subassembly walls due to the interaction of the molten fuel with the sodium can cause the walls to fail as a result of the high temperatures reached, and they could quite possibly melt. We are unable to say what effect this would have on the neighboring subassemblies. Calculations taking account of the heat transfer from the molten fuel and from the walls of the fuel subassemblies adjacent to the damaged subassembly indicate that full melting of the walls of the faulted subassembly would take place in about 8 sec under worst-case conditions. The molten mass of fuel would then fall on the wall of the neighboring subassembly. The resulting mechanical loading would rapidly disrupt this wall also. Further spreading of the damage would take place relatively slowly, since the sodium would be circulating at its normal rate through the neighboring subassemblies and an adequate heat transfer would be taking place. However, the loading, disruption, and melting of part of the damaged subassembly can lead to very slow but progressive extension of the damage. The time characteristics of the fault at this stage depend upon a number of factors which are difficult to assess in practice. Therefore, as our characteristic time for the development and propagation of the fault from the damaged subassembly to the six neighboring subassemblies, for guarantee purposes, we can take the time interval from the onset of occlusion of the damaged subassembly to the melting of its own wall (about 15 sec, according to calculation). This is the decisive time for the speed of reaction of the monitoring and protection systems of the reactor covering this type of fault.

In reactors with U–Pu-charged sodium chambers, the effect of reactivity throughout the core is positive. The maximum reactivity effect during boiling of the sodium in the coolant section and its drying out comprises $0.74 \cdot 10^{-4}$ $\Delta k/k$. The maximum rate of introduction of reactivity is $3 \cdot 10^{-4}$ $\Delta k/k$ per second. From the point of

662

view of the safety of the reactor, such a reactivity is insignificant, but it is sufficient for observing such faults from anomalous changes in reactivity, measured with the aid of equipment based on calculation of reactivity balance [10]. The introduction of positive reactivity is possible later, during the melting and displacement of the fuel. Faults involving the melting of one fuel subassembly and the leakage of fuel into the lower zone involve a variation in reactivity of about $-5.4 \cdot 10^{-4}$ $\Delta k/k$. The maximum reactivity is achieved in the case of a collapse of the molten fuel in the center of the core and comprises $8.7 \cdot 10^{-4}$ $\Delta k/k$. This hypothesis involves an idealized way of looking at the movement of the molten fuel. The maximum reactivity for destruction of seven fuel subassemblies, melting of the fuel, and collapse in the center comprises about $0.4 \cdot 10^{-2}$ $\Delta k/k$. This value is close to the effective proportion of the delayed neutrons at the limit of accuracy of the calculations. However, the introduction of such reactivity will increase with time (the duration of the introduction is greater than the propagation time of the fault given above). If such a rate of introduction of reactivity is achieved, then the power level will increase at a rate of about 10% per sec.

As we have already seen, the construction of assembles through which the sodium is fed to the fuel subassemblies is such that it excludes any possibility of an object blocking the inlet. When considering the worst-case design fault, our hypothetical initial condition of instantaneous blocking of the flow through the fuel subassembly is chosen with the aim of determining the minimum time characteristics of the fault. In this regard (when choosing more-probable initial assumptions of the scale and time of the blockage of the section), the process will in reality be considerably more drawn out. The development of the fault is observed at the stages of fuel-element overheating and the failure of its seal by observing the delayed neutrons, which fix the limit and the rate of increase of activity. Then, if the reactor has not already been shut down, the boiling of the sodium and the melting of the fuel can be registered from the neutron-flux and acoustic noise and also by the system for monitoring the reactivity balance, which initiates an alarm signal.

LITERATURE CITED

1. "General requirements for ensuring the safety of nuclear power stations during design, construction, and operation," (OPB-82), At. Energ., 54, No. 2, 151-160 (1983).
2. G. P. Bogoslovskaya, A. V. Zhukov, N. M. Matyukhin, et al., Studying the Thermodynamic Characteristics of Fuel Element Assemblies with Partial Blockages [in Russian], Survey FÉI-OB-146 (1982).
3. K. Gast et al., "Local boiling in partially blocked LMFBR subassembly," in: International Conference on Engineering of Fast Reactors for Safe and Reliable Operation, Kernforschungszentrum, Karlsruhe, 9-13 Oct., 1972.
4. D. Smith et al., "DFR special experiments," in: Proc. International Symposium, Bologna, Italy, 10-14 April, 1978. IAEA-SM-224/49.
5. J. Van Erp et al., "Pin-to-pin failure propagation in liquid-metal-cooled fast breeder reactor fuel subassemblies," Nucl. Safety, 16, No. 3, 297-307 (1975).
6. C. Dickerman, "Studies of fast reactor core behavior under accidental conditions," Nucl. Safety, 11, No. 3, 195-205 (1970).
7. V. M. Poplavskii, Yu. E. Bagdasarov, and V. N. Leonchuk, "Calculated methods of assessing the state of the sodium circuit with significant disruption of the tubing in a 'sodium-water' steam generator," At. Energ., 30, No. 2, 191 (1971).
8. Yu. K. Buksha, Yu. E. Bagdasarov, and I. A. Kuznetsov, "Studying the interaction of molten fuel with sodium in the core of a fast reactor," At. Energ., 41, No. 1, 9-14 (1976).
9. Yu. E. Bagdasarov, L. M. Zabud'ko, Yu. K. Buksha, et al., Studying the behavior of the hexagonal cans of the fuel subassemblies of a TVS fast reactor under maximum design fault conditions," Preprint FÉI-1477 (1983).
10. B. V. Kebadze, V. N. Efimov, and L. A. Adamovskii, "Statistical errors in calculating reactivity balance," At. Energ., 43, No. 1, 36-37 (1977).

DETERMINATION OF THE TRANSFER CROSS SECTION
UNDER THE THRESHOLD OF ^{238}U FISSION, AS OBTAINED
FROM EXPERIMENTS ON THE TRANSMISSION OF FISSION
NEUTRONS

V. A. Dulin, V. V. Korobeinikov,   UDC 621.039.51
V. M. Lityaev, and A. M. Tsibulya

When systems of group constants for the calculation of reactors or shields are compiled and tested, data of integral experiments are usually employed. Experiments in which the transfer cross sections under the fission threshold of ^{238}U are investigated are of particular interest. The BNAB–78 system of constants [1] facilitates the calculation of fast reactor characteristics, such as k_{eff} and the recovery factor with errors of 1.4 and 2.4%, respectively. The uncertainty of the transfer cross sections under the ^{238}U fission threshold of the construction materials and of ^{238}U itself significantly contributes to the errors indicated above (0.8 and 1.2%, respectively).

The transfer cross sections under the ^{238}U fission threshold were studied in experiments on the spherical transmission as early as in the fifties in the Soviet Union by Bondarenko [2], Lovchikova [3], and Andreev [4] and abroad by Bethe, Bayster, and Carter [5]. The results of those experiments were used when the BNAB–64 system of group constants was compiled [6]. For example, the transmission through 10 spherical shells with a transmission ranging from 0.47 to 0.96 was studied in the case of iron [5]. An inverse geometry was used in the experiments, i.e., the threshold detector was placed inside the sphere and the neutron source was far away outside. A thin ^{235}U plate irradiated with thermal neutrons was used as the neutron source with a fission spectrum. The errors in the transfer cross sections of the main reactor materials amounted in these experiments to 5-20%. In particular, the errors of the cross sections of inelastic scattering amounted to 20% in the case of stainless steel and ^{238}U. Nikolaev noted in his WRENDA list of requirements in nuclear data [7] that the precision of the transfer cross sections can be increased by repeating experiments with spherical transmission under optimal conditions and by analyzing these experiments with all the care which can be reached in modern computational techniques. This problem is the subject of the present paper.

The experiment was made in a straight spherical geometry (see Fig. 1), i.e., the neutron source was inside the sphere under inspection. A tube with the ^{252}Cf nuclide undergoing spontaneous fission was used as the source. The spheres under inspection usually had the same external diameter of 170 mm. Three fission chambers with ^{238}U layers were placed close to the spheres. Each of the chambers had the shape of a sphere and covered an angle of about 0.6π. The angles between the chamber centers were 120° and the total solid angle covered by all the chambers was close to 2π.

The proposed quasispherical geometry of the detector made it possible to obtain a high signal–to–noise ratio in the neutrons reflected from the walls and a high recording efficiency with a relatively thin uranium layer (1 mg/cm^2), which helped to obtain good counting characteristics of the chamber and therefore a high reproducibility of the results; in this way it was also possible to obtain a spherical experimental model suitable for an analysis by calculation.

This latter detail compensated for shortcomings of the detector geometry selected in comparison with the clasical detector geometry in which the detector is far from the sphere so that the various angular distributions of the neutrons incident on the detector directly from the source or after one or several collisions inside the sphere can be disregarded. In the classical formulation of the problem, the spherical transmission for a purely scattering but not moderating sphere is equal to unity. In our formulation of the problem, the angular distributions of the scattered and unscattered neutrons incident on the detector are obviously different, and since a detector with a spherical layer is characterized by an angular dependence of its sensitivity, the ratio of the counting rate with the sphere to the counting rate without the sphere is greater than one even for a purely scattering, not moderating sphere. In this way, the cross section of the transfer must in our case be assessed from

---

TABLE 1. Compositions of the Zones (number of nuclei in a volume of 10^{-20} cm^3)

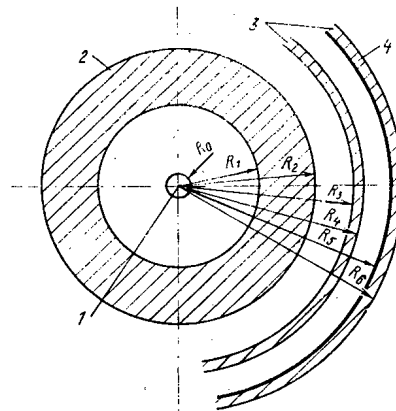| Nuclide	Zone of the source	Chamber wall	Material of the sphere			
			iron	steel	nickel	uranium
C	4,76	4,76	7,16	4,76	—	—
Cr	165	165	—	165	—	—
Ni	84,1	84,1	—	84,1	875	—
Si	13,6	13,6	—	13,6	—	—
Mn	1,30	1,30	4,30	1,30	—	—
Fe	584	584	847	584	—	—
Ti	6,96	6,96	—	6,96	—	—
^{238}U	—	—	—	—	—	473
^{235}U	—	—	—	—	—	0,33

Fig. 1. Computational model of the experiment:
1) source; 2) spherical sample; 3) wall of the fission chamber; 4) ^{238}U layer; $R_0 = 0.31$ cm is the effective radius of the source; R_1 denotes the inner radius of the sphere under consideration and is for iron spheres 7.5, 5.5, 3.6, 1.5, and 1.5* cm, and for nickel and 1Kh18N10T spheres 5.5, 3.6, and 1.5 cm; $R_2 = 8.50$ cm denotes the outer radius of the sphere under consideration and $R_1 = 1.5$* and $R_2 = 2.5$ cm in the case of the steel sphere; $R_3 = 8.60$ cm and $R_4 = 8.65$ cm denote the inner and outer radius of the inner wall; $R_5 = 9.00$ cm and $R_6 = 9.05$ cm denote the inner and the outer radius of the outer wall.

the values corresponding to a sphere with transfer cross section zero rather than one, in contrast to the measured transmission. The value can be rather accurately calculated because the geometry of the experiment is very simple.

Experiments were made with metal spheres of iron, nickel, 1Kh18N10T steel, and uranium (see Table 1).

The results of the experiments are listed in Table 2 together with the results of preliminary calculations made with the Monte Carlo method in the multigroup transport approximation using the BNAB-78 system of constants [1]. The possible use of the multigroup transport approximation for the calculations had been analyzed.

It was unclear how the results of the calculations are affected by the spatial dependence of the resonance self-shielding of the cross sections. The influence of this effect is at its maximum in iron spheres. A comparison of the transmission through the steel sphere with $R_1 = 1.5$ cm ($\Delta R = 7$ cm) calculated in the subgroup approximation (i.e., taking into account the spatial dependence of the resonance self-shielding) and in the group approximation (in which resonance self-shielding was assumed as similar to that of an extended iron medium) has shown that the effect cannot be distinguished within the statistical error limits of the computational results:

665

TABLE 2. Comparison of the Calculated and Experimental Transmissions*

Sphere	T_{exp}	T_{calc}	δT_{calc}	T^∞_{exp}	T^∞_{calc}	$\dfrac{T^\infty_{calc} - T^\infty_{exp}}{T^\infty_{exp}} \cdot 100$
Fe1	0,991±0,002	0,988±0,002	0,052±0,003	0,939±0,003	0,936±0,002	−4±6
Fe2	0,874±0,003	0,878±0,002	0,074±0,002	0,800±0,003	0,803±0,002	2±2
Fe3	0,758±0,002	0,762±0,002	0,073±0,002	0,684±0,003	0,688±0,002	1±1
Fe4	0,648±0,001	0,655±0,002	0,065±0,002	0,583±0,002	0,589±0,002	2±1
Fe5	0,938±0,002	0,944±0,006	0,005±0,007	0,933±0,007	0,939±0,004	9±13
Steel 1	0,876±0,002	0,875±0,003	0,085±0,003	0,791±0,003	0,791±0,002	0±2
Steel 2	0,751±0,002	0,753±0,003	0,0798±0,002	0,671±0,003	0,673±0,002	1±1
Steel 3	0,645±0,002	0,634±0,005	0,068±0,005	0,577±0,006	0,567±0,004	−2±2
Ni1	0,856±0,002	0,839±0,002	0,071±0,002	0,785±0,003	0,769±0,002	−8±2
Ni2	0,732±0,002	0,714±0,003	0,071±0,003	0,661±0,003	0,645±0,002	−5±1
Ni3	0,626±0,001	0,602±0,002	0,063±0,002	0,563±0,003	0,541±0,002	−5±1

*The results are given in the order of the R_1 values in the legend to Fig. 1.

TABLE 3. Comparison of the Transfer Cross
Sections Under the Threshold of ^{238}U Fission

Material of the sphere	Experiment	BNAB -78	Work of[5]
Iron	0,67±0,02	0,66	0,69
Nickel	0,78±0,02	0,83	0,71
^{238}U	2,16±0,04	2,11	—
Steel	0,64±0,02	0,63	—

in the subgroup approximation, the transmission was 0.657 ± 0.002, whereas the transmission was 0.655 ± 0.002 in the group approximation. The uncertainty in the fission spectrum of ^{252}Cf proved to be irrelevant.

Further, it was shown that it is possible to use the transport approximation of the scattering pattern. The transmission T for an iron sphere with the layer thickness $\Delta R = 4.9$ cm was calculated in the group approximation taking precisely into account the anisotropy of scattering. The result $T = 0.759 ± 0.004$ coincided within the statistical error limits with the results of a calculation made in the transport approximation: $T = 0.762 ± 0.002$. An analysis of the calculated results has confirmed that the multigroup transport approximation can be used for evaluating experimental data on the spherical transmission under real geometrical conditions.

Two quantities were determined in the calculation: the transmission $T_i(\Delta R)$, determined with the aid of a spherical detector surrounding the sphere, where ΔR denotes the thickness of the spherical layer of the i-th material, and the transmission $T_i^\infty(\Delta R)$ for infinite distance of the fission chamber from the sphere. The difference $\delta T_i(\Delta R) = T_i(\Delta R) - T_i^\infty(\Delta R)$ is termed the geometrical correction. In the experiments, the cross section of neutron transfer under the ^{238}U fission threshold can be defined as

$$\sigma^y_{yi} = \lim_{\Delta R \to 0} \frac{1 - T_i^\infty(\Delta R)}{C_i \Delta R},$$

(1)

where C_i denotes the concentration of the nuclei in spheres prepared from the i-th nuclide. For $\Delta R \to 0$, we have $T_i^\infty(\Delta R) = e^{-C_i \bar{l}\sigma_{yi}} \to 1 - C_i \bar{l}\sigma_{yi}$, where $\bar{l} \to \Delta R$; Eq. (1) therefore is obtained.

It follows from the multigroup system of constants that

$$\sigma^k_{yi} = \frac{\sum\limits_g \varphi_g \sigma^g_{fU} \sigma^g_{yi}}{\sum\limits_g \varphi_g \sigma_{fU}},$$

(2)

where φ_g denotes the spectrum of the source neutrons; and σ^g_{fU} denotes the cross section of ^{238}U fission to which the detector efficiency is proportional; further

$$\sigma^g_{yi} = \sigma^g_{ci} + \sigma^g_{fi} \sum_{g' > g} \sigma^{g \to g'}_{si} \left(1 - \frac{\sigma^{g'}_{fU}}{\sigma^g_{fU}}\right) + \sum_{g' > g} \sigma^{g \to g'}_{2ni} \left(1 - 2\frac{\sigma^{g'}_{fU}}{\sigma^g_{fU}}\right).$$

(3)

666

The T_{exp}^{∞} values for the first and the fifth iron sphere with identical layer thicknesses but with different external diameters coincide within the experimental error limits, whereas the transmission values measured with a real detector differ considerably. This confirms that corrections should be introduced for the angular dependence of the detector sensitivity.

It follows from a comparison of experimental and calculated results that for all spheres, except for the nickel spheres, the experimental and calculated transmission values coincide within the error limits of the experiment and the calculations. Thus, our experiments confirm the transfer cross sections of iron, stainless steel, and ^{238}U, with the cross section figures obtained with the BNAB-78 group constants assumed in the calculations.

In the case of nickel spheres, a systematic difference exists between the calculated and experimental transmission values. The difference indicates that the BNAB-78 constants render excessively high transfer cross sections under the threshold of ^{238}U fission (see Table 3).

Let us make the following remarks in conclusion.

Our experiments provide interesting information on the transfer cross sections of neutrons under the ^{238}U fission threshold; when these results are taken into account in the determinations of neutron data, the error of the transfer cross section can obviously be reduced to 3%, and this satisfies the accuracy requirements of integral moderation and absorption characteristics to be assessed for fast neutrons.

This approach is possible mainly when a very careful computational analysis is performed. The errors of the calculations due to errors of the total cross sections, the scattering cross sections, the anisotropy of scattering, etc., and the errors associated with the group approximation must be quantitatively assessed. The transfer cross section must also be carefully determined on the basis of available experimental data. It is unlikely that the results of a more careful analysis will substantially deviate from the results stated herein. However, as long as this analysis has not been made, the determination of the transfer cross section will not be fully reliable. Therefore, the results of the computational analysis listed above should be considered preliminary results.

The use of the results in practice must be supplemented by a review of weighted neutron data (including information on their errors), and accordingly, these data must correspond, within the error limits, to the results of the differential neutron-physical integral experiments (in particular, to the experiments described in the present article), as well as to the results of macroscopic experiments made on critical assemblies which contain in large concentrations the materials under consideration [8-10]. Work along this line is in progress.

In conclusion, the authors thank M. N. Nikolaev, who was of great help in planning the present experiments and in interpreting the results obtained.

LITERATURE CITED

1. L. P. Abagyan, N. O. Bazazyants, M. N. Nikolaev, and A. M. Tsibulya, Group Constants for the Calculation of Reactors and Shields [in Russian], Énergoizdat, Moscow (1981).
2. I. I. Bondarenko, in: Proc. of Seminar on Physics of Fast and Intermediate Reactors, Vol. 2, IAEA, Vienna (1962), p. 159.
3. G. N. Lovchikova and O. A. Sal'nikov, "Cross sections of the inelastic interaction of the neutrons of the fission spectrum," At. Energ., 11, 442 (1961).
4. V. N. Andreev, Inelastic Scattering of Neutrons of the Fission Spectrum and of 0.9-MeV Neutrons in ^{235}U and ^{239}Pu. Neutron Physics [in Russian], Atomizdat, Moscow (1961), pp. 287-293.
5. H. A. Bethe, et al., Nucl. Energy, 3, 273 (1956); Nucl. Energy, 4, 3 (1957); Nucl. Energy, 4, 147 (1957).
6. L. P. Abagyan, N. O. Bazazyants, I. I. Bondarenko, and M. N. Nikolaev, The Group Constants for Calculating Nuclear Reactors [in Russian], Atomizdat, Moscow (1964).
7. WRENDA-79/80, World Request List for Nuclear Data-INDC (SEC) 73/VRSF, October (1979).
8. J. Chaudat, M. Darouzet, and E. Fisher, Experiment in Pure Uranium Lattices with Unit K_{∞}, KFK-1865 (CEA-R-4552) (1974).
9. V. I. Golubev, S. I. Isachen, Yu. A. Kazanskii, et al., Investigation of the Characteristics of a Fertile Medium of ^{235}U and Stainless Steel, Problems of Atomic Science and Technology, Nuclear Constants Series [in Russian], No. 1 (28), pp. 41-45 (1978).
10. P. Azzoni, G. Brighenti, and F. Casali, Energ. Nucl., 24, 411 (1977).

STRUCTURAL CHANGES IN THE Kh20N45M4B NICKEL ALLOYS AND THE Kh16N15M3B STEEL DUE TO HELIUM ION BOMBARDMENT

B. A. Kalin, I. I. Chernov,
V. L. Yakushin, G. N. Shishkin, V. N. Chernikov,
O. A. Kozhevnikov, and A. N. Lapin

UDC 621.039.531

The structural materials of the discharge chambers of the thermonuclear systems and reactors are subjected to bombardment by large fluxes of accelerated light ions. This leads to radiation damages [1-6], and changes in the chemical composition [6-8] and, possibly, in the phase constitution [9] of the layers near the surface which, as was shown earlier [6, 10], have a significant effect on the fracture and erosion of the surface layer during He$^+$ bombardment. Therefore, a study of the structural damages, phase constitution, and chemical composition of the surface layers of the bombarded specimens is of great interest for evaluating the degree of damage of the materials during ion-bombardment and the interstitial gas accumulation in them.

Using transmission electron microscopy, x-ray structural analysis, and the thermal desorption techniques, we carried out a detailed study of the structural and phase changes, defect formation, and helium accumulation in the He$^+$-bombarded 16-15 austenitic steels and 20-45 nickel alloys (Table 1).

Experimental specimens were cut out from 0.2-0.5-mm-thick sheets of the industrial materials. Prior to ion-bombardment, the specimens were subjected to mechanical and electrolytic polishing, and were subsequently annealed in pure argon atmosphere at 1170°K for a period of 1 h. Bombardment of the specimens with He ions having an energy of 40 keV up to a fluence of $(1-600) 10^{20}$ m^{-2} was carried out in the 300-870°K range in an ILU-3 ion accelerator; bombardment with the ions having an energy of 20 keV up to a fluence of $(1-5) 10^{21}$ m^{-2} was conducted at temperatures up to 370°K in a double-focusing mass-monochromator [6]. All the structural studies were carried out on the specimens bombarded at T $\lesssim$ 370-420°K. The changes in the chemical composition of the near-surface layers were studied after bombardment at 300-870°K.

Microstructure of the bombarded specimens was studied using the methods of transmission electron microscopy of thin foils in the ÉVM-100L and EM-301G electron microscopes. The specimens for electron microscopic analysis were cut out from the bombarded materials on an electrospark machine, and were thinned on a special apparatus designed for continuous one-sided removal of metals. Electron micrographs and the microdiffraction data were processed according to the standard procedures [11-13]. X-ray studies on the specimens were carried out on a DRON-UM1 diffractometer using Cu K$_\alpha$ radiation. Thermal desorption of helium from the bombarded materials was studied under linear heating conditions maintaining a heating rate of 0.5 °K/sec in a mass spectrometer designed for investigating the processes of accumulation and liberation of inert gases. The changes in the chemical composition of the surface layers of the materials were followed using the secondary ion mass spectrometry (on a SMI-300 analyzer) and the Auger electron spectroscopy methods. The distribution of elements along the depth was studied during the process of layer-by-layer sputtering of the surface layer (at a rate of 0.25-0.3 nm/sec) with Ar$^+$ ions having an energy of 2-10 keV based on the analysis of mass-spectra of the positive ions of the specimen or the sputtered material.

TABLE 1. Chemical Composition of the Experimental Materials

Material	Weight content of elements, %									
	Cr	Ni	Mo	Nb	Ti	Al	C	N$_2$	B	Others
Steel 16-15	16,2	14,8	2,9	0,56	—	—	0,07	0,25	—	—
Steel 16-15 R	15,8	15,0	2,8	0,78	—	—	0,08	0,04	0,008	0,07 (Cu) 0,05 (Y)
Alloy 20-45	19,6	45,5	4,0	0,84	0,08	0,10	0,016	—	—	
Alloy 20-45 '	19,4	44,9	3,6	0,89	0,02	0,16	0,022	0,008	0,005	0,04 (Cu) 0,035 (Zz)

668   0038-531X/85/5902-0668$09.50   © 1986 Plenum Publishing Corporation

TABLE 2. Dependence of the Volumetric Density of the Loops ρ_{lps} and the Bubbles ρ_{bls}, and the Bubble Size ($2 r_b$) in the Materials Bombarded with He^+ ($E = 40$ keV, $T \leqslant 370°K$) on the He^+ Fluence

Material		Fluence, 10^{21} m^{-2}	ρ_{lps}, 10^{21} m^{-3}	ρ_{bls}, 10^{24} m^{-3}	$2r_b$, nm	$2\bar{r}_b$, nm
Steel	16-15	0,1	1,2±0,6	—	—	—
		0,3	2,2±1,1	—	—	—
		0,5	2,4±1,2	2	—	—
		1	2,0±1,0	7,1±2,1	1—5	2,0
Alloy	20-45	0,1	3,1±1,6	—	—	—
		0,3	3,5±1,8	—	—	—
		0,5	4,2±2,1	—	—	—
		0,7	4,0±2,0	6,0±1,8	1—4	2,0
		1	3,7±1,9	6,6±2,0	1—4	2,0
		3	—	8,4±2,5	1—3	1,8
		5 *				
		10	—	11,1±3,3	1—3	1,8

* In the fluence range (5-10) 10^{21} m^{-2} the bubbles form a superlattice with a period d ≈ 4 nm.
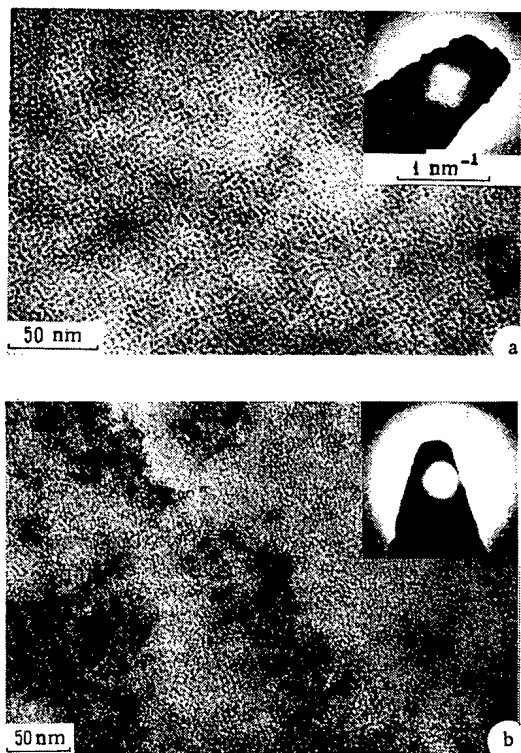
Fig. 1

Fig. 2

Fig. 1. Helium bubbles in the 20-45 nickel alloy bombarded with He^+ ($E = 40$ keV, fluence $1 \cdot 10^{22}$ m^{-2}, $T \leqslant 370°K$): a) region of ordered dispositioning of bubbles (overfocusing); b) region of disordered dispositioning of bubbles (underfocusing).
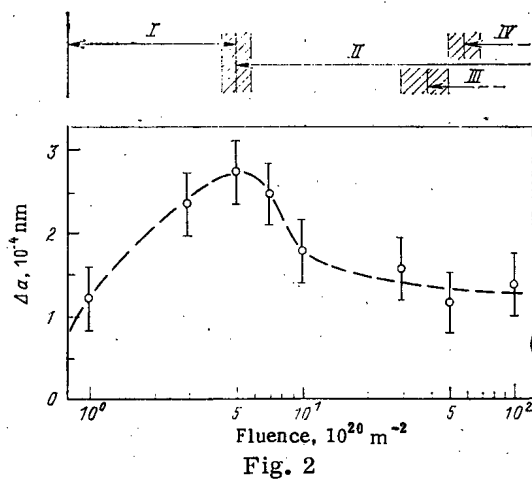
Fig. 2. Variation of the lattice constant of austenite in the 20-45 alloy bombarded with He^+ ($E = 40$ keV, $T \leqslant 370°K$).

669

Electron-microscopic investigation of the thin foils of the specimens bombarded with He^+ ions of energy 40 keV showed that at a fluence of $1 \cdot 10^{20}$ m^{-2} a defect structure consisting of point defect clusters and dislocation loops develops in the surface layers of the experimental materials. On increasing the fluence up to $5 \cdot 10^{20}$ m^{-2}, the dislocation loop size is insignificantly affected, but their volumetric density increases. An analysis of the fairly large loops in the 20-45 alloy showed that they are loops of interstitial atoms with a Burgers vector $b = (1/2) \, a \, \langle 110 \rangle$ lying in the close packed planes $\{111\}$. The calculations showed that the number of the point defects accumulated in these loops per unit volume amounts to $\sim 10^{23}$-10^{24} m^{-3}. In the stainless steels 316 and 0Kh16N15M3B, the nickel alloy Kh20N40M5B, and nickel, small dislocation loops form at a low He^+ fluence, and their density increases with increasing fluence [14, 15]. At an ion fluence exceeding $5 \cdot 10^{20}$ m^{-2} (Table 2), the loop density has a tendency to decrease, apparently because of their coalescence, and there is a slight increase in the average loop size. At a low fluence up to $1 \cdot 10^{21}$ m^{-2}, the volumetric densities of the dislocation loops considerably differ in the 20-45 type nickel alloys and the 16-15 type stainless steels: at a fluence of $1 \cdot 10^{20}$ m^{-2}, their ratio amounts to ~ 2.5, and with increasing fluence it decreases significantly. The fact that the 0Kh16N15M3B steel (that contains a greater amount of alloying elements as compared to the 1Kh18N10T steel) exhibits higher dislocation loop density was noticed during neutron irradiation also. In this case, the loop density varied from $\sim 3 \cdot 10^{20}$ m^{-3} and $\sim 10^{20}$ m^{-3} in the 0Kh16N15M3B and 1Kh18N10T steels, respectively, up to $\sim 7 \cdot 10^{20}$ m^{-3} in both cases as the fluence is increased from 2 up to 10 displacements per atom [16]; i.e., at a high fluence, the dislocation loop concentrations are less sensitive to the composition of the irradiated materials. The relatively large fraction of the radiation-induced vacancies captured by the alloying elements appears to be one of the possible reasons for the observed high density of the clusters of interstitial atoms in complex alloys and high-alloy steels.

At and above an ionic fluence of $7 \cdot 10^{20}$ m^{-2}, a high volumetric density of helium bubbles appears in the structure of the bombarded materials. With increasing fluence of the interstitial ions, the concentration of bubbles increases, but the average size remains virtually unaltered (see Table 2). We note that while at a fluence up to $1 \cdot 10^{21}$ m^{-2} one observes a considerable scatter in the bubble size distribution (1-4 nm) and the formation of separate bubbles measuring up to 5 nm in diameter, at a high fluence ($> 3 \cdot 10^{21}$ m^{-2}) the size distribution of bubbles shows less scatter and their average diameter is 1.8 nm in that the density and the sizes of the bubbles in the 16-15 steel and the 20-45 nickel alloy are virtually identical. As was shown earlier [5], at a fluence greater than $3 \cdot 10^{21}$ m^{-2} the bubbles form a space lattice both in complex alloys and pure metals [3, 4]. The bubble density reaches its maximum in the sublattice, and amounts to $\sim 10^{25}$ m^{-3}. The ordered assembly of the bubbles is retained right up to the development of blisters on the surface, i.e., up to a fluence of $\sim 10^{22}$ m^{-2}, but in this case, staggered zones with a much lower degree of ordering are observed (Fig. 1). This indicates that at a high fluence the bubble-lattice loses stability and collapses. Interaction of the neighboring bubbles is a possible mechanism of the disintegration of the superlattice. As was shown by Johnson and Mazey [17], this leads to the formation of blister cavities at a depth corresponding to the thickness of the blister covers.

Figure 2 shows the results of x-ray studies on the bombarded specimens. An analysis of the diffractograms revealed a marked dependence of the lattice constant of austenite a (determined from the position of the (422) and (400) diffraction lines) on the ionic fluence. With increasing fluence, initially there is a continuous increase in the lattice constant up to a fluence of $5 \cdot 10^{20}$ m^{-2} (Fig. 2, region I); with subsequent increase in fluence ($> 5 \cdot 10^{20}$ m^{-2}) we observe its decrease and gradual transition to a steady value (region II). In this case, there is a slight difference in the values of the lattice constant calculated from two different lines. This indicates the development of tetragonality in the lattice or a phase transformation involving a structural change (for example, fcc $\rightarrow$ hcp in nickel) [15, 18, 19]. The obtained results of electron microscopic and x-ray structural analysis of the bombarded materials generally agree with those published earlier [15].

A comparison of the dependence of a on the fluence (see Fig. 2) with the electron microscopy data on the substructure (see Table 2) and with the thermal desorption data shows that the region I of continuous increase of a coincides with the interval of helium accumulation and radiation-induced defects (fluence $< 5 \cdot 10^{20}$ m^{-2}). At a high fluence, the decrease in a is, apparently, due to partial elastic-stress relaxation resulting from the decay of the solid solution of helium in the material with the formation of gas bubbles. The regions III and IV, where the lattice constant of austenite retains a constant value, correspond to the formation of the superlattice of gas bubbles in the structure of the material and surface blisters. The relaxation of the lattice constant with increasing fluence of the implanted helium indicates that its increase is due mainly to the presence of helium atoms at the interstitial sites and in the $He_m V_n$ type ($m > n$) complexes [15, 19].

The form of the thermal desorption spectra of helium depends to a significant extent on the ionic fluence (Fig. 3, Table 3). On increasing the He^+ fluence from $1 \cdot 10^{20}$ m^{-2} up to $1 \cdot 10^{22}$ m^{-2}, there is an increase in the number of peaks appearing on the thermal desorption spectra (from one up to seven) and their height; the new

670

TABLE 3. Temperature of Peak Appearance on the Spectra of Thermal Desorption of Helium from the Materials Bombarded with He^+ (E = 40 keV, T ≤ 420°K)

Material	Fluence, 10^{21} m^{-2}	Peak number						
		I	II	III	IV	V	VI	VII
Steel 16-15	4	1600	1370	1310	1180, 1130 (splitting)	1050	850	
Steel 16-15P	8	1600	1445	1360	1130	1025	860	670
Alloy 20-45	10	1670	1530	1320	1170	1070	900, 850, 775 (splitting)	

Note: The peak numbers correspond to the symbols of Fig. 3.
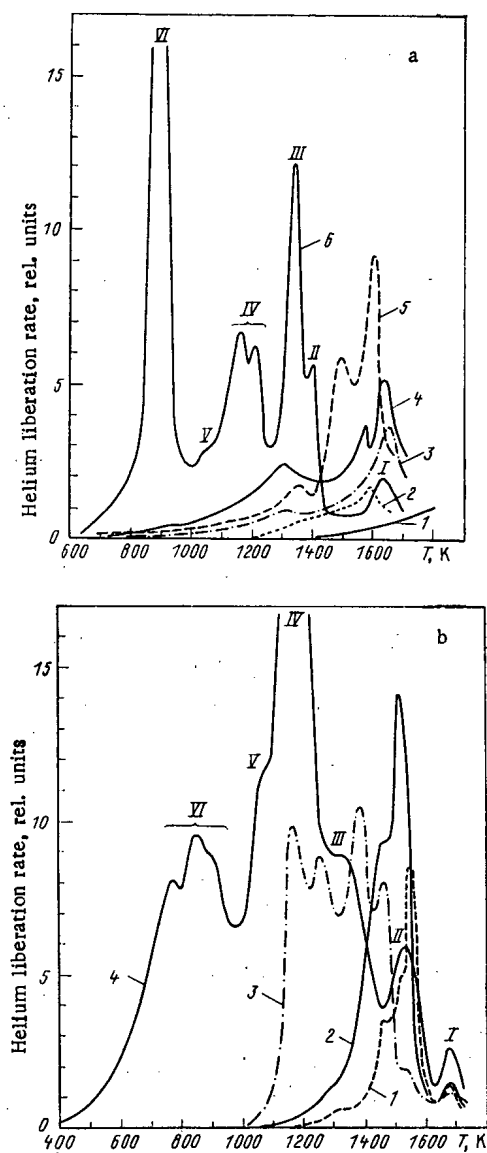
Fig. 3
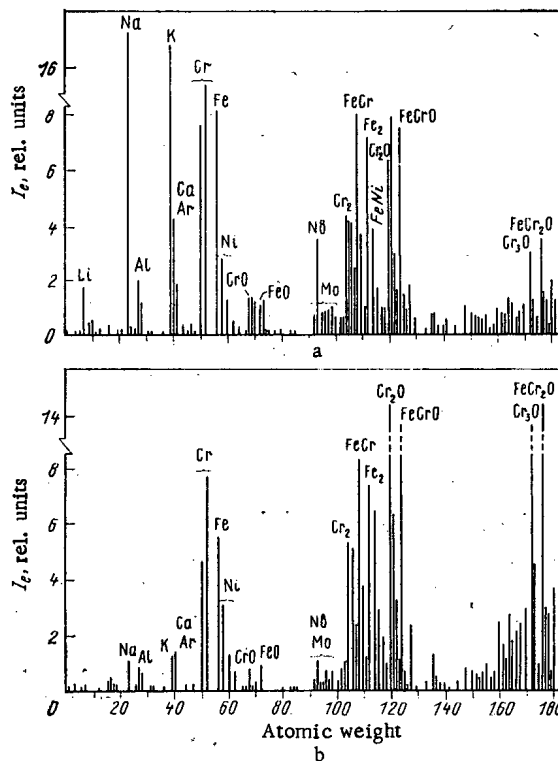
Fig. 4

Fig. 3. Spectra of thermal desorption of helium from the materials bombarded with He^+ (E = 40 keV, T ≤ 370°K); a) steel 16-15R: 1) background; 2) unexposed specimen; 3-6) specimens bombarded up to a fluence of $3 \cdot 10^{20}$, $7 \cdot 10^{20}$, $1 \cdot 10^{21}$, and $4 \cdot 10^{21}$ m^{-2}, respectively; b) alloy 20-45: 1-4) specimens bombarded up to a fluence of $5 \cdot 10^{20}$, $1 \cdot 10^{21}$, $2 \cdot 10^{21}$, and $1 \cdot 10^{22}$ m^{-2}, respectively.

Fig. 4. Mass spectra of the 16-15 steel specimens: a) original condition; b) after bombardment with He^+ (E = 20 keV, fluence $2 \cdot 10^{21}$ m^{-2}, T ≤ 370°K).

671

peaks appear at progressively lower temperatures in that with increasing fluence, the high-temperature peaks are shifted towards the low temperature region (see Fig. 3). An analysis of the gas liberation spectra shows that at a high fluence ($\geqslant 4 \cdot 10^{21}$ m^{-2}) the steels and the nickel alloy possess the same number of peaks. Here, the temperatures corresponding to the peaks I and II of the nickel alloy (see Fig. 3 and Table 3) are found to be higher than the temperatures of these peaks of the steels, but in the case of other peaks the temperature difference is insignificant. Hence, it may be concluded that when bombarded under identical conditions, the same mechanisms of helium expulsion operate during the heating process of both these austenitic materials. The obtained regularities of gas liberation from the He$^+$ bombarded specimens generally agree with the data of analogous investigations [1, 20]. At a fluence of $\leq 5 \cdot 10^{20}$ m^{-2} helium liberation takes place by one mechanism only: during the melting process of the specimens (peak I). From the moment helium bubbles appear in the structure of the materials (fluence $\geq 7 \cdot 10^{20}$ m^{-2}), certain new low-temperature peaks are seen in the thermal desorption spectra. This indicates operation of new mechanisms of helium liberation. The most complex desorption spectrum corresponds to the preblistering and blistering stages of structure evolution in the materials (fluence $\geq 4 \cdot 10^{21}$ m^{-2}). The presence of the low-temperature desorption peak VII (see Table 3) having an activation energy of ~ 1.5 eV (calculated according to a previously suggested method [21]) is, apparently, related to helium migration in the form of dumbbell-like complexes, for example, He$-$I, He$-$C, He$-$CV, etc., where I represents an intrinsic interstitial atom, C is a carbon atom (or any other interstitial element), and V is a vacancy. The possibility of formation and migration of such complexes is indicated by an analysis of the published data [22-24] and an experimental study on the redistribution of the main components of the austenitic materials (Fe, Cr, Ni) and the interstitial impurities (C, B, N, O) during the implantation process. In fact, the study of chemical composition of the ion-bombarded materials showed that at a high fluence there occurs a redistribution of the alloying elements along the depth of the specimens. This is confirmed by the layer-by-layer Auger analysis and a study of the specimens by secondary ion mass spectrometry (Fig. 4). The mass spectra of the 20-45 nickel alloys are similar to those of the 16-15 steel, but in the case of the 20-45 alloys all the mass peaks are substantially lower. An analysis of the obtained spectra shows that bombardment with He$^+$ of a relatively small fluence (below $1 \cdot 10^{22}$ m^{-2}) up to a temperature of 870°K does not lead to noticeable changes in the ratio of the main elements (Fe, Cr, Ni) in the experimental materials. This is seen from a comparison of the mass spectra presented in Fig. 4a and b. We find only a significant increase in the line intensity of the oxides and simultaneous surface decontamination from the impurities such as Li, Na, K, etc. Increasing the ionic fluence up to $6 \cdot 10^{22}$ m^{-2} leads to a redistribution of the main components of the steels along the depth of the target: in the layer measuring up to $\sim 0.4 \mu$m in thickness, the Fe and Cr content decreases by almost 2 times and a slight enrichment with nickel is observed.

According to the data of the earlier studies [6, 8], redistribution of interstitial impurities (C, B, O etc.) is observed even at a relatively low fluence (up to $2 \cdot 10^{21}$ m^{-2}), and segregation of boron and carbon takes place in the thin layer near the surface measuring < 10-15 nm in thickness, due to the reduced content of these elements in the ~ 0.1-μm-thick layer. At the same time, one observes enrichment of the surface layer with oxygen which penetrates up to a considerable depth (up to $\sim 1 \mu$m) and forms complex compounds with iron and chromium, as confirmed by the mass spectra of the bombarded specimens (see Fig. 4b).

Electron-microscopic study of the thin foils of the bombarded 16-15 steel specimens did not reveal noticeable changes in the phase composition of the materials due to bombardment. However, in the complex high-nickel 20-45 alloy bombarded with He$^+$ of energy 40 keV up to a fluence of $1 \cdot 10^{22}$ m^{-2} we observed numerous dark spots of different shapes that do not have clearly defined boundaries. Their maximum size amounts to $\sim 0.5 \mu$m. In some cases, the coarsest ones among them are decorated with minute phase-precipitates (< 0.01 μm) (Fig. 5). An analysis of their microdiffraction patterns showed that the observed particles have a fcc lattice and, in particular, the microdiffraction pattern shown in Fig. 5c matches well with the standard electron diffraction pattern of the fcc crystals having [011] orientation. According to our evaluation, the lattice constant of the precipitates lies within the limits 0.5664-0.5719 nm. It may be assumed that the observed precipitates are either particles of an intermediate phase in the segregation zone of atoms, which appear as blurred (diffused) spots on the electron microscopic image, or nuclei of secondary precipitates, for example, nickel niobide Ni(Mo, Nb)$_2$, that have a M$_6$C-type fcc lattice. Disintegration of the 20-45 nickel alloys must lead to the formation of such intermetallic compounds [25, 26].

It was previously observed [9] that in nickel and the 316 steel there are phase transformations caused by bombardment with P$^+$ having an energy of 40 keV up to a fluence of 10^{20}-10^{21} m^{-2} (flux density of ions $2 \cdot 10^{17}$ m$^{-2} \cdot$ sec^{-1}) at room temperature; here, it was concluded that the transformations are related not to the chemical nature of the interstitial ion, but to the high stresses (10^3-10^4 MPa) in the surface layers of the metal which result from the significant interstitial-ion concentration (atom fraction 25-30%). Apparently, the high internal
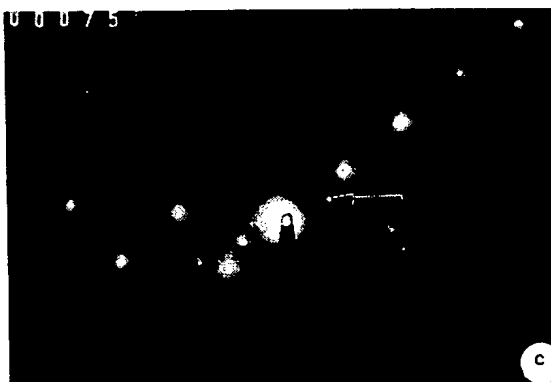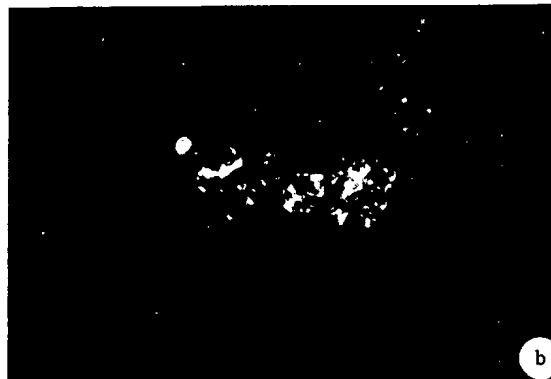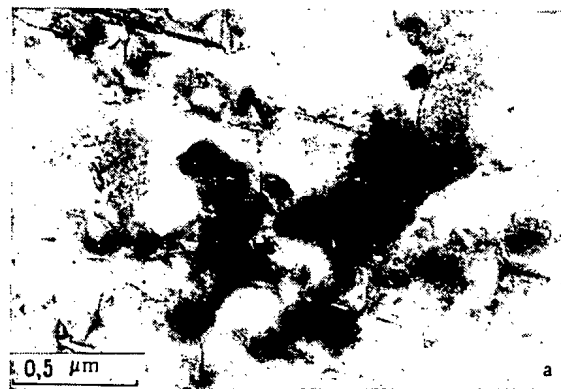
Fig. 5. Particles of the nuclei of the new phase in the He^+ bombarded 20-45 nickel alloy (E =40 keV, fluence $1 \cdot 10^{22} m^{-2}$, $T \lesssim 420°K$): a) bright-field image; b) dark-field image in reflected light, indicated by an arrow in the microdiffraction pattern (c); c) microdiffraction pattern of the selected region.

stresses developing in the surface layers during bombardment with barely soluble He^+ ions [27] also facilitates radiation-induced disintegration of the highly alloyed nickel-alloy, thereby making it easy for the rapid redistribution of the alloying elements in the field of internal stress gradients.

Thus, the conducted studies showed that bombardment of structural materials with light ions can lead to significant structural damages and changes in the chemical and phase composition of the surface layer. The possible mechanisms of the changes in the chemical and phase composition include selective sputtering and radiation-induced accelerated diffusion of elements in the field of internal lateral stresses developing during the He^+ implantation process.

673

LITERATURE CITED

1. B. A. Kalin, N. M. Kirilin, A. A. Pisarev, et al., "A study of blister formation on the surface of niobium and stainless steel under the action of helium ions," in: Reports of the All-Union Conf. on the Technological Problems Related to Controlled Thermonuclear Synthesis (Leningrad, June 26-28, 1974) [in Russian], Vol. 4, NIIÉFA, Leningrad (1975), pp. 150-165.

2. S. Das and M. Kaminsky, "Radiation blistering in metals and alloys," in: Radiational Effects on Solid Surfaces, Washington (1976), pp. 112-170.

3. D. Mazey, B. Eyre, J. Evans, et al., "A transmission electron microscopy study of molybdenum irradiated with helium ions," J. Nucl. Mater., 64, No. 1/2, 145-156 (1977).

4. W. Jäger and J. Roth, "Microstructure of Ni and stainless steel after multiple energy He and D implantation," ibid., 93-94, Part B, 756-766 (1980).

5. M. I. Guseva, A. P. Zakharov, B. A. Kalin, et al., "Electron microscopy study of helium distribution in a high-nickel alloy," At. Energ., 52, No. 6, 401-404 (1982).

6. E. E. Goncharov, M. I. Guseva, B. A. Kalin, et al., "Effect of heat treatment and alloying on the radiational erosion of austenitic stainless steels and alloys," ibid., 53, No. 4, 243-250 (1982).

7. M. I. Guseva, A. N. Mansurova, O. S. Naftulin, et al., "Effect of hydrogen ion bombardment on the structure and chemical composition of a high-nickel alloy," ibid., 54, No. 2, 134-135 (1983).

8. M. I. Guseva, M. E. Evmenenko, S. M. Ivanov, et al., "Radiational erosion of high-nickel alloys and the stainless steel 06Kh17G15NAB during irradiation with helium ions," Vopr. At. Nauki Tekh., Ser. Termoyaderny Sintez, No. 3 (13), 42-48 (1983).

9. E. Johnson, T. Wohlenberg, and W. Grant, "Crystalline phase transition produced by ion implantation," Phase Transit., 1, No. 1, 23-34 (1979).

10. N. M. Beskorovainyi, B. A. Kalin, V. N. Kulagin, et al., "Effect of heat treatment, alloying, and holding in lithium on the radiational erosion of the 16-15 stainless steels," Poverkhn., Fiz., Khim., Mekh., No. 10, 83-90 (1983).

11. P. B. Hirsch, A. Howie, R. B. Nicholson, D. W. Pashley, and M. J. Whelan, Electron Microscopy of Thin Crystals, Butterworths, London (1965).

12. L. M. Utevskii, Diffraction Electron Microscopy in Metals Science [in Russian], Metallurgiya, Moscow (1973).

13. V. Chernikov and A. Zakharov, in: Third Conf. on Applied Electron Microscopy, Zakopane, Eindhoven (1979), p. 20.

14. J. Bennetch, M. Sattler, L. Schiestle Horton, et al., "HVEM observation of in-situ He-ion bombardments," J. Nucl. Mater., 85-86, Part B, 665-669 (1979).

15. A. S. Nikiforov, A. P. Zakharov, V. I. Chuev, et al., "Helium problem in the structural materials of thermonuclear reactors," At. Energ., 53, No. 1, 3-13 (1982).

16. V. I. Shcherbak, V. N. Bykov, V. D. Dmitriev, and S. I. Porollo, "Effect of irradiation conditions and chemical composition on the development of radiational damage in the neutron irradiated steels and alloys," ibid., 46, No. 2, 91-96 (1979).

17. P. Johnson and D. Mazey, "The gas-bubble superlattice and the development of surface structure in He⁺ and H⁺ irradiated metals at 300°K," J. Nucl. Mater., 93-94, Part B, 721-727 (1980).

18. V. N. Bykov, G. G. Zdorovtseva, V. A. Troyan, et al., "A study of molybdenum irradiated with singly charged helium ions," Fiz. Met. Metalloved., 34, No. 3, 666-668 (1972).

19. J. S. Palatnik, A. A. Kozma, M. Ya. Fuks, et al., "A study of the helium solutions implanted in the epitaxial foils of fcc metals," Poverkhn., Fiz., Khim., Mekh., No. 4, 116-121 (1982).

20. V. S. Karasev, V. G. Kovyrshin, G. A. Vorontsova, et al., "Kinetics of helium liberation from the helium ion-irradiated 0Kh16N15M3B steel," Vopr. At. Nauki Tekh., Ser. Fiz. Rad. Povrezhd. Rad. Mater., No. 2, (13), 82-86 (1980).

21. R. Kelly and H. Matzke, "The application of diffusion theory to inert-gas motion in ion-bombarded solids," J. Nucl. Mater., 20, No. 2, 171-183 (1966).

22. L. Caspers, A. Van Veen, A. Ran Gorcum, et al., "Helium desorption from a (110) Mo crystal," Phys. Status Solidi, 37, (A), 371-383 (1976).

23. G. Van der Kolk, A. Van Veen, and L. Caspers, "The interaction of He with C in α-Fe," Delf. Progr. Rep., 4, No. 1, 19-28 (1979).

24. V. Kirsanov and M. Zhetbaeva, "Process of interstitial trapping by impurities," Solid-State Commun., 29, No. 4, 365-370 (1979).

25. A. M. Parshin, I. V. Gorynin, V. G. Azbukin, and A. A. Gorbakon', High-Temperature Strength and Inter-granular Corrosion-Resistance of the Kh20N45 type alloys [in Russian], LDNTP, Leningrad (1971).

26. A. M. Parshin, Structure, Strength, and Ductility of Stainless and Heat-Resistant Steels and Alloys Employed in Shipbuilding [in Russian], Sudostroenie, Leningrad (1972).

27. D. M. Skorov, B. A. Kalin, I. I. Chernov, and A. A. Volkov, "Experimental and Computational Analysis of helium redistribution during the ion-bombardment process," in: Abstracts of the XIV Conf. on Physics of Interaction of Charged Particles with Crystals [in Russian], Moscow State Univ., (1984), p. 12.

CRACK RESISTANCE OF COLD-WORKED 09Kh16N15M3B STEEL SHEETS

V. Yu. Gol'tsev, O. G. Kudryavtsev,   UDC 539.4
Yu. G. Matvienko, and V. V. Novikov

During the operation of nuclear reactors, microcracks can form in the material of the fuel-element cans (jackets) because of the mechanical action of the fuel and the chemical interaction of the fission products with the can material [1]. The efficiency of the fuel elements is determined by the crack resistance of the material, which, in turn, depends on the size of the existing defects, the magnitude of load, and the properties of the material.

The structure and the mechanical properties of the materials are considerably affected by the nature of the prior treatments such as the degree of cold deformation [2]. The optimum degree of cold deformation of stainless steels was previously evaluated [3, 4] from the standpoint of reducing radiation-induced swelling. In this connection, it is necessary to study the effect of cold deformation on the crack resistance of the material.

TABLE 1. Mechanical Properties of the Experimental Materials

Steel	Specimen orientation	Degree of prior deformation of specimens, %	$\sigma_{0,2}$, MPa	σ_b, MPa	δ, %	δ_p, %
09Kh16N15M3B	Longitudinal	Annealed	290	585	20	—
		20	800	845	11	—
	Transverse	Annealed	227	554	55	40
		20	780	860	14	—
modified 09Kh16N15M3B	Longitudinal	Annealed	210	595	55	50
		20	631	726	12,4	10
		30	802	838	9,0	8,2
		40	881	907	4,2	2,5
	Transverse	Annealed	208	565	46	42
		20	748	798	21	16
		30	843	885	14	9,4
		40	958	1020	7,0	2,4

Note: Tables 1 and 2 give the arithmetic average values of the mechanical properties and the crack resistance parameters of three test specimens.
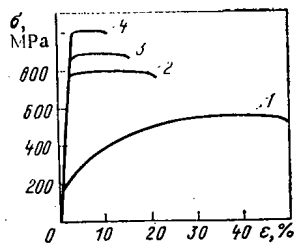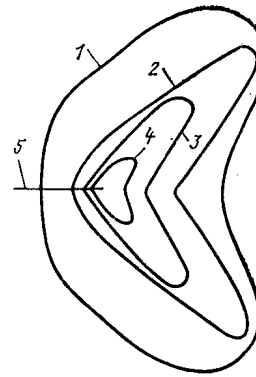
Fig. 1

Fig. 2

Fig. 1. Deformation diagrams of transverse specimens (cut out in the direction perpendicular to the rolling direction) of the modified steel 09Kh16N15M3B: 1) annealed material; 2, 3, 4) deformed by 20, 30, and 40%, respectively.

Fig. 2. Lines of equal plastic deformation (close to 8%) in the transverse specimens of the modified 09Kh16N15M3B steel: 1-4) see Fig. 1; 5) crack.

TABLE 2. Static-Crack-Resistance Characteristics of the Experimental Materials

Steel	Specimen orientation	Degree of cold deformation of the specimens, %	Thickness, mm					
			0,4			0,8		
			σ_{c0}, MPa	δ_c, mm	J_c, MPa·mm	σ_{c0}, mm	δ_c, mm	J_c, MPa·mm
09Kh16N15M3B	Longitudinal	Annealed				450	0,7	315
		20	770	0,35	194	845	0,5	307
	Transverse	20	780	0,35	211	860	0,5	310
Modified 09Kh16N15M3B	Longitudinal	Annealed	408	0,49	140	410	0,7	225
		20	736	0,2	104	705	0,23	116
		30	803	0,15	68	818	0,21	100
		40	908	0,14	32	917	0,17	86
	Transverse	Annealed	408	0,48	256	440	0,7	370
		20	853	0,31	267	816	0,4	380
		30	977	0,24	131	981	0,33	250
		40	1014	0,24	106	1066	0,26	195

We studied the room temperature crack resistance of the 09Kh16N15M3B stainless steel in sheet form and its modifications used for producing the fuel-element cans. The materials were studied in the austenitic condition and after different degrees of cold deformation (up to 40%). In order to evaluate the mechanical properties, sheet specimens were tested in tension according to GOST 11074-66 (Fig. 1, Table 1). The deformation diagrams indicate that the austenitic materials possess considerable ductility, and that their ductility decreases and strength increases with increasing degree of prior cold deformation.

Crack resistance of the materials was evaluated from the results of the static tensile tests conducted on the longitudinal and transverse sheet specimens (width B = 40 mm, length 200 mm, and thickness t = 0.4 and 0.8 mm with a 0.2-mm-wide centrally located transverse through-slot).

Under tensile loading, the moment of crack initiation (start of crack extension) in the specimens having a central slot is preceded by the formation of slip bands, opening of the slot tip, localized plastic deformation, and flow of metal in the zone ahead of the crack tip. The shape of the plastic (deformation) zone undergoes changes with increasing degree of cold deformation: from rounded pear-shape in the austenized material up to narrow bands (oriented at an angle of 35° with respect to the crack) in the cold worked material. In this case, the band width decreases with increasing prior cold deformation (Fig. 2). Such a plastic-zone configuration is typical for low strain-hardening or non-strain-hardening materials [5] in which the ratio of the ultimate strength and the yield strength tends towards unity (see Fig. 1).

The observed ductile fracture of the test specimens of both the steels with significant plastic deformation requires the application of the methods of nonlinear fracture mechanics.
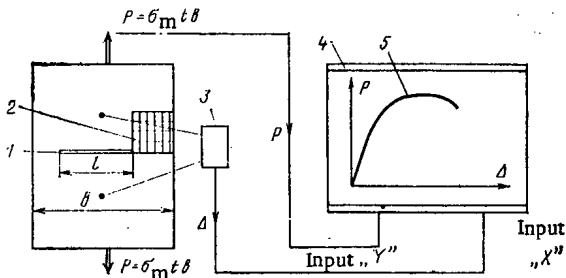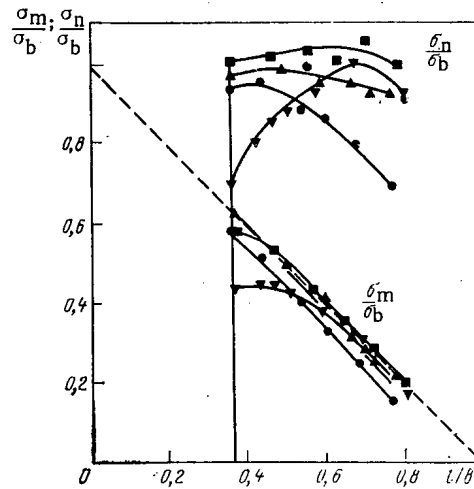
676

Fig. 3

Fig. 4

Fig. 3. Scheme for determining the crack-resistance of sheet materials: 1) crack; 2) grid; 3) displacement gauge; 4) x—y recorder; 5) load (P) vs displacement (Δ) diagram.

Fig. 4. Deformation diagrams of the longitudinal specimens of the modified 09Kh16N15M3B steel: ▼) annealed material; ●, ▲, ■) 20, 30, 40% deformation, respectively.
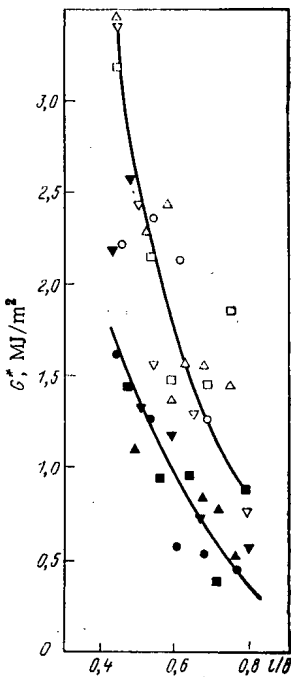

Fig. 5

Fig. 6

Fig. 5. Dependence of the intensity of plastic absorption on the relative crack length in the modified 09Kh16N15M3B steel: open symbols) transverse specimens; dark symbols) longitudinal specimens; ▼, ▽) annealed material; ●, O) 20% deformation; ▲, △) 30%; ■, □) 40%.
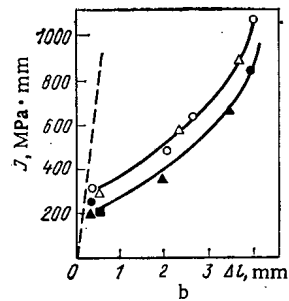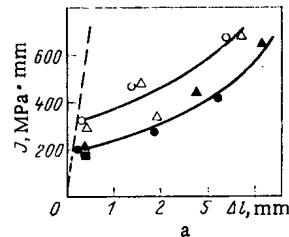
Fig. 6. J_R-curves of the 09Kh16N15M3B steel after 20% cold deformation: a) longitudinal specimens; b) transverse specimens; open symbols) 0.8-mm-thick specimens; dark symbols) 0.4-mm-thick specimens; O, ●) $l_0 = 8$ mm; △, ▲) $l_0 = 15$ mm; □, ■) $l_0 = 20$ mm, – – –) $J = 2M\sigma_{0.2}\Delta l$.

677

For carrying out a more complete evaluation of the fracture resistance of can-steels, a multicriterion approach [6] was adopted that permits one to study: the deformation fields in the crack-tip zone; the fracture diagrams in the coordinates σ_n/σ_b vs l/B and σ_m/σ_b vs l/B, where $\sigma_n = P/[t(B-l)]$; $\sigma_m = P/tB$; l, crack length at the moment of observation; P, current value of the load; and the stress required for crack initiation $\sigma_{c0} = P_c/[t(B-l_0)]$, where P_c is the crack-initiation load; l_0, original crack length; δ_c, critical crack-tip opening; J_c, critical value of the J_i-integral (at the moment of crack initiation); G^*, intensity of plastic absorption during the process of crack growth; and J_R, resistance of the material to stable crack growth.

When testing the specimens, the load versus notch-edge displacement diagram (Fig. 3) was autographically recorded on an x−y plotter PDP 4-002, and the crack-tip opening and the crack extension were noted; the tip opening at the moment of crack initiation was observed using a MPB-2 microscope. The deformation fields in the crack-tip region were determined using the grid method. These initial data were used for evaluating the crack resistance. The procedures for determining all the characteristics were described in detail elsewhere [6, 8].

The deformation diagrams (Fig. 4), plotted in the σ_n/σ_b vs l/B and σ_m/σ_b vs l/B coordinates, form a generalized characteristic of fracture resistance. The failure process is characterized by stable crack growth that is virtually independent of the degree of prior deformation; however, σ_{c0} increases significantly after prior cold deformation of the material. The crack propagates at a stress equal to or even slightly greater than the ultimate strength.

In the case of the notched specimens of the modified 09Kh16N15M3B steel (Table 2), σ_{c0} gradually increases with increasing degree of prior cold deformation. This phenomenon is related to the strain hardening of the material. At the same time, the effect of the rolling direction (specimen orientation) becomes increasingly apparent: the transverse specimens exhibit greater resistance to fracture than the longitudinal specimens. Even at 20% cold deformation, crack initiation is observed at a stress σ_{c0} equal to the ultimate strength independent of the original crack length and the specimen thickness.

The critical crack-tip opening δ_c at the moment of crack initiation characterizes the local ductility of the modified 09Kh16N15M3B steel. It decreases with increasing degree of cold deformation. This fact agrees well with the observed simultaneous reduction of ductility δ. Based on the δ_c values, it may be concluded that the transverse specimens possess a high crack resistance in the cold worked condition.

The J_c-integral forms a generalized energy parameter of fracture resistance. It characterizes the critical stress (deformation) state of the region ahead of the tip at the moment of crack initiation. The value of J_c is determined by the energy expended (work done) in plastically deforming the crack-tip region and in propagating the crack. The dependence of the J_c-integral on the degree of cold deformation of the modified 09Kh16N15M3B steel is nonmonotonic: after attaining the maximum at 20% cold deformation, it starts to decrease in that there is a significant effect of the specimen thickness and its orientation with respect to the rolling direction (the transverse specimens possess higher elastic−plastic fracture toughness). The appearance of the J_c-maximum at 20% cold deformation indicates a significant increase in the strength characteristics (σ_{c0}) and a not-very-significant reduction in the local ductility (δ_c).

Prior cold deformation affects the crack resistance of the 09Kh16N15M3B steel, but in contrast to the modified steel, in this case there is no effect of the specimen orientation relative to the rolling direction.

The observed increase in the critical crack-tip opening and in the value of the J_c-integral with increasing specimen thickness agrees well with the results of the earlier studies on the fracture toughness of ductile steels under plane stress condition [9].

The variation of G^* (Fig. 5) at identical values of crack extension indicates a high degree of reserve ductility of the specimens of both the materials and insensitivity of this parameter to the changes in the degree of prior cold deformation. An analysis of the J_R-curves (Fig. 6) also yielded a similar result. This analysis showed a slightly higher resistance of the material of the transverse specimens to stable crack-growth at a given crack extension Δl.

Thus, based on the analysis of the room-temperature fracture-resistance characteristics of the 09Kh16N15M3B and its modification, the following conclusions can be drawn:

the strength properties as well as the crack resistance of the 09Kh16N15M3B steel and its modification increase with increasing cold deformation up to 20%;

an increase in the degree of prior cold deformation intensifies the effect of the rolling direction (specimen orientation) on the characteristics of static crack resistance (the transverse specimens possess higher crack resistance); and

the static crack resistance decreases with decreasing material thickness.

In order to confirm the obtained regularities governing the fracture behavior of the can materials (and products), it is necessary to conduct additional experiments under the conditions approaching the service conditions.

<div align="center">LITERATURE CITED</div>

1. V. A. Tsykanov and E. F. Davydov, Radiation Stability of Heat Dissipating Elements of Nuclear Reactors [in Russian], Atomizdat, Moscow (1977).
2. N. P. Agapova, V. S. Ageev, V. A. Krasnoselov, et al., "Radiation swelling of structural materials of the fast-reactor cores," Vopr. At. Nauki Tekh., Ser. At. Mater., 15, No. 4, 12-19 (1982).
3. V. A. Krasnoselov, V. I. Prokhorov, A. N. Kolesnikov, Z. A. Ostrovskii, "Effect of prior thermomechanical treatment on the swelling of the stainless steel 09Kh16N15M3B," At. Energ., 54, No. 2, 111-114 (1983).
4. G. Ranjan and E. Smith, "Determination of stress within zircalloy cladding due to PCE," Nucl. Eng. Design, 56, 263-272 (1980).
5. A. A. Movchan, "Crack movement through a specimen of the VT5-1 titanium alloy," Izv. Akad. Nauk SSSR, Ser. Mekh. Tverd. Tela, No. 2, 178-181 (1975).
6. Yu. G. Matvienko and V. Yu. Gol'tsev, "Evaluation of crack resistance of thin sheets of metallic materials according to the nonlinear fracture mechanics criteria," Zavod. Lab., No. 5, 70-73 (1984).
7. A. A. Volkov, V. Yu. Gol'tsev, Yu. G. Matvienko, and D. Yu. Tyukhmenev, "Energy absorption in the plastically deformed zone during propagation of a viscous crack," in: Strength and Lift of Nuclear Engineering Materials and Structures [in Russian], Energoatomizdat, Moscow (1982), pp. 22-26.
8. Yu. G. Matvienko and V. Yu. Gol'tsev, "Application of the grid method for plotting the J_R-curve," Zavod. Lab., No. 10, 70-73 (1983).
9. V. Yu. Gol'tsev, B. A. Drozdovskii, and L. V. Prokhodtseva, "Effect of the thickness of metallic materials on their ability to inhibit fracture," ibid., No. 10, 1237-1241 (1969).

RESEARCH IN THE DISCHARGE OF RADIONUCLIDES
TO THE ATMOSPHERE AND ASSESSMENT OF THE MAXIMUM
PERMISSIBLE DISCHARGES IN THE CONTEXT
OF THE REPROCESSING OF NUCLEAR POWER PLANT FUEL
ELEMENTS

I. N. Ruzhentsova, R. V. Semova,   UDC 004.86
E. N. Teverovskii, and I. A. Ternovskii

In accordance with the nuclear-power development plans of many countries in the world in recent years, a transition to a closed nuclear fuel cycle with spent-fuel recycling is in progress. The reprocessing of the fuel is the most hazardous process as far as radiation is concerned, and it is accompanied by the discharge of long-lived radionuclides to the atmosphere. The composition of the discharge depends on the nature of the fuel being reprocessed, the reactor campaign, the holdup time of the fuel after it has been unloaded, and also on the technological characteristics of the recycling process and the efficiency of the gas purifiers used.

In the present article we present the results of research in the atmospheric discharge of fission and neutron-activation products, and also of transuranium elements, which were obtained during the operation of facilities for recycling spent VVÉR (water-moderated, water-cooled power reactor) fuel elements.

TABLE 1. Experimental Values of Radio-nuclide Discharges to Atmosphere

Radionuclide	Q'	Standard discharge,* Bq/[MW(e)·yr]
^{3}H	$2{,}5 \cdot 10^{-4}$	$2{,}0 \cdot 10^{8}$
^{90}Sr	$2{,}5 \cdot 10^{-8}$	$2{,}3 \cdot 10^{6}$
^{106}Ru	$2{,}2 \cdot 10^{-8}$	$3{,}2 \cdot 10^{6}$
^{129}I	$0{,}25$	$1{,}1 \cdot 10^{7}$
^{134}Cs	$1{,}8 \cdot 10^{-8}$	$2{,}0 \cdot 10^{6}$
^{137}Cs	$2{,}5 \cdot 10^{-8}$	$5{,}2 \cdot 10^{6}$
^{144}Ce	$2{,}8 \cdot 10^{-8}$	$2{,}9 \cdot 10^{6}$
^{239}Pu$+^{240}$Pu	$5{,}7 \cdot 10^{-9}$	$7{,}0 \cdot 10^{3}$
^{238}Pu	$7{,}0 \cdot 10^{-9}$	$1{,}3 \cdot 10^{4}$
^{241}Am	$3{,}6 \cdot 10^{-8}$	$7{,}0 \cdot 10^{3}$
^{244}Cm	$3{,}4 \cdot 10^{-9}$	$5{,}2 \cdot 10^{3}$
^{85}Kr	$1{,}0$	$1{,}1 \cdot 10^{13}$

* Discharge standardized on 1 MW(e)·yr.

TABLE 2. Values of DCF_{ni} (Sv·m³/(yr·Bq))

Radionuclide	$0{,}4DCF_{1i}$	$0{,}4DCF_{2i}$	DCF_{3i}	DCF_{4i}
^{3}H	—	—	$1{,}6 \cdot 10^{-6}$	$1{,}4 \cdot 10^{-6}$
^{90}Sr	—	—	$2{,}6 \cdot 10^{-2}$	$5{,}6$
^{106}Ru$+^{106}$Rh	$8 \cdot 10^{-7}$	$1{,}5 \cdot 10^{-3}$	$2{,}1 \cdot 10^{-3}$	$5{,}3 \cdot 10^{-2}$
^{129}I	$2{,}0 \cdot 10^{-7}$	$2{,}8 \cdot 10^{-3}$	$1{,}5 \cdot 10^{-2}$	$1{,}5$
^{134}Cs	$1{,}3 \cdot 10^{-6}$	$1{,}9 \cdot 10^{-2}$	$9{,}3 \cdot 10^{-4}$	$2{,}3 \cdot 10^{-1}$
^{137}Cs$+^{137m}$Ba	$4{,}8 \cdot 10^{-7}$	$2{,}5 \cdot 10^{-2}$	$8{,}2 \cdot 10^{-4}$	$1{,}5 \cdot 10^{-1}$
^{144}Ce$+^{144}$Pr	$4{,}4 \cdot 10^{-8}$	$3{,}0 \cdot 10^{-4}$	$1{,}9 \cdot 10^{-3}$	$2{,}0 \cdot 10^{-2}$
^{239}Pu$+^{240}$Pu	$1{,}9 \cdot 10^{-9}$	$1{,}1 \cdot 10^{-3}$	$5{,}5$	$1{,}0$
^{238}Pu	$1{,}4 \cdot 10^{-9}$	$7{,}6 \cdot 10^{-4}$	$2{,}5$	$1{,}8 \cdot 10^{-1}$
^{241}Am	$2{,}4 \cdot 10^{-8}$	$3{,}2 \cdot 10^{-3}$	$4{,}3$	—
^{244}Cm	$1{,}3 \cdot 10^{-9}$	$6{,}8 \cdot 10^{-4}$	$4{,}9$	—
^{85}Kr	$1{,}9 \cdot 10^{-9}$	—	—	—

One can assess the maximum permissible discharge (MPD), and also the possible doses to which the population is exposed through the operation of the fuel-element recycling facilities, by using data pertaining to a relative discharge, i.e., pertaining to that proportion of a radionuclide in the fuel being recycled which is discharged to atmosphere during the complete reprocessing of the batch of fuel elements: $Q' = A_Q/A_m$, where Q' is the relative discharge; A_Q is the activity of the radionuclide being discharged to atmosphere, and A_m is the activity of the radionuclide in the fuel being reprocessed.

The relative-discharge data make it possible to assess the degree of environmental contamination caused by the operation of the fuel-element recycling facilities and to predict the levels of contamination arising from a given quantity of fuel undergoing reprocessing.

The specific activity of a fission product with a mass number i in the VVÉR-440 fuel being recycled is given by (Bq/t):

$$A_i = 1{.}0 \cdot 10^{16} \, (Y_i^a a + Y_i^b b + Y_i^c c) \, (1 - e^{-\lambda_i \Delta t}) e^{-\lambda_i \Delta T},$$

where Y_i^a, Y_i^b, and Y_i^c is the cumulative yield of the radionuclide from the fission by thermal neutrons of ^{235}U, ^{239}Pu, and ^{241}Pu, respectively (%); a, b, and c is the contribution from the fission of the ^{235}U, ^{239}Pu, and ^{241}Pu nuclides to the power produced by the reactor; ΔT is the holdup time of the fuel pending recycling; $\Delta t = 8{.}4 \cdot 10^{-2}$ E is the reactor campaign (years), and E is the burnup. The specific activity of the neutron–activation product of the ^{134}Cs in the fuel being recycled is determined as follows:

$$A_{134} = 1{.}0 \cdot 10^{16} \left(\sigma_{133}^0 \sqrt{\frac{\pi 293}{4 T_{\text{н}}}} + \alpha R \right) nv \, (Y_{133}^a a + Y_{133}^b b + Y_{133}^c c) \left[\Delta t + \frac{1}{\lambda_{134}} (e^{-\lambda_{134} \Delta t} - 1) \right] e^{-\lambda_{134} \Delta T},$$

where σ_{133}^0 is the activation cross section for $T_N = 293°$K; T_N, apparent neutron temperature; α, epithermal neutron fraction; R, resonance interval; nv, density of the thermal neutron flux in the reactor core (cm$^{-2} \cdot$sec^{-1}), and 133 and 134, mass numbers of the ^{133}Cs and ^{134}Cs nuclei.

The activity of the transuranium elements in the fuel was determined by reference to the data of [1]. The measurements of the radionuclide discharges to atmosphere were carried out by sampling the aerosols, gases, and vapors present in the gas–air mixture discharged to atmosphere through ventilation shafts.

The radionuclide composition of the aerosols was determined with a gamma–spectrometer, the ^{129}I content was measured on an x-ray analyzer, and the ^{3}H content was measured in situ with a liquid scintillation counter. For the determination of the activity of the transuranium elements we used a radiochemical separation and de-contamination procedure, including ion–exchange and extraction–chromatography methods followed by mea-surements on an alphaspectrometer (Table 1).

The error in measuring a discharge is not greater than 40%. The data given in Table 1 indicate that the Q' value of radionuclides in aerosol form is $3{.}4 \cdot 10^{-9}$–$3{.}6 \cdot 10^{-8}$ and that it is close to the Q' value for the NFS reprocessing facility in the U.S.A. $(0{.}1 \cdot 10^{-9}$–$10 \cdot 10^{-8})$ [2].

Later we shall give assessments of the MPDs of the radionuclides to atmosphere for a fuel reprocessing facility with a throughput of 1500 ton/yr, which is typical of the published reprocessing facility projects [3].

In a mixture of radionuclides, the MPD of the ith radionuclide is given by the following expression (Bq/yr):

$$\mathrm{MPD}_i = 3.2 \cdot 10^7 \, (\, \mathrm{PK}_{Bi} - C_{\phi i}) k_d,$$

where PK_{Bi} is the average annual permissible concentration of the i-th radionuclide in respect of Category B persons as far as the discharge of the radionuclides mixture is concerned (Bq/m^3); $C_{\phi i}$ is the background concentration of the i-th radionuclide (Bq/m^3), and k_d is the average annual dilution factor (m^3/sec).

The values of PK_{Bi} can be calculated from the equation:

$$(\, \mathrm{PK}_{Bi}/\eta_i) \left(\sum_i \eta_i / \, \mathrm{PK}_{Bi}^{\cdot} \right) = 1 \ \text{and} \ \mathrm{PK}_{Bi} = \eta_i \, \mathrm{PK}_{Bi}^{\cdot},$$

where $\eta_i = Q_i/Q_j$ is the i-th radionuclide discharge divided by the reference j-th radionuclide discharge; $\mathrm{PK}_{Bi}^{\cdot} = MD/\sum_n DCF_{ni}$ is the average annual permissible concentration with respect to Category B persons as far as the i-th radionuclide discharge is concerned (Bq/m^3); MD is the maximum dose to which the group of critical organs is exposed (Sv/yr); DCF_{ni} is the dose conversion factor, which is equal to the dose rate to which the group of critical organs is exposed in respect of the nth exposure pathway over the average annual permissible concentration of the i-th radionuclide in the near-ground layer of the atmosphere $(Sv \cdot m^3/(Bq \cdot yr))$.

The experimental values of the average annual dilution factor for trace and highly dispersed contaminants in the areas proposed for the sites of the facilities with variable wind-behavioral characteristics at the effective discharge-source height of 200 m are given in [4].

It is necessary to assess the values of DCF_{ni} relating to the principal exposure pathways, namely, the external exposure due to the plume and the radioactive aerosols deposited on the surface of the soil, and the internal exposure resulting from the inhalational and peroral ingress of the radionuclides into the human body.

As a result of immersion in the discharge cloud we determined the values of DCF_{1i} by a γ-method based on the radiation-equilibrium principle [5]:

$$DCF_{1i} = 2.1 \cdot 10^{-6} \sum_k n_k E_{\gamma k}, \tag{1}$$

where $E_{\gamma k}$ is the energy of the γ-quanta (MeV), and n_k is the yield of γ-quanta of energy $E_{\gamma k}$ per nuclear decay.

As a result of the contamination of the surface of the soil we assessed the values of DCF_{2i} with the formula:

$$DCF_{2i} = DCF_{2i}^{\prime} \frac{v_g}{\lambda_{eff}} (1 - e^{-\lambda_{eff} \, t}), \tag{2}$$

where DCF_{2i} is the dose-conversion factor, which is equal to the exposure rate divided by the density of soil-surface contamination; v_g, turbulent-deposition velocity (m/sec); λ_{eff}, activity decay constant of the radionuclide in the top layer of soil resulting from radioactive decay and percolation into underlying layers, and $t = 70$ years time it takes to reach the cumulative or equilibrium surface-contamination density.

In the case of most long-lived radionuclides, $\lambda_{eff} = 4.4 \cdot 10^{-9} \, sec^{-1}$; in the case of the short-lived ones, $\lambda_{eff} = 0.693/T_{1/2}$ and $DCF_{2i} = DCF_{2i}^{\prime} v_g/\lambda_{eff}$.

In the calculation of $DCF_{2i}^{\prime}$ we took into account the plural scattering of the γ-quanta by assuming an isotropic γ-radiation distribution [6]:

$$DCF_{2i}^{\prime} = 3.0 \cdot 10^{-7} \sum_k n_k E_{\gamma k} \left[-Ei(-\mu_i h) + \frac{C}{1-D} e^{-(1-D)\mu_i h} \right], \tag{3}$$

where $Ei(-\mu_i h)$ is the integral exponential function, μ_i is the linear γ-radiation attenuation factor (m^{-1}); $h = 1$ m is the height of the detector above the surface of the soil, and C, D are constants depending on the energy of the γ-quanta.

In the assessments of DCF_{2i} and DCF_{1i} it is necessary to take into account a correction factor to characterize γ-radiation shielding by buildings, and also the average time (in a year) a person spends outdoors. According to the data in [2], this factor is equal to 0.4.

The assessment of DCF_{3i}, which is for the internal exposure due to inhalation, was carried out on the basis of the values laid down in NRB-76 [7] for the maximum annual intake [MAI] into the body in the case of Category-B persons:

$$DCF_{3i} = \frac{MD \cdot V}{MAI_i}, \tag{4}$$

681

where $V = 7.3 \cdot 10^3$ m³/yr is the volume of inhaled air.

The basis of the calculation of DCF_{4i}, which is for the internal exposure due to the peroral ingress of the radionuclides into the human body, was the expression [8]:

$$DCF'_{4i} = \frac{MD}{MAI_i} v_g \left\{ \sum_l m_l \Delta_l B_l \left[k_{nl} + \frac{k_{pl}}{\lambda'_{eff}} (1 - e^{-\lambda'_{eff} t}) \right] + \right.$$

$$\left. + \sum_l m_l \Delta_l B_l m \delta_l \left[k_{nl} + \frac{k_{nl}}{\lambda'_{eff}} (1 - e^{-\lambda'_{eff} t}) \right] \right\},$$

(5)

where m_l is the annual consumption of the l-th foodstuff (kg/yr); Δ_l, fraction of radionuclide content of the l-th foodstuff found after the processing of the original agricultural produce; B_l, a factor to take into account the average annual concentration of the radionuclide in the foodstuffs consumed in a year; m, daily fodder consumption of agricultural livestock (kg/day); δ_l, fraction of radionuclide passing into 1 kg of animal product from the content of the daily fodder ration (days/kg); k_{Bl}, resultant radionuclide concentration in the l-th plant product (fodder) at the time of production divided by the fallout rate of the radionuclide in question (m²·sec/kg); k_{pl}, resultant concentration of the long-lived radionuclide in the l-th plant product (fodder) divided by the soil-contamination density (m²/kg); and λ'_{eff}, a constant relating to the effective loss of radionuclide from the root inhabited soil layer (sec⁻¹).

For the ³H, which occurs in discharges as HTO vapor, the DCF_{4^3H} was determined with the formula:

$$DCF_{4^3H} = \frac{MD}{MAI_{3H}} \frac{1}{\rho} \Sigma m_l^f R_l,$$

(6)

where m_l^f is the annual uptake with the water in the composition of the l-th foodstuff (kg/yr); R_l, specific ³H activity of the l-th foodstuff divided by the specific activity of the moisture in the atmosphere; and ρ, mass moisture content of the atmosphere (kg/m³). The values of the parameters to be inserted into formulas (5) and (6) are given in [8].

In Table 2 we give the values of DCF_{ni}, which have been calculated with the aid of formulas (1)-(6), for the radionuclides discharged during the reprocessing of nuclear power plant fuel elements. The solubility of the radionuclides is not known.

Here we now give the values for the MPDs of the radionuclides characterizing a nuclear power plant fuel-element reprocessing facility, which have been standardized on 1 MW(e)·yr in case it is sited in areas with a variable wind-rose draft:

$$
\begin{aligned}
^3H & \dots (0.6 - 1.8)10^{10} \\
^{90}Sr & \dots (0.7 - 2.1)10^8 \\
^{106}Ru & \dots (1.0 - 3.0)10^8 \\
^{129}I & \dots (3.3 - 9.9)10^8 \\
^{134}Cs & \dots (0.6 - 1.8)10^8 \\
^{137}Cs & \dots (1.6 - 4.8)10^8 \\
^{144}Ce & \dots (0.9 - 2.7)10^8 \\
^{239}Pu + {}^{240}Pu & \dots (2.1 - 6.3)10^5 \\
^{238}Pu & \dots (0.4 - 1.2)10^6 \\
^{241}Am & \dots (2.1 - 6.3)10^5 \\
^{244}Cm & \dots (1.6 - 4.8)10^5 \\
^{85}Kr & \dots (3.3 - 9.9)10^{14}
\end{aligned}
$$

In the calculation of the MPDs we took into account the I.C.R.P. Recommendation that the radiation dose to individual members of the population should not be greater than 5 mSv/yr. Accordingly, we determined the effective equivalent dose with the formula [9]:

$$H = \sum_m \omega_m H_m,$$

where ω_m is the weighting factor and H_m is the dose to the m-th organ (tissues).

In the assessment of the MPDs we took into account the average food ration. We assumed that all foodstuffs consumed by the population are produced in the locality, that the sources of mains drinking water are artesian wells, and that the background radiation is small.

Should the fuel-element recycling facility be in an area with considerable background contamination, the MPDs of the radionuclides must be reduced $PK_{Bi} - C_{\Phi i}/PK_{Bi}$ times.

From a comparison of the data shown it follows that the factual discharges of radionuclides to atmosphere during the operation of a facility for recycling fuel elements from nuclear power plant reactors are 30-90 times

682

smaller than the values for the MPDs which are assessed in the light of the proposed areas for siting it with variable wind—behavioral characteristics.

LITERATURE CITED

1. A. K. Kruglov and A. Rudik, Artificial Isotopes and Methods for Calculating Their Abundance in Nuclear Reactors [in Russian], Atomizdat, Moscow (1977).
2. Ionizing Radiation: Sources and Biologic Effects, NKDAR Report for 1982, Vol. 1, New York (1982).
3. N. S. Babaev, B. F. Demin, L. A. Il'in, et al., Nuclear Power, Man and the Environment [in Russian], Énergoizdat, Moscow (1981).
4. I. N. Ruzhentsova and E. N. Teverovskii, "Local radiation effects of atmospheric discharges during the operation of a reprocessing facility," At. Energ., 54, No. 3, 192–194 (1983).
5. N. G. Gusev, V. P. Mashkovich, and A. P. Suvorov, Physical Bases of Radiation Protection [in Russian], Vol. 1, Atomizdat, Moscow (1970).
6. D. Kocher, Health Phys., 38, No. 4, 543 (1980).
7. Radiation Safety Standards NRB-76 and Basic Health Rules OSP-72/80 [in Russian], Énergoizdat, Moscow (1981).
8. N. E. Artemova, E. N. Teverovskii, I. A. Ternovskii, et al., Permissible Discharges of Radioactive and Toxic Chemical Substances to the Near-Ground Layer of the Atmosphere [in Russian], Atomizdat, Moscow (1970).
9. I.C.R.P. Recommendations: Publication No. 26 [Russian tranlation], Atomizdat, Moscow (1978).

DEVELOPING AN OPERATIONAL RADIOGRAPHIC
INSPECTION METHOD FOR THE ELBOW-SHAPED BRANCH
PIPES AT THE NPP WORKING WITH RBMK-1000

A. P. Semenov and V. I. Gorbachev

UDC 620.179.15

In the space below the RBMK-1000 reactor there are sharply bent elbow-shaped branch pipes ("calatches") measuring 57 mm in diameter and having a wall thickness of 4 mm. The weld joints of these pipes must be subjected to periodic inspection during operation. The branch pipes are positioned such that the distance between the pipes in the rows is 125 mm in one direction and 200 mm in the other (Figs. 1 and 2).

Inspection of the equipment and the piping located in the premises under the reactor must be carried out by remote control after the reactor has been stopped and cooled down for a period of 2-3 days. It must be ensured that the γ-radiation background $\leq 1000\ \mu$R/sec (1R $=2.58 \cdot 10^{-4}$ C/kg), and the energy of background γ-radiation must be 1.2 MeV. The radiographic inspection method must ensure a sensitivity specified in the inspection regulations PK 1514-72.

The data on the effect of radiation background on the sensitivity of γ-inspection [1-4] do not always agree among themselves; they are obtained at smaller values of radiation background (up to 500 μR/sec), and do not take into account the specific inspection features in the confined space under the reactor. The inspection procedure involves the application of the series-produced gamma-apparatus fitted with flexible cables in which the radiation source is ^{192}Ir (GII-D-3). The proposed scheme of radiographic inspection (see Fig. 2) makes it possible to examine the welds of three pipelines from a single working position, and ensures 100% inspection of the "elliptical" welds from two working positions at a focal length of 320 mm.

The effect of radiation background on the results of radiographic inspection was studied using the double exposure method: before inspecting the experimental specimens, the radiographic film was exposed to create an artificial fog. This permits one to adequately imitate the inspection conditions under radiographic background, since it was experimentally shown that the sensitivity of a radiographic print is independent of the sequence of operations of superpositioning the artificial fog and the radiation image [5].
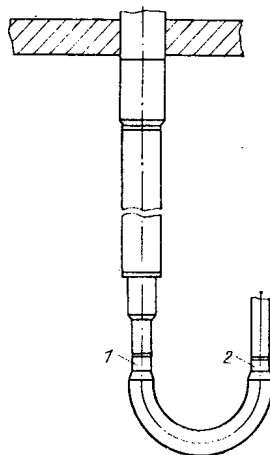

Fig. 1. Scheme of location of the
branch pipes and the control points (1,
2).

684

0038-531X/85/5902-0684$09.50   © 1986 Plenum Publishing Corporation
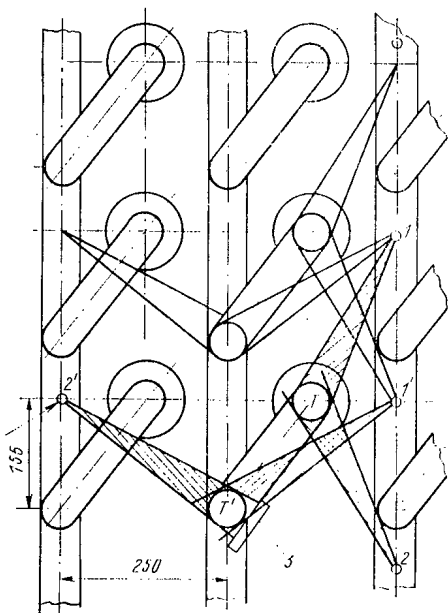
Fig. 2

Fig. 3

Fig. 2. Scheme of the branch pipe location and the working positions of the radiation sources for weld inspection: 1, 2 and 1', 2') working positions of the radiation source for inspecting the joints T and T', respectively; 3) cassette.
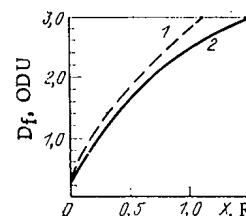
Fig. 3. Dependence of the photographic (optical) density of the radiographic film RT-1 on the exposure dose for different cassette loadings: with 0.09-mm-thick lead screens (1) and without intensifying media (2).

TABLE 1. Detectability Parameters of the Standard Defects

D_f, ODU	Background X, mR	Exposure time at a background EDI of 1000 μR/sec, sec	Slots (GOST 7512-82)		Wires (GOST 7512-82)		Holes*	
			h, mm	range of X, mR	h, mm	range of X, mR	h, mm	range of X, mR
0,2	0	0	0,2	750—1250	0,25	1000	0,5	1000—1250
0,7	100	100	0,25	750—1500	0,32	500—1750	0,6	750—1500
1,0	210	210	0,3	500—1500	0,32	750—1500	0,6	750—1500
1,5	400	400	0,3	750—1250	0,4	750—1250	0,6	1000
2,0	600	600	0,3	1000	0,4	1000	0,7	650—1500
							0,7	750—1250

*The data is for the holes whose diameter and height are equal.

The relationship between the fog density of the radiographic film that is created by the radiographic background and the exposure time was obtained in the case of ^{60}Co γ-radiation source (Fig. 3) whose spectral composition is close to that of the γ rays of the radiation background.

In the present studies we used slotted, wire, and sheet specimens as the sensitivity standards (GOST 7512-82) which were mounted on a 8.0-mm-thick 1Kh18N9T steel plate facing the radiation source. Radioscopy was accomplished using a RT-1 radiographic film with 0.09-mm-thick intensifying lead screens and maintaining a focal length of 320 mm.

The magnitude of the optical density of fogging of the photographs D_f, which includes the initial and the artificial fogging, was determined using a densitometer "Macbeth TD-540." The studies were carried out for five D_f values: 0.2 (initial fog of the film) 0.7, 1.0, 1.5, and 2.0 optical density units (ODU). The dosimetric measurements were conducted using a spherical chamber VA-K-253 (type 70110) of the dosimeter set 27012 (GDR). The exposure dose intensity (EDI) on the surface of the steel plate from the source end amounted to 8.2 mR/sec. The exposure dose X emerging from the GII-D-3 source was measured from 0 up to 2.0 R discretely at 0.25-R intervals. We obtained three prints for each combination of D_f and EDI. They were interpreted by the approved radiography specialists. The results of interpretations were averaged.
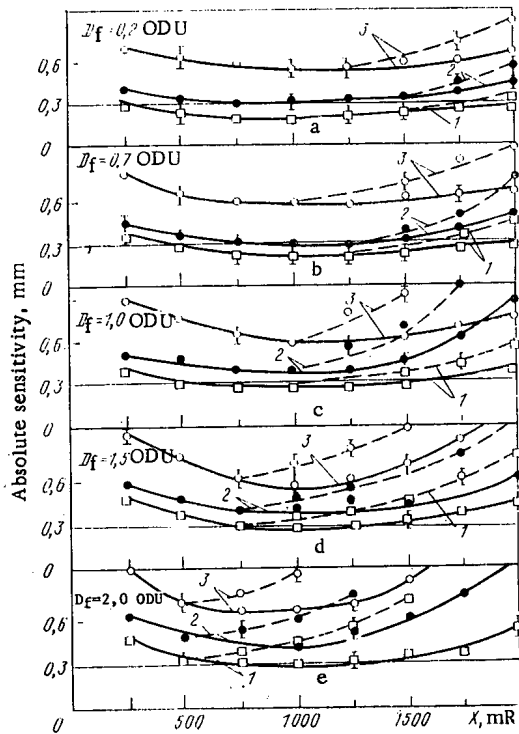
685

Fig. 4

Fig. 5

Fig. 4. Absolute radiographic sensitivity during the inspection of a 8.0-mm-thick steel using a RT-1 film as a function of the exposure dose of useful radiation at different fog values: a, b, c, d, e) D_f is equal to 0.2, 0.7, 1.0, 1.5, and 2.0 ODU, respectively.
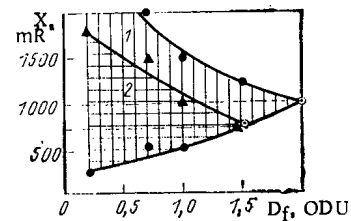
Fig. 5. Region of the exposure doses ensuring detection of the 0.3-mm-deep slots (GOST 7512-75) at different values of D_f and during the inspection of the radiographic prints on an OD-10N negatoscope: 1) on a screen having increased brightness; 2) on a screen with low brightness (up to 3.0 ODU of the print).

The radiographic prints were examined using an OD-10N negatoscope ("Rapan") fitted with two screens, of which one is intended for examining the prints having a photographic density up to 3.0 ODU and the second one is intended for examining the prints with a density up to 4.0 ODU.

Figure 4 shows the dependence of detectability k of different standard defects on the exposure dose at different photographic fog densities: the dashed lines are plotted on the basis of the inspection results obtained on the prints using a screen with less brightness, and the solid lines are plotted on the basis of the results obtained using a screen with increased brightness.

The analysis of the curves shows that for each of the standard defects there is an optimum range of the useful radiation levels, ensuring detection of the defects of a given size. The position of the boundaries of this range depends on D_f, the maximum brightness of the negatoscope screen, and the type of the standard defect.

Based on the curves shown in Fig. 4, we determined the region of the exposure doses of γ radiation that ensures detection of slots (grooves) measuring 0.3 mm in depth (following the specification PK 1514-72 for a 8.0-mm-thick steel sheet) at different D_f values and under different inspection (interpretation) conditions for k = 0.3 (Fig. 5).

With increasing D_f, the range of the optimum exposure doses of γ radiation narrows down, and at a certain brightness of the negatoscope screen it degenerates into a point. This can be attributed to the fact that the radiographically detectable minimum defect size depends on (besides other factors, which were unaltered in the present case) the accumulation of scattered radiation, the changes in the slope of the characteristic plot of the radiographic film caused by the density variation, and the limitations of the negatoscope.

In the case of the other types of defects, the nature of the X versus D_f relationship remains the same as that observed in the case of slots (Fig. 5).

686

Table 1 gives the data on the detectability of the standard defects of different types in a 8.0-mm-thick steel sample examined using a RT-1 film (GII-D-3 γ-ray source; focal length 320 mm). According to the specification PK 1514-72, in the absence of background, the radiographic sensitivity must be 0.25 m for the wire sample under consideration, and 0.27 m for the slotted sample. These data were obtained for the OD-10N negatoscope fitted with a screen that permits one to analyze the prints with a density up to 4.0 ODU. In order to detect the slots measuring 0.3 mm in depth, the EDI given by the working source in the inspection (control) zone must be at least 1.7 times higher than that of the radiation background.

However, for improving the efficiency of inspection and for enabling interpretation of the radiographic prints obtained with standard equipment, we recommend the use of the γ-ray sources whose EDI in the control zone is at least thrice that of the radiation background. Employing the high-activity sources is justified only when the GOST 7512-82 specification on the poor geometric definition of the image has to be met in the given case.

Thus, the conducted studies showed that when the series-produced GII-D-3 γ-ray sources having an activity not less than $40.2 \cdot 10^{10}$ Bq and RT-1 radiographic film are used, it is possible to accomplish radiographic quality control of the welds of the elbow-shaped branch-pipes under the conditions of a radiographic background of 1000 μR/sec and within the confined space below a RBMK-1000 reactor.

LITERATURE CITED

1. A. N. Maiorov, Radiosotopic Defectoscopy [in Russian], Atomizdat, Moscow (1976).
2. A. S. Dekopov and A. N. Maiorov, "Control of welded miter joints under the conditions of radiation background using the gamma-defectoscopy apparatus 'Drozd'," Isotopes in the USSR [in Russian] (1974), pp. 38-42.
3. V. S. Grom, "Radiography of weld joints under the conditions of radiation background," in: Radiation Defectoscopy [in Russian], Atomizdat, Moscow (1970), pp. 103-108.
4. V. S. Grebennik, "Nondestructive control methods employed at nuclear plants," Defektoskopiya, No. 8, 85-101 (1981).
5. A. P. Semenov, L. M. Zhakevich, V. I. Gorbachev, et al., "Radiographic control of reactor elements under the conditions of radiation background," At. Energ., 50, No. 2, 148-149 (1981).

EFFECT OF THE STAGE OF LOOSENING OF A CATIONITE
FILTER ON ITS OPERATING EFFICIENCY
DURING CONDENSATE PURIFICATION AT NUCLEAR POWER
STATIONS

M. A. Argin, I. V. Komarova,
I. M. Zakova, L. M. Alekseeva,
A. A. Neverova, and S. N. Shibkov

UDC 541.183

Condensate purification in nuclear power stations [1] includes the adsorption purification of the condensate from the cations and anions present in it and filtration purification from corrosion products and suspended particles. The process is effected by a technological scheme consisting of two successively connected filters with different or mixed ionite charges, and a cationite filter as a rule fulfils the role of a mechanical filter. The operating efficiency of this filter, therefore, is determined by its filtration and ion-exchange properties.

In the course of the filtration purification of the condensate, clogging of the pore space of the cationite filter by suspended particles occurs (corrosion products, finely divided fractions of ionites), in consequence of which the pressure differential in the system increases. In addition, the pressure differential is increased also because of caking of the bed due to the hydrodynamic action of the flow at the quite high filtration rate (70–100 m/h).
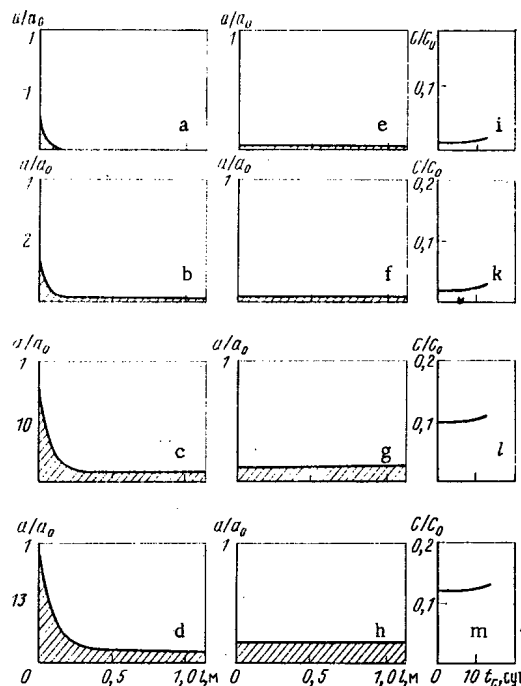
Fig. 1. Calculated distribution of sodium cations over the thickness of the cationite layer: a, b, c, and d) after adsorption before loosening; e, f, g, h) after loosening; i, k, l, and m) efficiency curves of sodium adsorption (the number of filtration cycles is shown on the left).
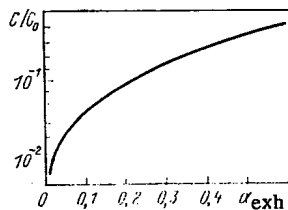

Fig. 2

Fig. 3

Fig. 2. Dependence of the condensate quality (intensity of purification) on the degree of exhaustion of the cationite.
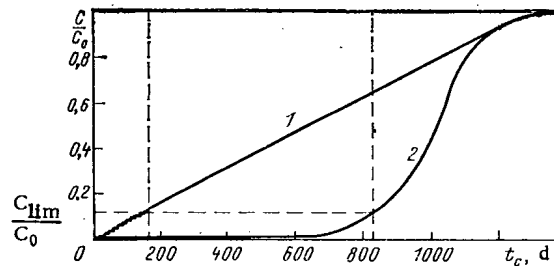
Fig. 3. Calculated efficiency curves of the adsorption of sodium cations on cationite KU-2-8: 1) loosening once in 14 days; 2) without loosening.

As the concentration of ion impurities in the condensate is small and the volume capacity of the bed is quite high, then the filtration cycle with respect to the ion component continues. On the other hand, the load capacity of the filter with respect to suspended particles is insignificant, and their main mass is retained by a "frontal" layer, which leads to an increase of the pressure differential. After attaining the limiting permissible value, loosening of the cationite is carried out. It restores the original filtration properties to the cationite. However, as a result of loosening, partial or total mixing of the ionite occurs, in consequence of which the partially spent cationite enters the lower levels of the filter, which leads to a change of distribution of the cations adsorbed in the solid phase of the ionite over the thickness of the bed. The concentration of these cations in the lower layer of ionite determines the quality of the filtrate at the outlet from the filter [2], which was confirmed experimentally during the operation of loosened H^+-cationite filters of nuclear power stations. Thus, the content of sodium in the condensate for a cationite filter in the case of adsorption over 10 days amounted to 0.5-1.5 μg/kg. After carrying out loosening of the cationite with subsequent adsorption, the concentration of sodium in the filtrate after the filter increased up to 4 μg/kg, which required the filter to be disconnected for

regeneration. The appearance of sodium in the filtrate with subsequent adsorption is caused by the displacement of sodium from the adjacent layers of cationite where it had entered during loosening.

Consideration of condensate purification as an adsorption system on the basis of the mathematical model of [2, 3] allows a calculation to be performed of the distribution of sodium over the thickness of the cationite bed and the quality of the filtrate to be determined before and after each loosening during a single filtration cycle. The purpose of the present paper is to study the quantitative characteristics of the process of sodium adsorption on cationite KU-2-8 in the case of interstitial loosening.

A calculation of the parameters of the condensate purification process with a salt content $C_0 = 1 \cdot 10^{-6}$ N for sodium purification conditions up to $C_{lim} = 1.2 \cdot 10^{-7}$ N (2.8 μg/kg) was performed for the following starting data, corresponding to the operating conditions of the H^+-filter in the condensate purification scheme:

Total exchange capacity of KU-2-8, mmole/ml	1.9
Ion exchange constant Na^+ by H^+	1.2
Equivalent grain diameter, mm	0.63
Filtration rate, m/h	80
Thickness of cationite charge in filter, cm	113
Cross section of filter, m^2	7

The cationite is loosened once per 14 days. Figure 1a shows the calculated distribution of sodium over the thickness of the cationite bed after adsorption over 14 days on completely regenerated cationite. The adsorbed sodium is found in the frontal layers of the cationite and does not affect the quality of the filtrate obtained. The area under the curve, characterizing the degree of exhaustion of the cationite, amounts to 1.18% of the total capacity of the cationite. As a result of loosening and with a filtration rate of 70 m/h, during 20 min according to the calculation the bed is almost completely ($\sim$98%) intermixed [4]. In consequence of this, the adsorbed sodium in the cationite after loosening is distributed uniformly over the thickness of the bed (Fig. 1, i). The average concentration of sodium in the cationite amounts to 0.022 mmole/ml. As the adsorption capacity is spent only insignificantly and, consequently, restoration of the regeneration capacity of the cationite is inexpedient, the filter is again switched into the purification process. Because of the displacement of the sodium ions from the cationite, their concentration in the filtrate during subsequent adsorption (during the second filtration cycle) is equal to $1 \cdot 10^{-8}$ N (see Fig. 1, i). Figure 1b shows the calculated distribution of sodium over the thickness of the cationite bed after adsorption of sodium during 28 days of which 14 days are by partially exhausted cationite (degree of exhaustion 2.36%). As a result of a second loosening, the cationite is found to be uniformly exhausted (Fig. 1f), with an average concentration of sodium in the cationite of 0.045 mmole/ml. During purification of the condensate over the next 14 days, the concentration of sodium ions in the filtrate becomes equal to $1.8 \cdot 10^{-8}$ N (Fig. 1, k). Figure 1 also shows the corresponding distributions of sodium in the bed and its concentration in the filtrate after the 10th and 13th filtration cycle (Fig. 1, c, g, and l, and Fig. 1, d, h, and m, respectively).

The calculation performed showed that purification of the condensate in the period between regenerations leads to partially exhausted cationite with a constant content of sodium over the thickness of the bed. This distribution can be characterized by the degree of exhaustion of the cationite (Fig. 2). In addition, if we start from the requirements on the quality of the purified condensate ($C_{lim} = 2.8 \mu$g/kg), then the minimum permissible values of the degree of exhaustion amount to 15% for an initial salt concentration of $C_0 = 1 \cdot 10^{-6}$ N and 2% for $C_0 = 1 \cdot 10^{-5}$ N, which corresponds to the thirteenth and second loosening carried out for the periodicity being considered. This means that after carrying out this cycle of loosenings, the concentration of sodium in the filtrate becomes higher than that passing through. The use of such cationite in the condensate purification scheme and with a separate charge of ionites is not possible without its regeneration, because of the nonfulfilment of the requirements on the quality of the purified condensate, which significantly reduces the duration of the filtration cycle.

The duration of the filtration cycle without carrying out loosenings amounts to 845, and with loosenings — 178 days (Fig. 3). For this, the working capacity of the cationite was used in the first case to 88 and in the second case to 12%, which indicates an inefficient utilization of the exchange capacity of the cationite used as the filtering material. Consequently, the process of interstitial loosening during the filtration cycle leads to a deterioration of the sorption properties of the cationite filter (the quality of the filtrate is reduced and the duration of the filtration cycle is reduced).

The efficiency of utilization of the cationite bed (as material for a mechanical filter) can be judged from the distribution of iron over the thickness of the bed before carrying out loosening. For beds with thickness

689

0-10, 10-20, 20-30, and 30-50 cm, the concentration of iron amounts to 4100, 2300, 430, and 70 mg/liter, respectively, but for beds with thickness 50-100 cm no iron ions were detected. In the H^+-cationite filter, the main fraction of the corrosion products occurs in the 20-30-cm layer; in the lower layers their quantity is small and approximately one-half of the bed generally does not participate in the filtration purification process of the condensate from corrosion products. This allows a conclusion to be drawn about the low efficiency of utilization of the entire cationite bed as the material of the mechanical filter, and about the fact that for the reestablishment of the filtration properties, it is advantageous to carry out loosening of only the upper part of the filter.

Thus, for the rational utilization of the cationite and for increasing the operating efficiency of the cationite filter in the condensate purification system, it is necessary to divide the functions of the filtering bed, so that one part of the cationite effects purification from corrosion products and the other part — the removal of salts from the condensate. This can be achieved in two ways: by the installation of an additional filter (the use of an inert material is possible) for purification from corrosion products, or by loosening only the upper part of the cationite filter during the filtration cycle, in proportion with the increase of the pressure differential in the upper part of the bed. Implementation of these recommendations will allow the operating efficiency of cationite filter in nuclear power station condensate purification systems to be increased, and thereby to determine the choice of a rational technological condensate purification scheme and the proportion of ionites in the filters.

LITERATURE CITED

1. L. A. Kul'skii, É. B. Strakhov, A. M. Voloshina, and V. A. Bliznyukova, Purification of Water from Nuclear Power Stations [in Russian], Naukova Dumka, Kiev (1979), pp. 158-162.
2. M. M. Senyavin, R. N. Rubinshtein, E. V. Venitsianov, et al., Calculation Fundamentals and Optimization of Ion-Exchange Processes, [in Russian], Nauka, Moscow (1972), pp. 175, 127.
3. M. M. Senyavin, R. N. Rubinshtein, I. V. Komarova, et al., Theoretical Principles of Demineralization of Fresh Water [in Russian], Nauka, Moscow (1975), pp. 128-132.
4. I. V. Komarova, M. M. Senyavin, A. S. Sobol', et al., "Characteristics of the mathematical description of industrial ion-exchange filters," in: Proceedings of the Third National Conference "Water Treatment, Water Cycle and Corrosion at Thermal and Nuclear Power Stations" [in Russian], Varna (1976), pp. 265-271.

USE OF A MATHEMATICAL MODEL FOR DESCRIBING THE CONDENSATE PURIFICATION PROCESS, FOR THE PURPOSE OF SELECTING THE OPTIMUM RATIOS OF IONITES IN NUCLEAR POWER STATIONS

M. A. Argin, I. V. Komarova, N. K. Galkina, I. M. Zakova, and N. K. Kolotilina

UDC 541.183

The special feature of the condensate purification process at nuclear power stations consists in that the adsorption of cations on KU-2-8 cationite, and anions on AV-17-8 anionite, takes place from strongly diluted solutions of salts ($C_0 = 10^{-5}$-10^{-6} N). Analysis of the ion component of the condensate impurity showed that it consists mainly of Na^+ and Cl^-. Data about the ion–exchange mechanism of Na^+ and Cl^- on the ionites used in nuclear power stations from solutions with a salt content of $C_0 = 1 \cdot 10^{-4}$ N are contradictory [1], and for more dilute solutions they are lacking altogether. In this paper, the extrinsic diffusion mechanism of ion exchange is verified for the adsorption of Na^+ by strongly acid cationite KU-2-8 and Cl^- on highly basic anionite AV-17-8 from a solution of NaCl, $C_0 = 2 \cdot 10^{-5}$ N, and the adsorption purification of the condensate is described mathematically.

It is well known that ion–exchange in columns is described by a system of equations, in which the equations of balance and diffusion occur, and also the adsorption isotherms. The theory of single–component dynamics of adsorption in the extrinsic diffusion region has been well developed [1]. The admissibility of the use of these developments for describing adsorption purification in equipments of different sizes and at different flow rates is shown in [2].

The starting data shown in Table 1 formed the basis of the calculation of the theoretical efficiency curves of the adsorption of the ions being considered.

The single–component dynamics of adsorption in the region of extrinsic diffucion kinetics is described by the system of equations:

$$\frac{\partial U}{\partial X} = -\frac{\partial V}{\partial T};$$

$$\frac{\partial V}{\partial T} = U - f(V); \quad f(V) = F(a)/C_0,$$

where $U = C/C_0$ and $V = a/a_0$ are the relative concentrations of ions in solution and in the sorbent, respectively; $X = \beta l/v$, dimensionless thickness of the ionite charge; $T = \beta t C_0/a_0$, dimensionless time; $\beta = 0.009 \omega v^{0.5}/d^{1.5}$, transfer coefficient per unit volume of ionite; ω, kinetic mass–transfer coefficient; the solution of this system of equations with initial conditions $U(0, T) = 1$ and boundary conditions $V(X, 0) = 0$ is performed by a numerical method on the computer, using the method of characteristics [3]. The solution is represented in the form of dimensionless efficiency curves of C/C_0 and a/a_0 as functions of the dimensionless parameters X and T for a specified ion–exchange constant (Fig. 1). The exchange constant of Na^+ by hydrogen on cationite KU-2-8 is equal to 1.2. In the case of adsorption of H^+–cationized water on anionite AV-17-8, exchange is accompanied by neutralization reactions, and equilibrium is characterized by the effective exchange coefficient (for exchange of Cl^- by OH^-, $K_0 > 10$); therefore, the exchange isotherm can be assumed to be rectangular [1].

The conditions for conducting the experiment were chosen in such a way as to ensure the feasibility of the experimental determination in the original solution and filtrate of the concentration of ions being studied.

The curves for the adsorption of Na^+ on cationite KU-2-8, and Cl^- on anionite AV-17-8 from a model solution of NaCl, were obtained by conducting experiments on a special test-rig (Fig. 2), which allows continuity and constancy of the feed rate of the solution with a given concentration to be implemented, and continuous monitoring of the concentrations of these ions in the original solution and in the filtrate to be conducted. The

691

TABLE 1. Starting Data for Calculation and Experiment

Parameter	Cationite KU-2-8	Anionite AV-17-8
Total exchange capacity of ionite a_0, mmole/ml	1,9	0,86
Concen. of ions C_0, mmole/ml	$2 \cdot 10^{-5}$	$2 \cdot 10^{-5}$
Ion-exchange constant K_0	1,2	10
Thickness of ionite charge l, cm	5,0	9,4
Cross section of column S, cm^2	1,56	1,56
Ionite grain diameter d, cm	0,062	0,063
Filtration rate v, cm/sec	3,98	3,98
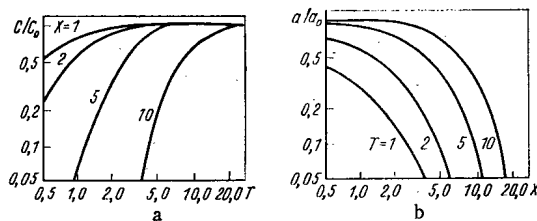
Fig. 1. Solution of the system of equations of the frontal dynamics of adsorption in the case of extrinsic diffusion kinetics, and $K_0 = 1.2$; a) dimensionless concentration in solution; b) dimensionless concentration in the sorbent.
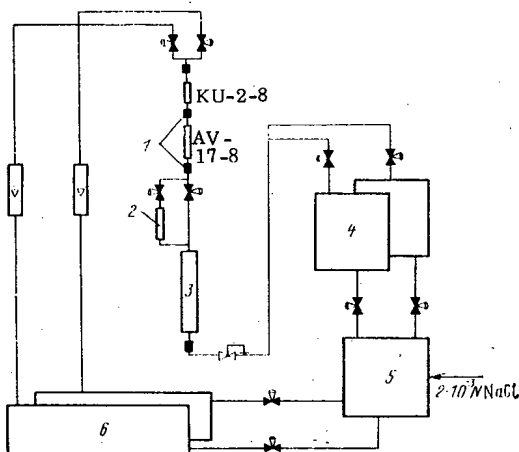
Fig. 2. Circuit diagram of the automated test-rig: 1) electrical conductivity measurement sensor; 2) concentrator; 3) mixed bed; 4) reservoir for water collection; 5) reservoir for preparation of the starting solution; 6) reservoirs with starting solution.
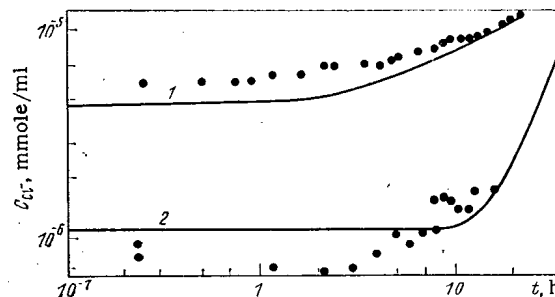
Fig. 3. Efficiency curves of sodium (1) and chlorine (2); ———) calculation, ●) experiment.

test-rig consists of two reservoirs with the original solution, a system of successively joined columns, concentrator column, flow sensors for measurement of the electrical conductivity of the solution passing through, a column with a mixed layer of ionites for the final purification of the filtrate (after adsorption of the ions on KU-2-8 and AV-17-8) for the purpose of the repeated use of the solution, two reservoirs for collection of the desalinated water, and a reservoir for the preparation of the model solution by dosing in a solution of NaCl (concentration $2 \cdot 10^{-3}$ N). The model solution was passed through the closed circuit, creating an excess pressure of the inert gas in the reservoir with the starting solution. This allows a uniform feed rate of the solution

692

to be organized during the experiment and the supply of the solution being passed to be regulated by a change of this pressure. In addition, the constancy of supply of the solution was maintained by means of a pneumatic system of a "pressure regulator." Continuous operation of the test-rig was effected by the automatic change-over of the flows from the starting solution reservoirs by means of electropneumatic valves.

Monitoring of the composition of the starting solution and filtrate was effected by a conductimetric method, using the four-channel IÉZhK-VI conductometer and thermoresistances for measuring the temperature of the solution. In addition, in order to determine the amount of Na^+, a pNa-meter was used, and to determine the amount of Cl^- its ion-exchange concentration on anionite AV-17-8 in NO_3-form was used, with subsequent washing of the chloride with a 1 N solution of $NaNO_3$ and determination of the chloride-ion in the concentrate by a nephelometric method.

The adsorption efficiency curves obtained are shown in Fig. 3. At the start of the efficiency curves, there is an "instantaneous throughput," which appears in the form of a step. From the theory of the dynamics of ion-exchange adsorption, it is known that with a sufficiently small length of the sorbent layer and a high rate of throughput of the solution, in this way only the extrinsic diffusion efficiency curves are characterized. For the extrinsic diffusion mechanism of kinetics, the instantaneous throughput is described by the ratio $C_{lim}/C_0 = e^{-X}$ [2]. According to calculation, for Na^+ it amounted to $4.5 \cdot 10^{-6}$ N and for Cl^- to $1.1 \cdot 10^{-6}$ N. The experimental efficiency curves coincide satisfactorily with the calculated curves, but the spread of the experimental values is related mainly with the measurement accuracy of small concentrations of ions by the conductimetric method.

It follows from the results obtained that in order to describe the process of adsorption of Na^+ on cationite KU-2-8 and Cl^- on anionite AV-17-8 from a $2 \cdot 10^{-5}$ N solution of sodium chloride, a mathematical model is used for the adsorption of the ion least adsorbed in the extrinsic kinetic region. The adequacy of the adsorption process with the mathematical model enables the condensate purification process for nuclear power stations to be calculated for realistic conditions, and the optimum ratios of KU-2-8 and AV-17-8 in separate and mixed ionite beds to be found.

LITERATURE CITED

1. M. M. Senyavin, R. N. Rubinshtein, I. V. Komarova, et al., Theoretical Principles of the Demineralization of Fresh Water [in Russian], Nauka, Moscow (1975).
2. M. M. Senyavin, R. N. Rubinshtein, E. V. Venitsianov, et al., Principles of the Calculation and Optimization of Ion-Exchange Processes [in Russian], Nauka, Moscow (1972).
3. N. S. Berezin and N. P. Zhidkov, Methods of Calculations [in Russian], Vol. 2, Fizmatgiz, Moscow (1962).
4. V. P. Tomoshenko, I. Ya. Shtral', Yu. M. Luzhkov, and M. G. Slin'ko, "Automated system for scientific investigations in the field of catalysis," Khim. Promyshlennost', No. 3, 172-177 (1979).

TESTS OF A U$_3$O$_8$ TUBULAR FEEDER

V. A. Zuev, A. A. Kryuchkov,
Yu. A. Repkin, S. F. Romanov,
and A. I. Tselikovskaya

UDC 669.02/09:546.791

Batching operations of friable materials are an important component part of the technological processes of uranium production [1-3]. In chemical technology, belt, screw conveyor, disk and vibration feeders usually are used for bulk batching. However, they all have drawbacks related first and foremost with instability of the friable material feed. In particular, in screw conveyor feeders, nonuniformity of the feed (error) can attain 30% and more.

In tubular feeders [5-6], the principal transportation element is a horizontal or inclined rotating tube. During movement through it, the friable material is repeatedly mixed, as a result of which its bulk density is stabilized and the batching uniformity is increased. By comparison with screw conveyors, the feed in tubular feeders is more stable and the batching error of different materials fluctuates from 1 to 1.5 up to 3-5%. These feeders are used particularly advantageously in the case of small flow rates [5-6].

This paper is devoted to tests of a tubular feeder (Fig. 1) for the purpose of assessing the prospects for its utilization for batching uranium-containing materials. After loading U$_3$O$_8$ powder in the drum 1, served by a hopper, the electric motor 4 was switched on, which through a mechanical transmission system 5 set the drum into rotation and also the transporting tube 6, mounted on ball bearings in the housing 3. On rotation, the powder first of all entered the distribution device of the "squirrel cage" type 2, and then passed into the collecting hopper and the transporting tube. From the transporting tube the powder poured through the funnel of the mixing chamber 7 into a glass flask, installed on the VLTK-500 balance, which allowed continuous monitoring of the change of mass of the friable product with time. The output of the feeder was regulated manually by changing the angle of inclination of the tube to the horizontal axis by means of the coupling 8. For this purpose, proviso is made for rotation of the feeder relative to the hinge 9. The feed rate of friable product with the tubular feeder depends on the diameter of the tube, its frequency of rotation, and the angle of inclination to the level line [5-6].

The granulometric composition of the starting U$_3$O$_8$ is as follows: for particles with diameter < 50, 50-63, 63-100, 100-160, 160-200, 200-250, 250-315, and > 315 μm, the mass percentage of the fractions amounts to 7.3, 11.3, 26.8, 14.0, 17.3, 11.0, 5.6, and 6.2%, respectively. The picnometric density is 6.7-7.2 g/cm^3, specific volume (measurement by Deryagin's method) 0.55-0.65 m^2/g. The flow coefficient (k=tr$^{2.58}$/G), angle of natural inclination α, and the poured mass are given in Table 1.

The critical operating parameters of the tubular feeder, for which there is no feed of the friable product, were determined by the following formulas:

critical frequency of rotation of the tube, sec^{-1}

$$n_{cr,\tau} = \frac{1}{2\pi} \sqrt{2g/d},$$

TABLE 1. Characteristics of the Starting Product and Individual Fractions

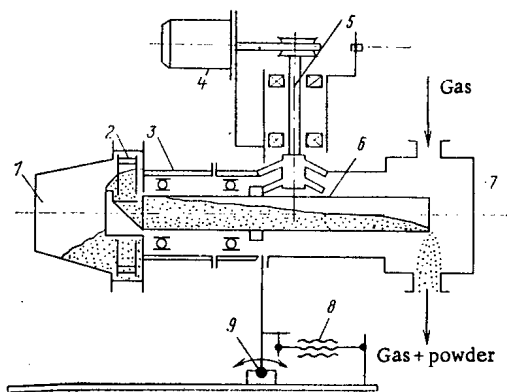| Characteristic	Starting product	Particle size, μm					
		50—63	63—100	100—160	160—200	200—250	250—315
k	Discharge not observed	—	—	2,7	2,00	1,77	1,78
α	43°30'	50°30'	50°50'	37°30'	36°50'	35°10'	34°30'
Poured mass, g/cm^3	1,9—2,0	1,6	1,83	2,05	2,18	2,41	2,50

Fig. 1. General view of the tubular feeder.

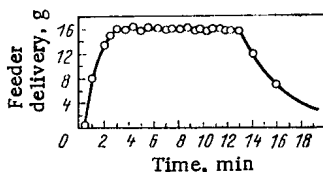
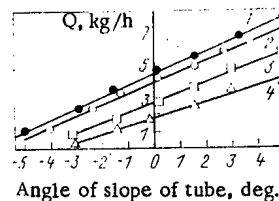Fig. 2. Change of feeder delivery with time (angle of inclination 0°).

Fig. 3. Dependence of the feeder delivery Q on the angle of inclination of the tube β and the particle size of the U_3O_8: 1) 100-160 μm; 2) starting product (angle of inclination 0°); 3) 63-100μm; 4) 50-63 μm.

where d is the tube diameter, cm; g = 9.81 m/sec^2 is the acceleration of gravity;

critical frequency of rotation of the drum, sec^{-1}:

$$n_{cr.Dr} = \frac{1}{2\pi}\sqrt{2g/D},$$

where D is the diameter of the drum, cm;

critical angle of inclination of the tube:

$$\beta_{cr} = \text{arctg}\,\frac{d}{L},$$

where d is the diameter of the tube, cm; L is the length of the tube, cm.

Delivery of the product is most stable when the frequency of rotation of the tube $n_T = (0.1-0.5)n_{cr.T}$, L = (6-10)d and the frequency of rotation of the drum $n_{Dr} = (0.6-0.7)n_{cr.Dr}$. For the given feeder, d = 2 cm, D = 15 cm, L = 19.4 cm, $n_{cr.T}$ = 300 min^{-1}, $n_{cr.Dr}$ = 109 min^{-1}, and β_{cr} = −6°. The tests of the feeder were carried out with the following: $n_T = n_{Dr}$ = 60 min^{-1}, the U_3O_8 charge was 500 g and the measurement interval was 15 sec.

The effect of the angle of inclination of the tube and the particle size of the U_3O_8 on the feeder delivery was investigated (Fig. 2).

Processing of the experimental data was carried out for the section of stable delivery of the feeder. The calculation of the measurement errors was performed by the procedure explained in [8]. The total results are shown in Fig. 3. The dependence of the feeder delivery on the angle of inclination of the transporting tube for all fractions of U_3O_8 studied, with an accuracy from ± 1.1 to ± 1.8%, can be described by the linear equation $Q = a + b\beta$, where a and b are constant coefficients.

The results of the tests showed that the tubular feeder allows batching of the U_3O_8 with sufficiently high accuracy. Thus, for the starting product, the granulometric composition of which is given above, the relative error amounted to ± 0.9 to ± 2.5%. The feeder delivery was increased with increase of the particle size of the U_3O_8. The batching accuracy decreased with reduction of the particle size and with increase of the elevation of

695

the tube (sign of the angle negative). The critical angle of inclination depended on the particle size. The batching accuracy of the starting product and of the fraction with a particle size of 100–160 μm was satisfactory for all the investigations, for angles of inclination from -5 to $+5°$. The delivery of smaller sized particles (50–63 and 63–100 μm) ceased at $-5°$. For particles with a size of 50–63 μm, lumping of the product was observed with the tube elevation angle of $-3°$, and the batching accuracy was reduced to $\pm 5.4\%$. The tests showed the feasibility of delivering U_3O_8 powders with poor consistency with inclination of the tube, with the assurance of quite high accuracy (from ± 1.0 to 2.5%).

Thus, the tests of the tubular feeder carried out have shown the prospects for the chosen design. Even for materials with poor consistency, the batching accuracy amounted to $\pm 5\%$ in the case of a measurement interval of 15 sec. The feeder delivery was regulated over wide limits from 1–7.7 kg/h with a batching accuracy from 1.0 to 2.5% with variation of the angle of inclination of the transporting tube. The design of the feeder was calculated on the periodic charging of the product, and therefore with a charge in the bunker of 500 g of U_3O_8, the duration of stable delivery was short and, depending on the angle of inclination of the tube and the particle size of the starting material, amounted to 3–15 min. Extension of the section of stable delivery of the feeder is possible with increase of the volume of the bunker and with continuous charging of the product. In these conditions, a stable delivery of a friable product can be maintained during the required time interval and within the limits of permissible accuracy.

LITERATURE CITED

1. N. P. Galkin and V. B. Tikhomirov, Principal Processes and Equipments of Uranium Technology [in Russian], Gosatomizdat, Moscow (1961).
2. S. Smaili, Equipment Design of Heterogeneous Processes in Uranium Technology [in Russian], Gosatomizdat, Moscow (1963).
3. B. N. Sudarikov and É. G. Rakov, Processes and Equipments of Uranium Production [in Russian], Mashinostroenie, Moscow (1969).
4. G. A. Reginskii, Batching of Friable Materials [in Russian], Khimiya, Moscow (1978).
5. Yu. A. Repkin and V. M. Mikhalin, "Tubular feeders," Khim. Neft. Mashinostr., No. 3, 44 (1975).
6. Yu. A. Repkin and A. I. Tselikovskaya, Tubular Microfeeders — High-Speed Information [in Russian], TsINTIKhIMNEFTEMASh, Series KhM-1, No. 11 (1979).
7. Yu. I. Makarov, Equipments for Mixing Friable Materials [in Russian], Mashinostroenie, Moscow (1973).
8. A. N. Zaidel', Elementary Estimates of Measurement Errors [in Russian], Nauka, Moscow (1968).

EFFECT OF HIGH-POWER GAMMA-RADIATION ON THE ^{90}Sr DISTRIBUTION IN THE GROUND

I. A. Sobolev, L. M. Khomchik,
E. M. Timofeev, A. S. Barinov,
and M. I. Ozhovan

UDC 621.329.714

The final stage in processing radioactive waste is its burial in the ground in special storage facilities of various design [1, 2]. In order to estimate the reliability of such burial, it is necessary to predict the possibility of change in the characteristics of the ground surrounding the storage facility as a result of exposure to ionizing radiation. Since the time of waste storage is measured in hundreds or thousands of years, the doses absorbed by the ground may be considerable, even for waste of moderate specific activity. In order to predict changes in the ground properties, it is obviously necessary to determine the irradiation parameters of decisive importance for changes in the physicochemical characteristics of the ground.

The present article is concerned with the effect of gamma-radiation on the ^{90}Sr distribution in argillaceous soil. As is known, the distribution coefficient is actually the determining quantity in estimating radionuclide migration in grounds.

In our experiments, we used specimens of heavy moraine loam containing up to 30% argillaceous particles with sizes of less than 1 μm, represented by kaolinite, montmorillonite, and hydromica. The density of the ground was equal to 2.68 g/cm^3, the exchange capacity amounted to 0.321 mole/kg, while the humus percentage did not exceed 0.3%. The ground composition comprised the following cations: 65 Ca^{2+}, 15.7 Na$^+$, 11.2 Mg^{2+}, and 8.1 K$^+$. Air-dry ground samples were ground in a porcelain mortar and screened through a sieve with 0.25 mm mesh. Samples with a mass of 70 g were taken from the fraction that had passed through the sieve and were placed in the lateral channel of the RKhM-γ-20 irradiation device with cobalt (^{60}Co) gamma-radiators. The absorbed dose rate varied in the range from 1.2·10^3 to 2.2·10^5 rd/h (3.3×10^{-3}–6.1·10^{-1} Gy/sec), while the integral absorbed dose varied from 10^3 to 2.3·10^8 rd (from 10 to 2.3·10^6 Gy). The temperature in the channel of the irradiation device was equal to 40 ± 5°C.

For the irradiated argillaceous ground specimens, we investigated the ion–exchange capacity (using the Grabarov–Uvarova method based on Ba^{2+} sorption [3]) and the ^{90}Sr distribution coefficient (ratio of the ^{90}Sr concentration in the solid phase to the ^{90}Sr concentration in the contacting equilibrium solution [4]). The determination was performed under static conditions with respect to several parallel specimens from a nitrate solution of ^{90}Sr in distilled water with a specific radioactivity of 3.7·10^4 Bq/liter. The solution-to-sorbent mass ratio was equal to 20/1. The measurement error was less than 14%.

The investigation of the irradiated ground samples has shown that the ion-exchange capacity remains virtually unchanged up to a total dose of 2.3·10^8 rd (which agrees with the earlier data [5, 6]) in the range of dose rates $P_D = 10^3$–2·10^5 rd/h (2.8·10^{-3}–5.6·10^{-1} Gy/sec).

TABLE 1. Dependence of the ^{90}Sr distribution in Argillaceous Ground on the Irradiation Conditions

$P_D = \text{const} = 2.2 \cdot 10^5$ rd/h ($6.1 \cdot 10^{-1}$ Gy/sec)		$D = \text{const} = 10^6$ rd (10^4 Gy)	
D, rd (Gy)	K_d	P_D, rd/h (Gy/sec)	K_d
0	819	0	819
10^3 (10)	1073		—
10^4 (10^2)	998	2,2·10^5 (6,1·10^{-1})	491
10^5 (10^3)	575	4,5·10^4 (1,3·10^{-1})	513
10^6 (10^4)	491	2,2·10^4 (6,1·10^{-2})	593
10^7 (10^5)	633	4,3·10^3 (1,2·10^{-2})	458
10^8 (10^6)	439	1,2·10^3 (3,3·10^{-3})	294

The effect of gamma-radiation on the ^{90}Sr distribution coefficient was investigated in two series of experiments. In the first series, the specimens were irradiated with doses of 10^3 to 10^8 rd (from 10 to 10^6 Gy) at a constant dose rate of $2.2 \cdot 10^5$ rd/h ($6.1 \cdot 10^{-1}$ Gy/h). In the dose range of up to 10^5 rd (10^3 Gy), we observed a slight increase in K_d, after which this value diminished by a large factor as the absorbed dose increased.

The dose of irradiation of ground specimens was constant in the second series of experiments and amounted to 10^6 rd (10^4 Gy) with the dose rate varying from $1.3 \cdot 10^3$ to $2.2 \cdot 10^5$ rd/h (from $3.6 \cdot 10^3$ to $6.1 \cdot 10^{-1}$ Gy/sec). In this case, the distribution coefficient diminished with a reduction in the gamma-radiation dose rate.

The experimental results (see Table 1) indicate that the K_d value is affected by both the integral dose and the dose rate. In connection with this, it does not seem always justified to predict the change in systems of complex composition (such as, for instance, ground sediments) solely with respect to the results of their short-term irradiation with large doses. In order to estimate the results of radiation action, it is evidently necessary to perform sufficiently long irradiation of specimens in a wide range of dose rates.

Changes in the sorption properties of grounds caused by irradiation are primarily connected with changes in the surface layers [5-8] and, as a consequence, with changes in the kinetic parameters of the interphase distribution of sorbed ions.

Thus, while the ion-exchange capacity of argillaceous ground remains unchanged for total irradiation doses $\lesssim 10^8$ rd (10^6 Gy), the ^{90}Sr distribution coefficient undergoes changes depending to a great extent on the irradiation dose rate.

LITERATURE CITED

1. A. S. Nikiforov, A. S. Polyakov, and K. P. Zakharova, "Processing and solidification of radioactive waste from atomic electric power stations," At. Energ., 55, No. 6, 368-370 (1983).
2. I. A. Sobolev and L. M. Khomchik, Rendering Radioactive Waste Harmless at Centralized Locations [in Russian], Énergoatomizdat, Moscow (1983).
3. A. S. Belitskii and E. I. Orlova, Protection of Underground Water from Radioactive Contamination [in Russian], Meditsina, Moscow (1968).
4. Methodic Manual of Geological-Engineering Investigation of Rocks [in Russian], Vol. 2, Moscow State University (1968).
5. V. S. Spitsyn, V. Balukova, I. Kosareva, and S. Kabakchi, in: Scientific Basis for Nuclear Waste Management, Vol. 3, Plenum Press, New York–London (1981), p. 429.
6. V. Spitsyn, V. Balukova, and M. Savushkina, in: Scientific Basis for Nuclear Waste Management, Vol. 6, Plenum Press, New York–London (1982), p. 703.
7. I. A. Sobolev, L. M. Khomchik, E. M. Timofeev, et al., "Radiation-induced structural changes in heterogeneous dispersed systems," Inzh.-Fiz. Zh., 46, 692 (1984).
8. I. A. Sobolev, L. M. Khomchik, E. M. Timofeev, et al., "Diffusion instability of the surface of solids," Poverkhnost', No. 12, 32-37 (1984).

EFFECT OF RADIATION ON THE OPTICAL
CHARACTERISTICS OF QUARTZ GLASS

I. Kh. Abdukadyrova

UDC 535.342 : 666.192

This is a continuation of the investigation of the effect of radiation on the optical spectra of quartz glasses that had been started earlier [1]. We investigated gas-fused KV glass and KSP plasma glass (in many cases, we also used other types of glass, KSG, KU, and KI, for radiation resistance comparisons), which were exposed to different sets of doses D of ^{60}Co gamma-radiation (from 1 to 10^8 Gy). We recorded before and after irradiation the spectra of optical absorption in the visible region of the spectrum at wavelengths $\lambda = 450-700$ nm and of photoluminescence (PL) at $\lambda = 396.284$ nm [2].

Figure 1 shows the variation of the reduced optical density E/d (E is the induced optical density, and d is the specimen's thickness) at the maximum of the 540-nm absorption band with increasing D values. It is evident from the diagram that the dose dependence of the degree of blackening of KV and KSP glasses is characterized by proportional growth up to $D = 10^6$ Gy. The curve subsequently reaches a saturation plateau for $D > 10^6$ Gy. It is evident that the curves $(E/d)_{540} = f(D)$ do not have an inflection in the $D > (1-5)10^5$ Gy range, which has been found in similar dependences for the UV-band (215 nm) in these glasses as well as in KSG and KU glasses and is probably connected with the development of additional structure defects (up to 10^7 Gy).

We monitored in our investigations the stability of the visible tint induced by ionizing radiation after the irradiation of quartz glass was discontinued. According to our results (Table 1), the posteffect over a period of 1000 h amounts to ~6-10% (after further refinements for long-duration detector exposures, it will probably be possible to introduce a suitable correction).

The effect of daylight was also studied. For this purpose, KSP plates were placed in an illuminated location, and changes in the initial optical density were systematically monitored. Good stability of the induced tint was observed. The effect of light of greater intensity was determined by illuminating the specimens with unfiltered light from a mercury-vapor lamp. The irradiation time was equal to 0.2-2 h. It has been established that the tint is stable with respect to the action of a wide spectrum of the lamp's radiation. All this makes it possible to perform repeated optical density measurements for irradiated glass kept under different storage conditions. The effect of irradiation conditions was investigated on KSP plates with a thickness of 1 mm. Variation of the radiation dose rate within the 0.2-40 Gy/sec range at processing temperatures of up to 200-250°C show an absence of noticeable effect on the system's responses. As in the case of KI glass [1], the plates are completely discolored by short-term heating to 450-500 deg C, which makes the system suitable for repeated use.

The photoluminescence method, which is the most sensitive one, was used for elaborating recommendations on the development of glass detectors in the range of small radiation doses. The well-known phenomenon

TABLE 1. Stability of the Induced Tint in Various Glasses at the Maximum of the 540-nm Absorption Band for Different Exposure Times (irradiation dose, $2 \cdot 10^6$ Gy)

Glass type	d, mm	Exposure time, h					
		1	5	10	25	100	1000
KSP	1,0	0,53	0,54	0,51	0,53	0,51	0,50
	1,6	0,79	0,81	0,81	0,82	0,78	0,76
KV	0,6	0,34	0,34	0,36	0,36	0,32	0,29
	1,1	0,64	0,59	0,61	0,66	0,60	0,57
	3,5	1,87	1,81	1,89	1,77	1,82	1,77

TABLE 2. Photoluminescence Intensity I of KV Quartz Glass (irradiation dose, 10^2 Gy) in Relation to Changes in the External Conditions A_i

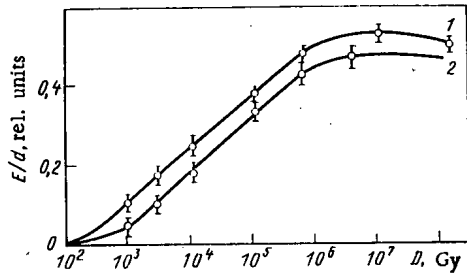| A_1, Gy/sec	I_1, rel. units	A_2, °C	I_2, rel. units	A_3, h	I_3, rel. units
0,2	70	31	68	0,5	68
0,4	69	70	68	2,0	68
6,5	68	90	69	5,5	68
17,0	69	140	70	25,0	71
23,0	68	160	72	52,5	70

 699

Fig. 1. Reduced optical density at the 540-nm absorption band for KSP (1) and KV (2) glasses.
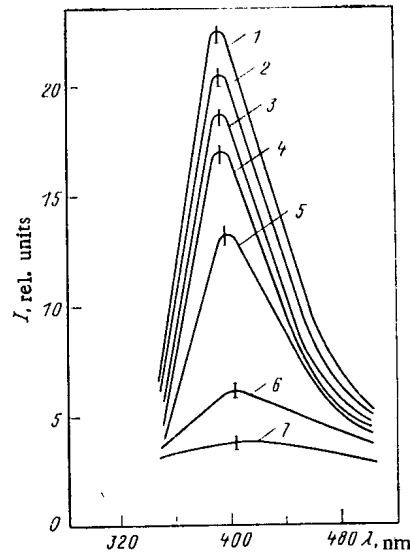

Fig. 2. Effect of the gamma-radiation dose on the photoluminescence spectrum of KV in the $\lambda = 350$–500 nm range. 1) Un-irradiated specimen; 2) irradiation dose, 10^0 Gy; 3) 10^1 Gy; 4) 10^2 Gy; 5) 10^3 Gy; 6) 10^4 Gy; 7) 10^5 Gy.

of radiation-induced reduction in the luminescence intensity I at the 396-nm band maximum was used as the working parameter. The monotonic decrease in the luminescence intensity found for the set of glasses indicates the presence of a sufficient number of the preradiation structure defects responsible for photoluminescence, the filling of which by charge carriers varies during the irradiation process. It was found that the slope of the function $I = f(D)$ is determined by the type of glass, which may be due to a particular previous history of the material and also the effect of controllable impurities.

The strongest luminescence degradation effect was observed in the case of KV glass (Fig. 2). As the gamma-radiation dose is varied within the range $I < D < 10^5$ Gy, the luminescence intensity gradually decreases, and, for $D > 10^5$ Gy, luminescence in the glass virtually ceases at $\lambda = 396$ nm. On the other hand, for $D > 7 \cdot 10^5$ Gy, we found the induction in KSG of one of the two PL bands (~ 290 nm), where I varies as D increases. This, together with an allowance for the above-mentioned increase in the rate of buildup of the tint center in the UV-region of the spectrum, provides an indication that oxygen vacancies are produced in the lattice by radiation.

We investigated the effect of the radiation dose rate (A_1), the temperature of the ^{60}Co source channel in the irradiation zone (A_2), and the exposure time of specimens (A_3), on the luminescence characteristics of ir-radiated glass. It was found (Table 2) that, within the range under consideration, the error in measuring the spectroscopic signal amounts to ~ 3–5% (this satisfies the requirements imposed on dosimetric systems; how-ever, in order to improve the data accuracy in detailed investigations, this factor may be taken into account).

On the basis of the results obtained, we concluded that it is advisable to use the phenomena of lumines-cence degradation for KV glass for practical problems (detection of very small absorbed energy values), that the initial UV-luminescence vanishes during suitable radiation processing of glass, and that the transparency of the material in the UV- and the visible regions of the spectrum deteriorates.

There is still no unanimity of opinion concerning the nature of the 396-nm luminescence band in quartz glasses. Some authors [5, 6] consider that a structure defect, for instance, an oxygen deficit, is the cause of this luminescence, while others relate it to the presence of impurities [7, 8]. If one accepts the latter, the luminescence in question is then probably due to the presence of uncontrollable impurities of metal ions in KV glass. Then, in order to reduce the error in measuring the absorbed dose on the basis of the monotonic de-crease in the intensity of the 396-nm band, it would be necessary first to produce a calibration graph of the optical signal for a control specimen as a function of the gamma-radiation dose for each glass batch.

Thus, the results of comparative investigations of the effect of ^{60}Co gamma-radiation on the optical prop-erties of quartz glasses and careful determination of the effect of all kinds of external factors on their charac-teristics provided a basis for recommending KSP and KV quartz glasses as solid dosimeters of gamma-radia-

tion in a wide range of absorbed doses, from 1 to 10^7 Gy. At the first stage ($D = 1-10^5$ Gy), it is advisable to use the luminescence degradation phenomenon (KV quartz glass; operating wavelength, 396 nm; cell dimensions, $10 \times 10 \times 2$ mm), and, at the second stage ($D = 10^3-10^6$ Gy), the proportional increase in optical density at $\lambda = 540$ nm (KSP and KV quartz glasses with dimensions of $10 \times 10 \times 2$ (3) mm). For $D \leq 10^7$ Gy and $\lambda = 215$ nm, it is recommended to use KSP, KV, KSG, and KU glasses with the size $10 \times 10 \times 1$(2) mm.

LITERATURE CITED

1. I. Kh. Abdukadyrova, "Colorimetric dosimeter of γ radiation," At. Energ., 49, No. 2, 135-136 (1980).
2. G. V. Byurganovskaya, V. V. Vargin, N. A. Leko, and N. F. Orlov, Effect of Radiation on Inorganic Glasses [in Russian], Atomizdat, Moscow (1968).
3. N. K. Gusakova and R. V. Lebedeva, New Inorganic Materials and Coatings Based on Glass and High-Melting Compounds [in Russian], Moscow (1973), p. 19.
4. S. M. Brekhovskikh, Yu. N. Viktorova, and L. M. Landa, Radiation Effects in Glasses [in Russian], Énergoizdat, Moscow (1982), p. 184.
5. V. Garino-Canina, Verres et Refract., 10, 63 (1956).
6. R. Jokota, J. Phys. Soc. Jpn., 7, 316 (1952).
7. D. M. Yudin, "Determination of the type of radiation traps in glasses," Phys. Tverd. Tela, 7, No. 6, 1733-1738 (1965).
8. A. V. Amosov, "Fine structure of the 4.4-eV luminescence band in quartz glasses," Fiz. Khim. Stekla, 5, No. 5, 624-626 (1979).

RADIATION STABILITY OF CORUNDUM CERAMIC
WITH PULSED IRRADIATION BY FAST NEUTRONS

O. B. Alekseevskii, S. A. Vorob'ev,
R. G. Ziyakaev, and V. V. Mameev

Ceramic dielectrics are promising electrical insulating materials for thermonuclear power generation, which explains the interest towards changes of their microstructure and electrophysical properties in conditions of intense radiation action. Measurements of the conductivity of ceramic materials under neutron irradiation in nuclear reactors [1-3] do not allow the effect of the neutrons on the conductivity of the materials to be assessed accurately because of the accompanying γ radiation. The appearance of accelerators, generating intense neutron fluxes with high energy, has made it possible to investigate the action of pulsed neutron radiation on the conductivity of corundum ceramic.

The calculation of the number of displaced atoms was performed by taking account of elastic and inelastic scattering of neutrons with 14-MeV energy. When considering elastic scattering, the well-known energy distributions of the initially knocked-out atoms were used. For inelastic scattering, the method of calculating the distributions was used, based on the statistical theory of multiple processes and the results of experiments on the investigation of the inelastic scattering of nucleons by nuclei. In the assumed model, excitation of the residual nucleus is removed by cascade emission of γ-quanta. Calculation of the characteristics of the system, consisting of a recoil nucleus, scattered neutron and k emitted γ-quanta, is reduced to the calculation of the phase volumes [4]. The expression obtained for the energy distribution of the initially knocked-out atoms in the laboratory system of coordinates has the form

$$W(E) = \frac{4\pi}{E_m \lambda(k)} \sum_{i=0}^{2k-1} \frac{C(i, k)}{i+1} [1 - (1 - 2\sqrt{E/E_m})^{2(i+1)}],$$

where E_m is the maximum energy of the initially knocked-out atom;

$$\lambda(k) = \sum_{i=0}^{2k-1} \frac{2C(i, k)}{2i+3}; \quad C(i, k) = (-1)^i \binom{2k-1}{i}.$$
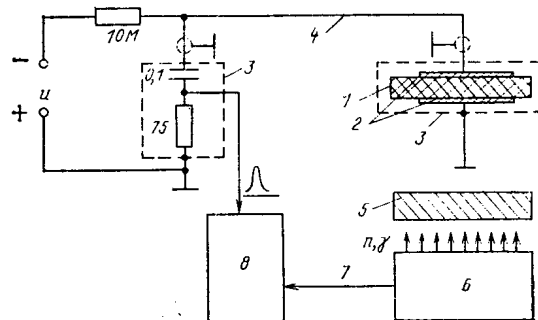
701

Fig. 1. Measurement circuit of pulsed radiation conductivity: 1) sample; 2) electrodes; 3) screen; 4) high-frequency cable; 5) lead shield; 6) accelerator; 7) signal for triggering the oscillograph scanning; 8) S8-12 oscillograph.

The average number of γ-quanta, k, emitted by the nucleus was determined from the average energy of the inelastically scattered neutrons from a comparison of the calculated and experimental data. When considering the cascade of the formation of elementary defects in Al_2O_3, irradiated with 14-MeV neutrons, the cascade multiplication factors were calculated by the modified model of Kinchin and Peas [5], converted for diatomic materials, and were averaged over the energy distributions of the initially knocked-out atoms. Using the data of [6-7], it was obtained that in the case of irradiation with a pulsed neutron flux of 10^{12} cm^{-2}, $1.73 \cdot 10^{14}$ defects per cm^3 are formed in the Al_2O_3.

An experimental investigation of the process of defect formation was carried out by measuring the radiation conductivity by means of an electron microscope and the method of positron annihilation. The generation of intense neutron fluxes was effected with the TONUS high-powered (high-accuracy) electron accelerator, with a lithium target for the collective acceleration of deuterium ions by an electron beam. The current of the beam of electrons with 900-keV energy amounted to 45 kA. The pulse duration at half-amplitude was equal to 60 nsec. The neutron yield per pulse attained $\sim 10^{10}$. Measurements of the neutron flux were made with an Ag-detector.

The conductivity of the ceramic during pulsed irradiation with neutrons was measured by the scheme shown in Fig. 1. Silver electrodes were deposited on corundum disks by brazing. For protection from bremsstrahlung, a lead wall with a thickness of 5 cm was located in front of the measurement cell with the sample. As a result of careful screening, the level of interference did not exceed 2 mV. The pulse of the potential drop, with an amplitude proportional to the radiation component of the conductivity of the sample being investigated, was photographed from the oscillograph screen. The measurement circuit allowed single pulses with a duration of $\sim 10^{-8}$ sec to be recorded and it had a sensitivity of $2 \cdot 10^{-9}$ ($\Omega \cdot$ cm)$^{-1}$. Pulsed irradiation with a stream of neutrons in the conditions of the experiment did not lead to the origination of radiation conductivity in MK, UF-46, GB-7, and MG-54 ceramics for a bias potential on the sample of 600 V.

Measurements before and after irradiation with a total neutron flux of $\sim 10^{12}$ cm^{-2} showed that changes of conductivity of the ceramics do not fall beyond the limits of experimental error ($\pm 10\%$). When the irradiated samples were investigated on the electron microscope, no irreversible structural changes were observed; however, with the aid of the more sensitive method of positron annihilation, some increase in the number of defects was established.

The calculations and experiments performed confirm the conclusion made earlier [3], according to which changes of conductivity of ceramics based on Al_2O_3, observed in the case of the combined action of γ radiation and neutrons, are caused by the action not of the neutrons but of the γ radiation. Calculations using the energy distributions of the initially knocked-out atoms, showed that the energy release causing breakdown of the corundum ceramic as a result of pulsed irradiation with a duration of 60 nsec by neutrons with 14-MeV energy, will be achieved with a neutron flux intensity of more than 10^{23} cm$^{-2} \cdot$ sec^{-1}.

LITERATURE CITED

1. U. G. Glyamov, N. S. Kostyukov, and A. P. Sokolov, "Electrical conductivity of mullite-corundum ceramic at elevated temperatures during reactor irradiation," At. Energ., 37, No. 1, 57 (1974).

2. N. P. Antonova, S. N. Makeev, N. I. Senina, and M. I. Manyasev, "Temperature dependence of the specific volume resistance of ceramic materials as a result of pulsed gamma-neutron irradiation," in: Effect of Radiation on Insulating Materials [in Russian], Filial Akad. Nauk, Tashkent (1977), pp. 34-37.
3. N. S. Kostyukov, V. V. Maslov, and M. I. Muminov, Radiation Stability of Dielectrics [in Russian], Filial Akad. Nauk, Tashkent (1981).
4. G. I. Kopylov, Principles of Resonance Kinematics [in Russian], Nauka, Moscow (1970).
5. G. Dell, H. Berry, A. Goland, and O. Lazareth, "Calculation of radiation damage in insulators for fusion reactors," J. Nucl. Mater., 85-86, 373-377 (1979).
6. C. Coulter and D. Parkin, "Damage energy function in polyatomic materials," J. Nucl. Mater., 88, 249-260 (1980).
7. D. Parkin and C. Coulter, "Displacement functions in polyatomic materials," J. Nucl. Mater., 85-86, 611-615 (1979).

DISCHARGE OF ^{14}C BY NUCLEAR POWER STATIONS
WITH RBMK-1000 REACTORS

V. B. Gaiko, N. A. Korablev,
E. N. Solov'ev, T. I. Trosheva, V. P. Shamov,
M. P. Umanets, and V. G. Shcherbina

UDC 621.039.524.2:539.172.8

According to the data of the report of the Scientific Committee of the United Nations Organization on the Effects of Nuclear Radiation (SCENR) in 1977, the normalized intensity of the discharge of ^{14}C amounts to 0.9 Ci [MW(el)·yr] (1 Ci = $3.7 \cdot 10^{10}$ Bq) for nuclear power stations with light-water−graphite reactors (LWGR) operating in the Soviet Union [1]. In [2] almost the same value was derived − 0.8 Ci [MW(el)·yr], based on which the forecast was made by certain foreign authors, that by 1990, 65% of the total amount of ^{14}C discharged by all the world's reactors will come from nuclear power stations in the Soviet Union with water−graphite reactors, whereas the fraction of such nuclear power stations in peaceful nuclear power generation amounts to 1.2% [3].

The value of the normalized intensity of the discharge of ^{14}C, equal to 0.8 Ci [MW(el)·yr], was obtained 10 years ago on the AMB reactor of the Beloyarsk nuclear power station [4]. At the present time, the basis of the power-generating water−graphite reactors operating and under construction in the Soviet Union, comprises the RBMK reactors which have structural and technological differences from the AMB reactor facility of the Beloyarsk nuclear power station. Therefore, the conversion of the data obtained from the facility to nuclear power stations with RBMK is unjustified. In the present paper, the results of a project are discussed, in the course of which the rate of formation and the intensity of the discharge of ^{14}C by nuclear power stations with RBMK-1000 reactors were determined by a computational and experimental route.

The formation of ^{14}C takes place in the following systems of a reactor (see Fig. 1):

1. Coolant. The ^{14}C formed in it, together with the radiolysis products, is exhausted by the ejector from the turbine condensers and is directed into the combustion plant with the detonating mixture. Later, in the form of carbon dioxide gas, it enters the atmosphere through the gas holder, filter, and ventilation stack.

2. Cooling System of the Control and Safety Rod Channels (not shown in the diagram). This is a closed autonomous circuit in which the control and safety rod channels are cooled with water. The ^{14}C formed enters the atmosphere directly through the filters and the ventilation stack.

3. Nitrogen−helium Purging Circuit of the Reactor Space. The nitrogen−helium mixture, circulating through the internal cavity of the reactor, provides the temperature conditions of the stack. From the reactor space, the nitrogen−helium mixture enters the helium scrubbing plant where ^{14}C formed is trapped by zeolite adsorbers. During the periodic regeneration of the adsorbers, the ^{14}C enters the atmosphere through the gas holder, filter, and ventilation stack.

TABLE 1. Calculated Values of the Normalized Rates of Formation and Discharge Intensity of ^{14}C in Nuclear Power Stations with RBMK-1000 Reactors

System	Nuclear reaction	Rate of formation, GBq/[MW(el) · yr]
Nitrogen—helium purging circuit of the reactor space (10 vol.% N_2 + 90 vol.% He)	^{14}N (n, p) ^{14}C	0,39
Nitrogen purging circuit of the metal structures of the circumreactor space	^{14}N (n, p) ^{14}C	0,54
Coolant	^{17}O (n, α) ^{14}C ^{14}N (n, p) ^{14}C	0,31
Cooling system of the control and safety rod channels	^{17}O (n, α) ^{14}C ^{14}N (n, p) ^{14}C	0,09
Fuel elements	^{17}O (n, α) ^{14}C	0,28
Graphite brickwork	^{13}C (n, γ) ^{14}C ^{14}N (n, p) ^{14}C	12,0
Total rate of formation		13,6
Intensity of discharge		1,33

TABLE 2. Experimental Values of the Normalized Rate of Formation of ^{14}C in Nuclear Power Stations with RBMK-1000 Reactors

System	Rate of formation, GBq/[MW(el) · yr]
Nitrogen—helium purging circuit of the reactor space (10 vol.% N_2 + 90 vol.% He)	0,3±0,1
Nitrogen purging circuit of the metal structures of the circumreactor space	0,6±0,2
Coolant (at the outlet from the detonating mixture combustion plant)	0,3±0,1
Cooling system of the control and safety rod channels	0,09±0,04
Total rate of formation	1,3±0,2
Discharge (ventilation stack, taking account of ventilation emerging at the roof)	1,0±0,3
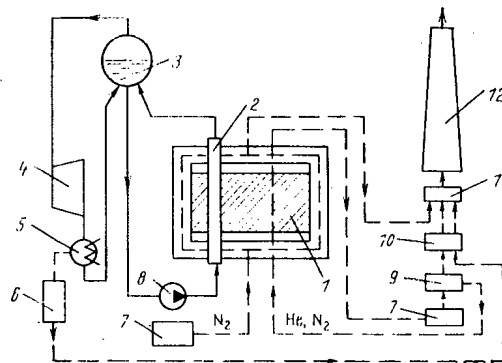
Fig. 1. Diagram of the discharge of ^{14}C by nuclear power stations with RBMK-1000 reactors: 1) graphite brickwork; 2) fuel channel; 3) drum separator; 4) turbogenerator; 5) condenser; 6) combustion plant for detonating gas; 7) compressor; 8) main circulatory pump; 9) helium scrubbing plant; 10) gas holder; 11) filter; 12) ventilation stack.

4. Nitrogen Purging Circuit of the Metal Structure of the Circumreactor Space. The ^{14}C formed enters the atmosphere directly through the filter and ventilation stack.

5. Fuel Elements. ^{14}C is formed in the fuel and cladding.

6. Graphite Brickwork. ^{14}C formed in the brickwork can enter the atmosphere only in the case of oxidation of the graphite.

The results of a numerical estimate of the normalized values of the rate of formation and intensity of the discharge of ^{14}C for the RBMK-1000 when operating at a nominal power [5] are shown in Table 1. The main contribution to the formation of ^{14}C is made by the graphite brickwork. However, its contribution to the discharge is insignificant as, at the existing rates of oxidation of the graphite of the brickwork, the discharge of ^{14}C from it at the end of 30 years of operation does not exceed $3.7 \cdot 10^7$ Bq [MW(el) · yr]. The ^{14}C formed in the fuel elements is localized under their cladding and therefore also makes no appreciable contribution to the discharge. The main quantity of the ^{14}C enters the atmosphere from four systems: the nitrogen—helium purging

704

circuit of the reactor space, the nitrogen purging circuit of the metal structures, the coolant, and the cooling system of the control and safety rod channels.

Work on the experimental determination of the discharge was conducted over 2 years on four power-generating units of the V. I. Lenin Nuclear Power Station, Leningrad. Sampling and the determination of the ^{14}C concentration was carried out in the nitrogen−helium mixture at the outlet from the reactor space, in the gas−air mixture at the exit from the detonation mixture combustion plant, on the purgings from the circulation tanks of the control and safety rods, and also in the ventilation stack. The investigations showed that the principal quantity (~70%) of the ^{14}C formed is found in the form of the dioxide. In view of this, sampling of ^{14}C is based on trapping the $^{14}CO_2$ with alkali. The absorbed carbon dioxide is precipitated in the form of $Ba^{14}CO_3$. Radiometric measurement of the purified $Ba^{14}CO_3$ deposit was carried out in a 4π−flow−counter in 2π−geometry by the "thick layer" method [6]. The sensitivity of the method is 10^2 Bq per gram of carbon. The experimental results obtained (Table 2) confirm that the total experimental and calculated discharge of ^{14}C into the atmosphere coincided well.

The experimentally obtained value of the ^{14}C discharge in nuclear power stations with RBMK−1000 reactors (1.0 ± 0.3) GBq/[MW(el)·yr] $\{(0.027 \pm 0.008)$ Ci/[MW(el)·yr]$\}$ is significantly less than that given in the SCENR report and is **comparable** with the discharges of ^{14}C in nuclear power stations with the principal types of reactors operating in the world − $(0.006$–$0.018)$Ci/[MW(el)·yr] [1].

LITERATURE CITED

1. Sources and Effect of Ionizing Radiation. Report of the Scientific Committee of the United Nations Organization on the Effect of Nuclear Radiation during 1977 [in Russian], New York (1978).
2. W. Davis, Carbon−14 Production in Nuclear Reactors, Oakridge National Laboratory Report ORNL/NUREG/TM12 (1977).
3. G. Killough and J. Till, "Scenarios of ^{14}C releases from the world nuclear power industry from 1975 to 2020, and estimated radiological impact," Nucl. Safety, 19, No. 5, 602–616 (1978).
4. V. Rublewsky, A. Zykova, and A. Turkin, "Atomic electric power stations as sources of ^{14}C discharge" in: Proceedings of the Third International Congress of the International Radiological Protection Association. Atomic Energy Agency Report CONF−730907, Washington, D. C., U.S.A. (1974).
5. N. A. Dollezhal' and I. Ya. Emel'yanov, Channel Nuclear Power Reactor [in Russian], Atomizdat, Moscow (1980).
6. V. P. Rublevskii, S. P. Golenetskii, and T. S. Kirdin, Radioactive Carbon in the Biosphere [in Russian], Atomizdat, Moscow (1979).

SPECIFIC RADIOACTIVITY OF POTASSIUM IN SEA WATER

Yu. A. Sapozhnikov and A. V. Merkushov

UDC 551.464.679

The natural radioactive potassium isotope ^{40}K provides the basic contribution to the intrinsic beta- and gamma-radioactivity of sea water [1]. It has been found that the concentration distribution of potassium K, which is among the basic sea water ions, is correlated with the salinity S, although considerable deviations of the K/S ratio from the mean values have been observed during various expeditions. The isotopic abundance of potassium in seawater is usually assumed to be constant, so that the specific activity of potassium A_K in sea water is considered to be equal to the value suggested for terrestrial rocks, $A_0 = 28.27 \pm 0.05$ Bq/g [2].

Our aim was to check the validity of the assumption concerning the constancy of A_K in sea water. Accurate methods have been developed for determining the radioactivity of ^{40}K [3] and the over-all potassium percentage in sea water samples, whereby the value of A_K can be estimated with an error of less than 1% with a 95% confidence coefficient.

In using either method, potassium is separated from sea water samples by precipitation by means of a selective reagent — sodium tetraphenyl borate (Na-TPB). For determining the radioactivity of ^{40}K, 500-ml samples were taken, and the deposit was separated and dissolved in a mixture of dimethyl formamide and dioxane with scintillation admixtures. We used Na-TPB, labeled with ^{14}C, for determining the overall potassium percentage; the sample volume was equal to 5 ml. Both methods involve radioactivity measurement by means of liquid-scintillator equipment.

Most of the ocean water samples for determining the A_K value were taken in the Pacific during the second stage of the first voyage of the Akademik Aleksandr Nesmeyanov scientific-research vessel in the autumn of 1982. Table 1 provides the results of A_K determination for these samples and also water samples from other parts of the world's oceans. The results of A_K determination in normal sea water and in extra spectroscopically pure solutions are given for comparison.

Altogether, 14 samples were taken in the Pacific Ocean. Within the limits of measurement error, the mean value of A_K in these samples coincided with that of A_0 [2]. However, there were also considerable deviations to either side of the mean value. Negative deviations were recorded in the equatorial region, while a band of positive deviations, reaching 5.9%, was observed to the north of the equatorial region (only two measurements were performed south of the equator, while a negative deviation was also found in the region near the equator); this is followed by a broad region of negative deviations, with the largest positive deviation (10.2%) observed in the subarctic front region.

The sampling of the A_K measurement results is, of course, too small for reaching unambiguous conclusions. It should be mentioned that the samples analyzed were taken at different depths (0, 100, 300, and 500 m), so that potassium behavior at different points may have reflected different trends. In spite of this, we note a certain dependence of A_K on the geographic latitude of the locations at which the samples were taken, which resembles the distribution of the atmospheric fallout of cosmic and artificial radionuclides that have reached the upper atmospheric layers as a result of nuclear tests.

Considerable negative deviations of A_K from the accepted values (up to -7.0%) were observed in water samples from thermal brine in deep-sea basins of the Red Sea. However, in the surface water layers of this sea, the A_K value corresponds to the mean value for terrestrial rocks. The positive deviations from the mean values are possibly connected with the incoming cosmic dust (minute particles of meteorite matter, formed during the ablation of meteorites in the atmosphere), whose isotropic potassium composition differs from the terrestrial one. Values of A_K in meteorites that exceeded those in terrestrial rocks by two to three orders of magnitude have been recorded [4, 5]. Values exceeding the A_K mean values by 40–70% have been observed in submillimeter-size magnetic spherules (probably of extraterrestrial origin), separated from deep-sea sediments in the Pacific Ocean [5]. For the oceans, which occupy $\sim 70\%$ of the earth's surface, the arrival rate of cosmic dust may reach $1.4 \cdot 10^9$ tons/yr [6]. The mean percentage of potassium in meteorite matter is equal to

TABLE 1. Specific Activity of Potassium in Sea Water Samples

Sample No.	Level, m	Latitude	E. long.	A_K, Bq/g	$\frac{A_K - A_0}{A_0} 100\%$
Pacific Ocean
1	300	42°30,0′ N. lat.	159°31,7′	31,15	+10,2
2	100	41°30,0′ N. lat.	159°31,0′	26,90	—4,8
3	0	40°33,3′ N. lat.	159°27,5′	28,15	—0,4
4	500	40°03,1′ N. lat.	159°20,0′	27,88	—1,4
5	0	24°41,5′ N. lat.	150°01,4′	27,67	—2,1
6	500	21°04,5′ N. lat.	150°08,8′	27,50	—2,7
7	0	18°00,2′ N. lat.	152°16,4′	27,63	—2,3
8	500	12°55,6′ N. lat.	155°32,1′	28,88	+2,2
9	0	10°51,4′ N. lat.	157°16,4′	29,93	+5,9
10	0	04°33,8′ N. lat.	159°36,0′	28,47	+0,7
11	0	01°14,4′ N. Lat.	160°17,3′	27,65	—2,2
12	0	01°53,1′ S. lat.	162°26,0′	27,83	—1,6
13	300	13°58,3′ S. lat.	157°14,6′	28,43	+0,6
14	0	02°51,3′ N. lat.	146°59,0′	28,33	+0,2
Sea of Japan
15	0	40°08,3′ N. lat.	131°50,5′	28,03	—0,8
Red Sea
16	0			28,22	—0,2
17	1460 (3 m from bottom)			27,40	—3,1
18	Atlantis Basin (5 m from bottom)			26,28	—7,0
19	Valdivia Basin (depth, 1660 m; 3 m from bottom)			26,77	—5,3
20	Normal sea water (19.374% Cl)			28,03	—0,8
21	KCl, extra spectroscopically pure			28,37	+0,4

0.15% [7], while, according to estimates for the terrigenous suspension, 1–10% of matter available in the form of a suspension is dissolved in sea water [8], i.e., together with extraterrestrial matter, $2.2 \cdot 10^4$ to $2.2 \cdot 10^5$ tons of dissolved potassium enters the ocean water annually, while the quantity entering sea water with river effluence amounts to $5.25 \cdot 10^7$ tons [9].

An important conclusion has been reached in [6] on the basis of a generalization of the data provided by many researchers: The size distribution of cosmic dust particles is such that the mean rate of arrival of particles on earth increases rapidly as their mass decreases, up to the limiting value of $\sim 10^{-12}$g (particles with a mass of $\sim 10^{-14}$ g are carried away by solar light pressure beyond the confines of the solar system). As they fall into the ocean, these fine particles dissolve readily in sea water. It is difficult to determine the dispersion composition of the undissolved part of extraterrestrial matter entering the ocean. This was probably the reason why data on the size distribution of spherical particles in the peat at the location of impact of the Tunguska meteorite were used in [10] for estimating the contribution of extraterrestrial matter in the dispersion composition of oceanic sediments.

It is known that meteorites are linked with the concept of cosmic or radiation age, i.e., the time elapsed from the disintegration of the parent body and irradiation of a certain fragment by cosmic radiation [11]. In contrast to small particles, large meteorites have a lower mean specific activity (because the radiation is attenuated by the meteorite mass). Moreover, it is precisely the surface layers of meteorites, which are highly exposed to the action of cosmic radiation, that are atomized as they enter the atmosphere during the ablation process. As they pass through the atmosphere, meteorites lose about one–half to two-thirds of their mass [12]. Consequently, it is possible that even larger A_K values may be in the fine–dispersion suspension of cosmic origin, which is the main source of dissolved forms of extraterrestrial matter in sea water, than in relatively large meteorites.

The nonuniformity of the A_K distribution in sea water may be connected with the temporal and spatial nonuniformity of arrival of extraterrestrial matter. Actually, an increase in the arrival rate of cosmic dust by two to three orders of magnitude in comparison with the mean rate is observed at the time of occurrence of the known intensive meteorite showers reaching the earth's surface [13]. The spatial nonuniformity of arrival of extraterrestrial matter on the earth's surface from the upper atmospheric layers resembles in many ways the character of the fallout of radionuclides of cosmic origin [12] and of artificial radionuclides that have entered the stratosphere as a result of nuclear tests [14].

The role of extraterrestrial matter in oceanic sediment formation is sometimes considered to be insignificant [10]. However, it is difficult to explain the considerable increase in A_K in ocean waters by other causes. Analysis of other processes possibly influencing A_K in sea water (sorption on argillaceous suspensions, biological activity, formation and melting of ice, processes in the surface microlayer, etc.) indicates that their

707

total contribution can alter the value of A_K by not more than 1-2%. At the same time, it has been found that the isotopic lead abundance in deep-sea sediments is close to the percentage of isotropic lead in meteorites [15], while siderophile elements, such as nickel and cobalt, of which there is a much higher percentage in meteorites than in the earth's crust, enter the ocean also from the atmosphere and not only with the river effluence. Their entry into the atmosphere is probably connected to a considerable extent with extraterrestrial matter. The specificities of the state of iron in deep-sea sediments are possibly also connected with the effect of both extraterrestrial and volcanic matter [16].

Irregularities in A_K values could probably also occur as a result of volcanic activity, the contribution of which to sediment formations in oceans reaches 2-3 billion tons annually [9]. Volcanic matter can also be enriched by siderophile elements [17, 18]; however, it is not subject to the effect of cosmic radiation below the surface of the earth.

Volcanic matter enters sea water as a result of the activity of land volcanoes and, to a greater extent, due to undersea eruptions [18]. The water from thermal brines in the Red Sea, which is characterized by low A_K values, probably arrives from a fairly great depth in the earth, where the potassium lodged there since the times of layer differentiation within the earth's crust was not subject to the action of cosmic radiation or exchange with the potassium arriving with ground water from the surface layers of the earth's crust.

Dust of cosmic or volcanic origin can be retained over a long period of time by the surface microlayer of sea water [19], where its composition can undergo considerable changes due to the action of surface-active matter and biological activity. With the subsequent slow submergence of microscopic particles, which may remain in the water over periods of hundreds or thousands of years [20], further leaching of compounds with an anomalous isotopic potassium composition takes place, which leads to changes in the A_K value in water. As a result of similar processes, the number of particles of cosmic origin (including magnetic spherules) in oceanic sediments is much smaller than in the ice of Antarctica [21].

Thus, A_K can be used as an indicator of elevated concentrations in large bodies of water of both extraterrestrial (positive deviation of A_K from the mean value) and volcanic matter (negative deviation).

LITERATURE CITED

1. N. I. Popov, K. N. Fedorov, and V. M. Orlov, Sea Water (Reference Manual) [in Russian], Nauka, Moscow (1979).
2. R. Beckinsale and N. Gale, "A reappraisal of the decay constants and branching ratio of ^{40}K," Earth Planet. Sci. Lett., $\underline{6}$, 289-294 (1969).
3. A. V. Merkushov and Yu. A. Sapozhnikov, "Scintillation-liquid determination of potassium in sea water," Vestn. Mosk. Gos. Univ., Ser. Khim., 5 (1983); deposited at the All-Union Institute of Scientific and Technical Information (VINITI) on April 7, 1983, No. 1868-83.
4. H. Voshage and H. Hinterberger, "Massenspektrometrische Isotropenhäufigkeitsmessungen an Kalium aus Eisenmeteoriten und das Problem der Bestimmung der ^{41}K-Strahlungsalter," Z. Naturforsch., $\underline{16a}$, 1042-1053 (1961).
5. T. Shimamura, O. Arai, and K. Kobayashi, "Isotopic ratios of potassium in magnetic spherules from deep-sea sediments," Earth Planet. Sci. Lett., $\underline{36}$, 317-321 (1977).
6. É. V. Sobotovich, Isotopic Space Chemistry [in Russian], Atomizdat, Moscow (1979).
7. G. V. Voitkevich, A. E. Miroshnikov, A. S. Povarennikh, and V. G. Prokhorov, Brief Manual of Geochemistry [in Russian], Nedra, Moscow (1977).
8. Oceanography, Marine Chemistry, Chemistry of Ocean Water [in Russian], Vol. 1, Nauka, Moscow (1979).
9. A. P. Vinogradov, Introduction to Marine Geochemistry [in Russian], Nauka, Moscow (1967).
10. A. P. Lisitsyn and Yu. A. Bogdanov, "Granulometric composition of suspensions from the Pacific Ocean," Oceanographic Research [in Russian], Vol. 18, Nauka, Moscow (1968), pp. 53-74.
11. J. Wood, Meteorites and the Origin of the Solar System [Russian translation], Mir, Moscow (1971).
12. V. Yu. Luyanas, Atmospheric Radionuclides of Cosmic Origin [in Russian], Mosklas, Vilnius (1979).
13. G. M. Ivanova, Yu. A. L'vov, N. V. Vasil'ev, and I. V. Antonov, Fallout of Cosmic Matter on the Earth's Surface [in Russian], Izd. Tomsk. Univ. (1975).
14. I. L. Karol', Radioactive Isotopes and Global Transport in the Atmosphere [in Russian], Gidrometeoizdat, Leningrad (1972).
15. S. P. Golenetskii, "The nature of global atmospheric aerosols," Astron. Vestn., $\underline{15}$, No. 4, 226-233 (1981).

16. Y. Minai, T. Tominaga, T. Furuta and K. Kobayashi, "A Mössbauer study of deep sea sediments," Radiochem. Radioanal. Lett., 48, Nos. 3-4, 165-173 (1981).
17. W. Zoller, "Iridium enrichment in airborne particles from Kilauea volcano, January, 1983," Science, 222, No. 4628, 1118-1121 (1983).
18. K. K. Zelenov and V. I. Ivanenkov, "Effect of contemproary undersea volcanism on the chemistry of ocean water," Izv. Vyssh. Uchebn. Zaved., Ser. Geolrazvedka, 25, No. 11, 3-26 (1982).
19. K. Hunter, "Processes affecting particulate trace metals in the sea surface microlayer," Marine Chem., 9, 49-70 (1980).
20. A. S. Monin, History of the Earth [in Russian], Nauka, Leningrad (1977).
21. É. V. Sobotovich, G. N. Bondarenko, and T. I. Koromyslichenko, Cosmic Matter in Ocean Sediments and Glacier Covers [in Russian], Naukova Dumka, Kiev (1978).

COMPARISON OF DETECTORS WITH RESPECT TO THE LOWER LIMIT OF DETERMINING THE ACTIVITY OF GAMMA-EMITTING NUCLIDES

B. Ya. Shcherbakov and V. I. Myshlyavkin

UDC 628.3:539.166:543.52

Since the number of tasks in environmental monitoring is increasing, an experimental comparison of the capabilities of various detectors with respect to the lower limit of activity determinations on gamma-emitting nuclides is of interest.

Measurements were made with a gamma spectrometer provided with an 800-channel analyzer and detectors of various types and dimensions: a DGDK-32A germanium detector and NaI (Tl) scintillation detectors with the dimensions 63×63, 150×100, and 150×140 mm with a well. A 10-cm-thick passive lead shield of detectors was employed. The comparison was based on ^{137}Cs (energy of the gamma radiation 661.7 keV) in liquid 25-, 50-, 75-, and 100-ml samples filled into 100-ml polyethylene bottles (see Fig. 1). The liquid samples were prepared from a radioactive ^{137}Cs standard solution of class 1 with a specific mass activity q (Bq/g) indicated in the specification data with an error of 3% on the 0.95 confidence level. A certain amount of the radioactive standard solution was filled into the polyethylene bottle which had been previously weighed on an analytic balance with a precision of 0.0001 g; thereafter the bottle was weighed again and the mass m (g) of the sample taken was determined. The activity Q (Bq) of the quantity of the radioactive standard solution filled into the bottle was determined with the equation

$$Q = qm. \tag{1}$$

The error of Q did not exceed 4%. After that, a diluting agent recommended in the specification data was poured into the bottle to obtain a volume V = 25 ml, the solution was mixed, the bottle was hermetically sealed with a lid, and then the bottle was placed on the detector as indicated in Fig. 1a. After that, the average pulse frequency $\bar{n}$ (sec^{-1}) in the peak of total absorption of the 661.7-keV gamma quanta was determined (with the background subtracted) and the detector efficiency was calculated with the formula

$$\varepsilon = \bar{n}/Qp, \tag{2}$$

where the gamma quanta yield p = 0.853 was assumed [1]. Then the volume of the solution in the bottle was successively increased to 50, 75, and 100 ml, the measurements were repeated, and the detector efficiency was determined in each case. The results obtained are compiled in Fig. 2.

The lower limit of the determination of the ^{137}Cs bulk activity was estimated under the assumption that no errors were introduced from the "harder" radiation of other nuclides because in the case of a complicated composition of the initial sample, the nuclide of interest can be isolated in pure form by chemical methods. Thus, only the natural background generated by the cosmic radiation, the building materials, and the surrounding objects was taken into account. The average pulse frequency of the background pulses and the mean-square errors obtained with passive lead shields of various thicknesses on the detectors are listed in Table 1.
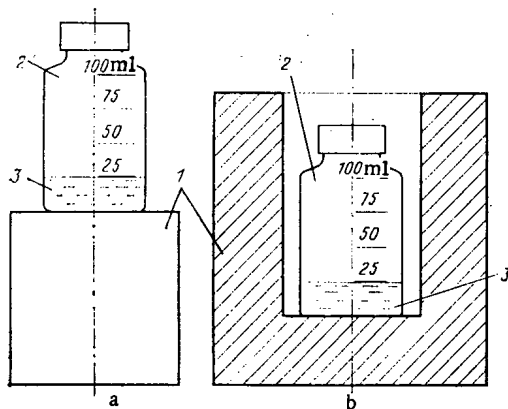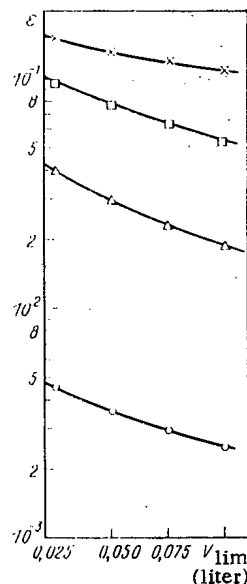
709

Fig. 1

Fig. 2

Fig. 1. Geometrical conditions in the measurements in the case of a) detectors without well and b) detectors with well: 1) detector; 2) polyethylene bottle; 3) radioactive standard solution.

Fig. 2. Dependence of ε upon the sample volume with various detectors: O) DGDK–32A detector; $\triangle$) NaI(Tl) detector with a size of 63×63 mm; $\square$) NaI(Tl) detector, size 150×100 mm; ×) NaI(Tl) detector, size 150×140 mm, with well.

TABLE 1. Average Background Pulse Frequency (sec^{-1}) in the Region of the Peak of Total Absorption of 661.7–keV Gamma Quanta; Various Detectors

Shield thickness (cm)	DGDK-32A	NaI (Tl), $\varnothing\, 63\times 63$ mm	NaI (Tl), $\varnothing\, 150\times 100$ mm	NaI (Tl), $\varnothing\,150\times140$ mm with well $\varnothing\,70\times100$ mm
5	$0,021\pm0,001$	$1,98\pm0,03$	$9,55\pm0,11$	$20,5\pm0,3$
10	$0,016\pm0,001$	$1,08\pm0,03$	$6,46\pm0,07$	$16,7\pm0,3$
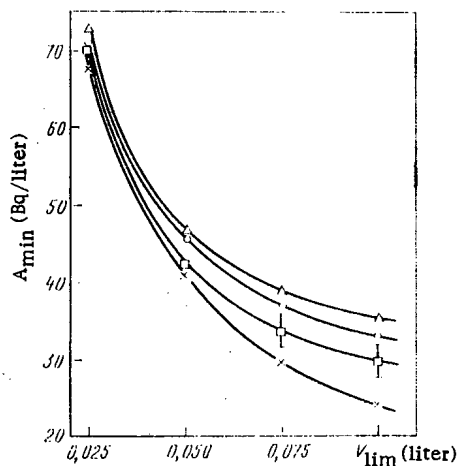
Fig. 3. Dependence of the lower limit of determining the bulk activity of ^{137}Cs upon the volume of the liquid sample; various detectors (the notation of the curves is the same as in Fig. 2).

710

TABLE 2. Lower Limit of Determining the Bulk Activity of Nuclides in Liquid Samples with a DGDK-32A Germanium Detector

Nuclide	Energy (keV) in the maximum of the peak of total absorption [1]	Results of our work		AC (Bq/m³)
		frequency (sec⁻¹) of the background pulses	A_{min} (Bq/m³)	
^{24}Na	1368,6	0,010±0,001	8,5·10⁴	1,0·10⁶
^{54}Mn	834,9	0,016±0,001	5,3·10⁴	4,4·10⁵
^{60}Co	1332,5	0,011±0,001	8,3·10⁴	1,3·10⁶
^{65}Zn	1115,6	0,016±0,002	1,6·10⁵	3,7·10⁶
^{95}Zr	756,7	0,015±0,002	8,3·10⁴	2,3·10⁶
^{95}Nb	765,8	0,014±0,002	4,5·10⁴	3,6·10⁶
^{103}Ru	497,1	0,043±0,004	4,5·10⁴	3,0·10⁶
^{106}Ru + ^{106}Rh	511,9	0,042±0,003	2,0·10⁵	4,4·10⁵
	621,9	0,023±0,002	4,2·10⁵	
^{131}I	364,5	0,068±0,002	4,0·10⁴	3,7·10⁴
^{137}Cs	661,7	0,016±0,001	4,6·10⁴	5,6·10⁵
^{144}Ce	133,5	0,160±0,004	2,4·10⁵	4,4·10⁵

The lower limit A_{min} (Bq/liter) of determining the bulk activity of ^{137}Cs was calculated with an equation of [2]:

$$A_{min} = \frac{\sqrt{2n_b}}{\delta\sqrt{t\varepsilon pV}}, \tag{3}$$

where n_b denotes the frequency of pulses generated by the natural background under the peak of total absorption of gamma quanta; δ, maximum admissible relative error in the determination of the area of the peak of total absorption of gamma quanta; t, time (sec) of the measurements; ε, efficiency of the detector under the particular conditions of the measurement; p, gamma quantum yield; and V, volume (liter) of the sample.

The results in the calculation of A_{min} obtained with a 10-cm-thick lead shield, $t = 2$ h, and $\delta = 0.3$ (since $\delta > 0.3$, the normal distribution of the number of pulses and the validity of Eq. (3) are affected) are shown in Fig. 3. The vertical lines denote the mean-square errors resulting only from the errors of the experimental ε and n_b values.

A comparison of the curves of Fig. 3 reveals that despite the significantly higher efficiency, scintillation detectors even of a large volume do not provide advantages with respect to the lower limit of determining the activity in comparison with a smaller germanium detector with a passive shield, because the background under the peak of total absorption of gamma quanta is high. The poor resolution of the scintillation detectors is the main reason (in the case under consideration, the resolution is between 10 and 16% in the 661.7-keV line). Therefore, in determinations of a low activity of gamma-emitting nuclides in liquid waste, emissions into the atmosphere, and objects in the environment, germanium semiconductor detectors, which provide more information, should be preferably used.

The DGDK-32A germanium detector with a passive 10-cm-thick lead shield was used to establish experimentally the lower limit of determining the bulk activity of nuclides in a liquid 50-ml sample which was placed directly on the upper lid of the detector as shown in Fig. 1a; the nuclides ^{24}Na, ^{54}Mn, ^{60}Co, ^{65}Zn, ^{95}Zr, ^{95}Nb, ^{103}Ru, ^{106}Rh, ^{131}I, ^{137}Cs, and ^{144}Ce, which are very important with respect to environmental protection, were considered. The dependence of the absolute detector efficiency upon the energy of the gamma quanta was determined from radioactive standard solutions of class 1 with the nuclides ^{57}Co (E = 122.1 and 136.5 keV), ^{137}Cs (E = 661.7 keV), and ^{60}Co (E = 1173.2 and 1332.5 keV); the solutions had been diluted to a volume of 50 ml. The activity of the solutions amounted to about $5 \cdot 10^4$ Bq and was in each case determined with an error of less than 4%. The error made in the determination of the efficiency with the aid of Eq. (2) amounted to at most 7%. The position of the peak of total absorption of gamma quanta for each nuclide was found in the analyzer channels and with the aid of an energy calibration and the resolution of the spectrometer. The average values of the pulse frequency of the background under the peaks of total absorption of gamma quanta and the mean-square errors of the average values were determined in multiple measurements of the natural background. The results are listed in column 3 of Table 2. The lower limit A_{min} (Bq/m³) of determining the bulk activity of each of the nuclides was calculated with Eq. (3), assuming $\delta = 0.3$, $t = 2$ h, and V = 50 ml ($5 \cdot 10^{-5}$ m³). The gamma-quantum yield figures were taken from the handbook [1]. The results are listed in column 4 of Table 2. For comparison, the admissible concentrations AC of the nuclides in water are listed in column 5 [3].

It follows from a comparison that the lower limit of determining the bulk activity of gamma-emitting nuclides in liquid samples with the aid of gamma spectrometers equipped with a small germanium detector and

a passive 10-cm-thick lead shield in a laboratory on the ground during a medium measurement time (2 h) and in the case of a small sample volume (50 ml) is not above the admissible concentration of the nuclides in water and is for some of the nuclides even much lower to a degree which suffices for many tasks of environmental protection. If it is necessary to determine a much lower activity, the background of the cosmic radiation can be reduced by transferring the spectrometer into an underground laboratory, as indicated in [4–6], or by employing an active detector shield.

LITERATURE CITED

1. Yu. V. Khol'nov, V. P. Chechev, V. G. Nedovesov, et al., Characteristics of the Radiations of Radioactive Nuclides Employed in the National Economy [in Russian], Atomizdat, Moscow (1980).
2. V. A. Dement'ev, The Measurement of Low Activities of Radioactive Samples [in Russian], Atomizdat, Moscow (1967).
3. Radiation Safety Standards NRB–76 and Basic Health Regulations OSP–72/80 [in Russian], Énergoizdat, Moscow (1981).
4. L. I. Shekherov, Ya. D. Prodanov, G. V. Stefanov, et al., "Comparative measurements of the radioactive background of gamma radiation in various shielding chambers with the aid of a germanium–lithium detector," in: Radiation Safety in the Operation of Atomic Power Stations [in Russian], Book 4, Énergoatomizdat, Moscow (1984), pp. 3–10.
5. L. I. Shekherov, Ya. D. Prodanov, G. I. Stefanov, et al., "A low-background Ge(Li) spectrometer under various conditions of shielding," in: Radiation Safety in the Operation of Atomic Power Stations [in Russian], Book 5, Énergoatomizdat, Moscow (1984), pp. 160–176.
6. O. S. Tsvetkov and N. G. Triumfov, "The measurement of low concentrations of radionuclides under the conditions of an underground laboratory shielded from cosmic radiation," in: Radiation Safety in the Operation of Atomic Power Stations [in Russian], Book 5, Énergoatomizdat, Moscow (1984), pp. 177–185.

THE KINETICS OF LIBERATING IMPLANTED HELIUM
FROM A 20-45 NICKEL ALLOY IN HIGH-TEMPERATURE
DEFORMATIONS

B. A. Kalin, A. V. Markin,
A. A. Volkov, S. N. Korshunov, D. M. Skorov,
V. T. Fedotov, I. I. Chernov, and A. N. Mansurova

Cold helium, desorbed from the first wall by heating and radiation-induced erosion will significantly contribute to the energy balance of the plasma in a thermonuclear reactor. Mechanical stress and deformations arise in the first wall during the operation of the reactor and substantially affect the surface destruction by erosion. The goal of the present work is to develop a method of recording the desorption of helium during a high-temperature deformation.

The experiment setup comprised a unit for mechanical testing in vacuum and a PTI–10 mass spectrometer. The sample was heated by passing through it an electric current so that good vacuum and low thermal inertia were guaranteed. In order to obtain temperature levelling over the useful length, a sample of special construction [1] was used. The method was tested with Kh20N45 alloy samples which had been previously irradiated with 40-keV helium ions at 370°K and up to a flux of $3 \cdot 10^{21}$ m^{-2} (Fig. 1). The desorption rate decreased uniformly during a 2-h exposure at 1000°K (see Fig. 2). After applying a load, an incubation period of 100 sec was observed within which the desorption rate was constant. Then the desorption rate increased sharply. A stress reduction reduced the desorption rate. When the stress was increased again, the incubation period did not show up.

The activation energy H of processes accounting for the creep and the helium desorption was determined with the technique of small temperature jumps based on a formula of [2]

Fig. 1

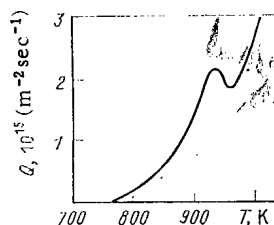Fig. 2

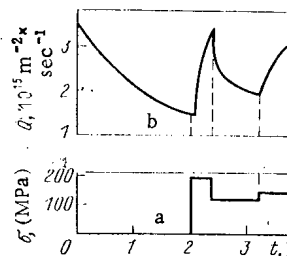Fig. 1. Helium liberation Q from the Kh20N45 alloy in the case of 1000°K heating at a rate of 0.5 K/sec.

Fig. 2. Dependence of the rate of helium liberation upon the mechanical stress σ.

$$H = kT \frac{T}{\Delta T} \ln \frac{q\,(T + \Delta T)}{q\,(T)} \, ,$$

where k denotes the Boltzmann constant; T, absolute temperature; and q, rate of creep or desorption.

The calculated activation energies coincided within the error limits and amounted to 3 eV. This means that there exists a vacancy mechanism of helium migration in the particular alloy at 1000°K.

The dependence which we obtained for the rate of helium liberation upon the mechanical stress seems to be associated with an increase in the mobility of the helium atoms by diffusion because the vacancy concentration rises in deformations. Besides that, structure studies of the alloy, which were made with an electron microscope, have shown that slip along boundaries and sliding inside grains occur after a deformation. This leads to the development of 10–100-nm-high steps on the sample surface and implies the breakup of the implanted layer (the assumed range of the 40-keV helium ions in the alloy is 200 nm). Accordingly, the desorption rate must depend upon the deformation rate, and the incubation period must obviously be associated with a delayed deformation of the surface layer of the sample.

Thus, our results indicated that deformations substantially affect the liberation of helium. This must be taken into account in the energy balance of the plasma.

LITERATURE CITED

1. "A sample for studying the strength of materials under high temperatures," Inventor's Certificate No. 974,208, Byull. Izobret., No. 42, 196 (1982).
2. F. Garofalo, The Laws of Creep and of Long-Term Strength of Metals [in Russian], Metallurgiya, Moscow (1978).

ERRATUM

The article by E. P. Veretenkin et al. "Use of metallic lithium for detecting solar neutrinos" (Vol. 58, No. 1, pp. 82-83 (1985)) contains a misprint. Line 13 of the first paragraph should read: "and this is 1000 times lower than the usual contamination of the surrounding materials."

How To Comply With The New Copyright Law

Participation in the Copyright Clearance Center (CCC) assures you of legal photocopying at the moment of need.

Libraries everywhere have found the easy way to fill photocopy requests legally and instantly, without the need to seek permissions, from more than 3000 key publications in business, science, humanities, and social science. You can:

Fill requests for multiple copies, interlibrary loan (beyond the CONTU guidelines), and reserve desk without fear of copyright infringement.

Supply copies from CCC-registered publications simply and easily.

The Copyright Clearance Center is your one-stop place for on-the-spot clearance to photocopy for internal use.

Its flexible reporting system accepts photocopying reports and returns an itemized invoice. You send only one convenient payment. CCC distributes it to the many publishers whose works you need.

And, you need not keep any records, the CCC computer will do it for you. Register now with the CCC and you will never again have to decline a photocopy request or wonder about compliance with the law for any publication participating in the CCC.

To register or for more information, just contact:
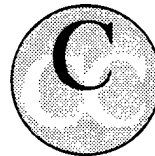
Copyright Clearance Center
21 Congress Street
Salem, Massachusetts 01970
(617) 744-3350

a not-for-profit corporation

NAME	TITLE
ORGANIZATION	
ADDRESS	
CITY	STATE ZIP
COUNTRY	TELEPHONE

CHANGING YOUR ADDRESS?

In order to receive your journal without interruption, please complete this change of address notice and forward to the Publisher, 60 days in advance, if possible.

(Please Print)

Old Address:

_____
name

_____

_____
address

_____
city

_____
state (or country)   zip code

New Address

_____
name

_____

_____
address

_____
city

_____
state (or country)   zip code

_____
date new address effective

_____
name of journal

THE LANGUAGE OF SCIENCE

Plenum
PUBLISHING CORPORATION | **233 Spring Street, New York, New York 10013**

MEASUREMENT TECHNIQUES
Izmeritel'naya Tekhnika
Vol. 27, 1984 (12 issues) $520

MECHANICS OF COMPOSITE MATERIALS
Mekhanika Kompozitnykh Materialov
Vol. 20, 1984 (6 issues) $430

METAL SCIENCE AND HEAT TREATMENT
Metallovedenie i Termicheskaya Obrabotka Metallov
Vol. 26, 1984 (12 issues) $540

METALLURGIST
Metallurg
Vol. 28, 1984 (12 issues) $555

PROBLEMS OF INFORMATION TRANSMISSION
Problemy Peredachi Informatsii
Vol. 20, 1984 (4 issues) $420

PROGRAMMING AND COMPUTER SOFTWARE
Programmirovanie
Vol. 10, 1984 (6 issues) $175

PROTECTION OF METALS
Zashchita Metallov
Vol. 20, 1984 (6 issues) $480

RADIOPHYSICS AND QUANTUM ELECTRONICS
Izvestiya Vysshikh Uchebnykh Zavedenii, Radiofizika
Vol. 27, 1984 (12 issues) $520

REFRACTORIES
Ogneupory
Vol. 25, 1984 (12 issues) $480

SIBERIAN MATHEMATICAL JOURNAL
Sibirskii Matematicheskii Zhurnal
Vol. 25, 1984 (6 issues) $625

SOIL MECHANICS AND FOUNDATION ENGINEERING
Osnovaniya, Fundamenty i Mekhanika Gruntov
Vol. 21, 1984 (6 issues) $500

SOLAR SYSTEM RESEARCH
Astronomicheskii Vestnik
Vol. 18, 1984 (6 issues) $365

SOVIET APPLIED MECHANICS
Prikladnaya Mekhanika
Vol. 20, 1984 (12 issues) $520

SOVIET ATOMIC ENERGY
Atomnaya Énergiya
Vols. 56-57, 1984 (12 issues) $560

SOVIET JOURNAL OF GLASS PHYSICS AND CHEMISTRY
Fizika i Khimiya Stekla
Vol. 10, 1984 (6 issues) $235

SOVIET JOURNAL OF NONDESTRUCTIVE TESTING
Defektoskopiya
Vol. 20, 1984 (12 issues) $615

SOVIET MATERIALS SCIENCE
Fiziko-khimicheskaya Mekhanika Materialov
Vol. 20, 1984 (6 issues) $445

SOVIET MICROELECTRONICS
Mikroélektronika
Vol. 13, 1984 (6 issues) $255

SOVIET MINING SCIENCE
Fiziko-tekhnicheskie Problemy Razrabotki Poleznykh Iskopaemykh
Vol. 20, 1984 (6 issues) $540

SOVIET PHYSICS JOURNAL
Izvestiya Vysshikh Uchebnykh Zavedenii, Fizika
Vol. 27, 1984 (12 issues) $520

SOVIET POWDER METALLURGY AND METAL CERAMICS
Poroshkovaya Metallurgiya
Vol. 23, 1984 (12 issues) $555

STRENGTH OF MATERIALS
Problemy Prochnosti
Vol. 16, 1984 (12 issues) $625

THEORETICAL AND MATHEMATICAL PHYSICS
Teoreticheskaya i Matematicheskaya Fizika
Vol. 58-61, 1984 (12 issues) $500

UKRAINIAN MATHEMATICAL JOURNAL
Ukrainskii Matematicheskii Zhurnal
Vol. 36, 1984 (6 issues) $500

Send for Your Free Examination Copy

ALS IN THE PHYSICAL
IATICAL SCIENCES

AVAILABLE IN ENGLISH TRANSLATION